Spatial Aggregation of Land Surface Characteristics:

Impact of resolution of remote sensing data on land surface modelling

Promotor:	dr. ir. R.A. Feddes Hoogleraar in de bodemnatuurkunde, agrohydrologie en grondwaterbeheer
Co-promotor:	dr. M. Menenti Visiting professor, Université Louis Pasteur, Strassbourg, Frankrijk

H. Pelgrum

NN08201, 2812

Spatial Aggregation of Land Surface Characteristics:

Impact of resolution of remote sensing data on land surface modelling

Proefschrift
ter verkrijging van de graad van doctor
op gezag van de rector magnificus
van Wageningen Universiteit,
dr C. M. Karssen,
in het openbaar te verdedigen
op woensdag 14 juni 2000
des namiddags te vier uur in de Aula.

im 979213

CIP-DATA KONINKLIJKE BIBLIOTHEEK, DEN HAAG

Pelgrum, H.

Spatial aggregation of land surface characteristics: impact of resolution of remote sensing data on land surface modelling / H. Pelgrum. - [S.1. : s.n.]
Thesis Wageningen Universiteit. - With ref. - With summary in Dutch.
ISBN 90-5808-243-I
Subject headings: hydrology / remote sensing.

NN08201, 2812

1. De wavelet variantie bepaald met de Haar wavelet is een goede maat voor de lengte schaal van landoppervlakte eigenschappen die zijn afgeleid van remote sensing gegevens.

   Dit proefschrift

2. De grootte van de aggregatie fout van een landoppervlak model gebruikmakend van remote sensing gegevens als invoer hangt af van de mate van niet-lineariteit van het landoppervlak model en de mate van heterogeniteit van de remote sensing gegevens.

   Dit proefschrift

3. De maximale aggregatie fout voor individuele pixels neemt af bij toenemende resolutie.

   Dit proefschrift

4. De dominante lengte schaal voor een landoppervlakte eigenschap is niet per definitie gelijk aan de optimale geometrische resolutie voor remote sensing gegevens om die bepaalde eigenschap mee te bepalen.

   Dit proefschrift

5. De grootste onzekerheid in het karteren van de landoppervlak energie balans met behulp van remote sensing gegevens wordt bepaald door de karakterisering van de ruwheid voor momentum en warmte.

   Dit proefschrift

6. Het waarnemend vermogen van een remote sensing satelliet wordt niet alleen door de geometrische en spectrale resolutie bepaald maar ook voor een deel door de gebruiker van de gegevens.

7. De atmosferische grenslaag scheidt niet alleen het aardoppervlak van de vrije troposfeer maar ook de hydrologen van de meteorologen.

8. Elke vergelijking waarbij de NDVI of een andere gewasindex wordt gebruikt om een fysische variable af te leiden moet worden bekeken met de nodige skepsis.

9. Land met een duidelijk agrarische bestemming is een onmisbaar onderdeel in het Nederlandse landschap.

10. Een instituut voor wetenschappelijk onderzoek behoort een naam te hebben die duidelijk aangeeft wat het onderzoeksveld van het instituut is.

11. Het stoppen als fietser of voetganger voor rood licht vereist tegenwoordig meer moed dan het negeren ervan.

12. Niets smaakt zo goed als het zoet van een onverdiende overwinning.

13. Het Nederlands elftal wordt nooit wereldkampioen voetbal.

Stellingen behorend bij het proefschrift *Aggregation of land surface characteristics: impact of resolution of remote sensing data on land surface modelling.* Henk Pelgrum, Wageningen, 14 juni 2000.

Abstract

Pelgrum, H., 2000, *Spatial aggregation of land surface characteristics: Impact of resolution of remote sensing data on land surface modelling.* Doctoral Thesis, Wageningen University, The Netherlands.

Land surface models describe the exchange of heat, moisture and momentum between the land surface and the atmosphere. These models can be solved regionally using remote sensing measurements as input. Input variables which can be derived from remote sensing measurements are surface albedo, surface temperature and vegetation cover. A land surface model using those land surface characteristics is presented i.e. the Surface Energy Balance Index (SEBI) model. This model uses the observed temperature difference between the land surface and atmosphere as an indicator for evapotranspiration.

Spatially distributed land surface model results can be used as a boundary condition for numerical weather predicton models. The results should therefore be aggregated from the remote sensing pixel scale to the atmospheric model scale. However aggregated values will differ when derived from remote sensing data with different resolutions. This difference, the error due to aggregation is caused by two different aspects: land surface heterogeneity and non-linearity of the land surface model. Two approaches are presented to quantify the error due to aggregation: the *linearization* approach, where the land surface model is approximated by a Taylor expansion and a *geometrical* approach where the range of valid results for the land surface model is derived using a convex hull.

To measure the heterogeneity of land surfaces, the concept of length scale is introduced. The wavelet transform is being used to derive the length scale of the land surface characteristics. The wavelet variance derived from the Fast Wavelet Transform using the Haar wavelet is a good indicator for the variability of land surface characteristics at different spatial scales. For three different data sets the length scale of land surface characteristics have been derived: Barrax, Spain, the Jornada Experimental Range, USA and the Central Part of the Netherlands.

The two approaches for quantifying the error due to aggregation have been verified using the three data sets. The results obtained by the linearization show that aggregation error can indeed be estimated. For the three test sites the large scale error did not exceed 10%. However the results based on the convex hull analysis show that the large scale error due to aggregation can be much larger than observed for the three test cases. Therefore low resolution remote sensing data cannot be used a priori as input for land surface models.

Voorwoord

Het afronden van een proefschrift brengt een tweeledig gevoel met zich mee. Enerzijds is er de opluchting dat het proefschrift afgerond is en aan iets nieuws kan worden begonnen. Anderzijds is het ook een afsluiting van een relatief zorgeloze periode waarin ik niet veel meer hoefde te doen dan met mijn onderzoek bezig te zijn. Had het dan niet binnen de vier jaar afgerond kunnen worden? Misschien wel moet ik eerlijk toegeven, maar onderzoek laat zich moeilijk plannen en zorgvuldigheid moet niet worden opgeofferd ten behoeve van snelheid.

Een proefschrift is grotendeels een klus voor een persoon, maar met hulp van anderen neemt zowel de kwaliteit toe als de hoeveelheid werk af. Allereerst wil ik mijn directe begeleider en tevens co-promotor bedanken, Massimo Menenti. Ondanks het feit dat Massimo veelvuldig op reis is, en zijn vaste werkplek in Strassbourg ligt, heb ik hem toch zeer regelmatig en uitputtend kunnen spreken over het proefschrift en aanverwante zaken. Ook is in deze tijd van internet fysieke aanwezigheid ook al geen voorwaarde meer voor vergaderingen. De grootste kwaliteit van Massimo is vooral het vermogen om onderzoek zowel te kunnen plaatsen in breder verband, maar daarbij ook nog oog houdend voor de details. Mijn dank gaat tevens uit naar mijn promotor Prof. Feddes, die er in hoge mate verantwoordelijk voor is dat het proefschrift binnen de vijf jaar is afgerond. Ook is het zijn verdienste dat het proefschrift leesbaar is voor een breder publiek dan een beperkt groepje hydrologen die zich met remote sensing bezig houden.

Iemand die niet vergeten mag worden is de initiator van het geheel, Wim Bastiaanssen. Aan Wim is het danken dat geld voor Strategisch Expertise Onderzoek binnen het (toenmalige) Staring Centrum werd gereserveerd voor een AIO-plaats op het vlak van remote sensing en klimaat. Wim heeft in het eerste jaar van het onderzoek ook gefungeerd als directe begeleider, maar moest daar van af zien nadat hij eerst vertrok voor een half jaar naar Sri Lanka, om vervolgens definitief bij het Staring Centrum te vertrekken. Ook is Wim er verantwoordelijk voor dat ik me al geruime tijd bezig houd met remote sensing ten behoeve van hydrologie. Eerst als afstudeervakker, later als dienstweigeraar en vervolgens als AIO.

Henk van Ledden en Martin Jansen zijn verantwoordelijk voor de figuren in het proefschrift. Hun vakkennis heeft er voor zorg gedragen dat de figuren leesbaar en overzichtelijk zijn geworden. Verder wil ik Karel Soeterik bedanken voor het corrigeren en bewerken van de Landsat TM beelden van Nederland.

The participation in the Jornada Field Experiment also led to a stay of six months at the USDA-ARS Hydrology Lab in Beltsville, MD. I would like to thank all the people at the lab for their cooperation and company during those months, especially Tom Schmugge, Jerry Ritchie, Al Rango and Bill Kustas. During my stay at the hydrolab I had plenty of time to lay down the structure of the thesis. Also I could make fully use of the Jornada data set.

In de zes jaar die ik in totaal bij het Staring Centrum heb gewerkt ben ik zonder van bureaustoel te verwisselen bij drie verschillende afdelingen werkzaam geweest. Ik ben begonnen bij de afdeling waterhuishouding aride gebieden, dat toen viel onder de hoofdafdeling waterbeheer. Zo'n drie jaar geleden is de afdeling waterhuishouding aride gebieden opgegaan in de afdeling ontwikkelingssamenwerking die op zijn beurt vorig jaar is opgenomen in de nieuw gevormde afdeling Bodem en Landgebruik. Uit de naamgeving van de afdelingen zou je kunnen afleiden dat mijn onderzoek steeds verder van de (water)bron is geraakt. Daarbij is het ook binnen het Staring Centrum het type onderzoek van de toenmalige afdeling waterhuishouding aride gebieden minder herkenbaar geworden. Voordeel bij deze reorganisaties is wel dat de groep van collega's die je goed leert kennen steeds groter wordt. Daarentegen blijft het moeilijk je afkomst te verloochenen. Daarom wil ik bij deze de mensen bedanken die de afgelopen jaren min of meer de vaste kern van de afdeling waterhuishouding aride gebieden hebben gevormd, alhoewel nu er een andere, officieuze naam is bedacht nl de Satellite Earth Observation Group: Gerbert Roerink, Zhongbo (Bob) Su en Claire Jacobs. Massimo, Wim en Susanna Azzali zijn de collega's van het eerste uur. Het algemene kenmerk van deze groep mensen is dat er een gezonde afkeer bestaat tegen vergaderen en daarmee een hoge mate van flexibiliteit in de besluitvorming kennen, waar ik me altijd in heb kunnen vinden.

Natuurlijk zijn er veel meer collega's geweest op het Staring Centrum die ik zou willen bedanken voor hun collegialiteit en behulpzaamheid, maar om niemand te vergeten, wordt een ieder die zich nu aangesproken voelt hartelijk bedankt.

Contents

List of symbols v

1 Introduction 1
- 1.1 Spatial and temporal scales of atmospheric and hydrological processes . . . 1
  - 1.1.1 Process scale . . . 3
  - 1.1.2 Observation scale . . . 3
- 1.2 Description of land surface processes in atmospheric models . 5
  - 1.2.1 Model scale . . . 6
  - 1.2.2 Land surface model . . . 6
  - 1.2.3 Soil water content . . . 6
  - 1.2.4 Remote sensing of soil water content . . . 7
- 1.3 Aggregation of wetness indicators . . . 8
- 1.4 Outline . . . 11

2 Parameterization of land surface processes 13
- 2.1 Surface energy balance . . . 13
- 2.2 Turbulent surface energy flux densities . . . 14
- 2.3 Flux profile relationships for the surface layer . . . 18
- 2.4 Flux profile relationships for the atmospheric boundary layer 21
  - 2.4.1 Mean profiles in the outer layer . . . 22
  - 2.4.2 Mean profiles for the atmospheric boundary layer . . . 23
- 2.5 Combination equation for evaporation . . . 24
- 2.6 Surface Energy Balance Index (SEBI) . . . 26

3 Spatial aggregation of radiometric observations 33
- 3.1 Aggregation of spatially distributed variables . . . 33
- 3.2 Aggregation analysis by linearization . . . 37
  - 3.2.1 Model with one variable ($n = 1$) . . . 37
  - 3.2.2 Model with two or more variables ($n \geq 2$) . . . 38
- 3.3 Aggregation analysis using convexity approach . . . 39

4 Wavelet analysis **47**
4.1 The Fourier transform 48
4.1.1 The Fast Fourier Transform (FFT) 49
4.1.2 The windowed Fourier transform 50
4.2 The continuous wavelet transform 50
4.3 The discrete wavelet transform 53
4.3.1 The orthogonal wavelet transform 53
4.4 The fast wavelet transform 56
4.4.1 Fast wavelet transform for images 58
4.5 Multi scale analysis 58
4.6 Wavelet variance 61
4.7 Length scale analysis by means of wavelet analysis 64

5 Description of the study areas **69**
5.1 Barrax 69
5.1.1 Location and climate 69
5.1.2 Field data 71
5.1.3 Remote sensing data 72
5.2 Jornada Experimental Range 73
5.2.1 Location and climate 73
5.2.2 Field data 77
5.2.3 Airborne remote sensing data 78
5.3 The Netherlands 80
5.3.1 Location and climate 80
5.3.2 Field data 81
5.3.3 Remote sensing data 85

6 Length scale analysis **87**
6.1 Case study Barrax 87
6.1.1 Wavelet analysis 87
6.2 Case study Jornada Experimental Range 89
6.2.1 Wavelet analysis 89
6.3 Case study The Netherlands 91
6.3.1 Wavelet analysis 92
6.4 Optimal sensor resolution 98

7 Aggregation of land surface characteristics **101**
7.1 Case study Barrax 102
7.1.1 Application of SEBI 102
7.1.2 Impact of spatial resolution of input data on SEBI results 104
7.1.3 Linearization approach 109
7.1.4 Convex hull approach 114
7.2 Case study Jornada Experimental Range 118
7.2.1 Linearization approach 120

7.2.2 Convex hull approach 122
7.3 Case study The Netherlands 123
7.3.1 Linearization approach 123
7.3.2 Convex hull approach 125
7.4 Conclusions 127

Summary and conclusions **129**

Samenvatting en conclusies **137**

Bibliography **145**

Curriculum Vitae **151**

List of symbols

Symbol	Interpretation	Unit
β_{xi}	Stability parameter	-
β_{yi}	Stability parameter	-
$\delta_{x,agg}$	Relative error due to aggregation for variable x	%
$\overline{\delta}_{x,agg}$	Overall relative error due to aggregation for variable x	%
$\Delta_{x,agg}$	Error due to aggregation for variable x	-
$\overline{\Delta}_{x,agg}$	Overall error due to aggregation for variable x	-
γ	Psychometric constant	Pa K^{-1}
ε_0	Surface emissivity	-
ε'	Apparent emissivity	-
η_i	Stability parameter	-
θ	Potential temperature	K
θ_h	Potential temperature at boundary layer height	K
θ_v	Virtual potential temperature	K
θ_{v0}	Virtual potential surface temperature	K
θ^*	Temperature scale	K
κ	Wavenumber	m^{-1}
λ	Latent heat of evaporation	J kg^{-1}
λE	Latent heat flux density	W m^{-2}
Λ	Evaporative fraction	-
μ_i	Stability parameter	-
ν_0	Stability parameter	-

continued on next page...

Symbol	Interpretation	Unit
ν_i	Stability parameter	-
ξ	Stability parameter	-
ρ_a	Air density	kg m^{-3}
σ	Stefan Boltzmann constant	W m^{-2} K^{-4}
$\hat{\sigma}^2_{f,j}$	Wavelet variance of function f at scale level j	-
$\hat{\sigma}^2_{fg,j}$	Wavelet covariance of function f and g at scale level j	-
τ	Transmissivity	-
$\phi_e(\xi)$	Monin Obukhov function for water vapor transfer	-
$\phi_h(\xi)$	Monin Obukhov function for heat transfer	-
$\phi_j[n]$	Discrete wavelet function at scale level j [integer ≥ 0]	-
$\phi_m(\xi)$	Monin Obukhov function for momentum transfer	-
$\phi_{u,s}(x)$	Continuous wavelet function with translation u and scale s	-
Φ_{be}	Stability function for vapor transfer in the ABL	-
Φ_{bh}	Stability function for heat transfer in the ABL	-
$\psi_e(\xi)$	Stability function for water vapor transfer	-
$\psi_h(\xi)$	Stability function for heat transfer	-
ω	Frequency	s^{-1}
a_0	Constant in z_{0m}-$NDVI$ relationship	m
a_h	Constant in θ-profile function for the ABL	-
a_v	Constant in q-profile function for the ABL	-
$\overline{A}$	Mean of turbulent property A	-
A'	Deviation from the mean of turbulent property A	-

continued on next page...

Symbol	Interpretation	Unit
b_0	Constant in z_{0m}-$NDVI$ relationship	m
c	Constant in definition of h_r	-
c_0	Constant in Q^*-G_0 relationship	-
c_1	Constant in Q^*-G_0 relationship	-
c_p	Specific heat	J kg^{-1} K^{-1}
c_{pd}	Specific heat for dry air	J kg^{-1} K^{-1}
C	Similarity function for the ABL	-
C_i	Similarity function for the ABL using h_i	-
$C_{i,0}$	Similarity function for the ABL using h_i at zero evaporation	-
$C_{i,max}$	Similarity function for the ABL using h_i at maximum evaporation	-
d_0	Zero displacement height	m
D	Similarity function for the ABL	-
e	Vapor pressure	Pa
e_0	Surface vapor pressure	Pa
e^*	Saturated vapor pressure	Pa
$e_{s,0}$	Saturated vapor pressure at 273.15 K	Pa
E	Evaporation flux density	kg m^{-2} s^{-1}
E_{max}	Maximum evaporation flux density	kg m^{-2} s^{-1}
$\hat{f}(\kappa)$	Continuous Fourier transform of continuous function $f(x)$	-
$\hat{f}[\kappa]$	Discrete Fourier transform of discrete function $f[x]$	-
f	Coriolis parameter	s^{-1}
$f_{z,0}$	Ratio of $z_{0,m}$ and $z_{0,h}$	-
f_{G_0}	Ratio of G_0 and Q^*	-
$\overline{F}$	Average result of function F based on distributed input variables	-
$F(\overline{p})$	Result of function F based on averaged input variable $\overline{p}$	-

continued on next page...

Symbol	Interpretation	Unit
F_V	Lower boundary of the convex hull encompassing function F	-
$F^\wedge$	Upper boundary of the convex hull encompassing function F	-
g	Acceleration due to gravity	m s^{-2}
G	Geostrophic velocity	m s^{-1}
G_0	Soil heat flux density	W m^{-2}
h	Boundary layer height	m
h_i	Observed boundary layer height	m
h_r	Rotational boundary layer height	m
H	Sensible heat flux density	W m^{-2}
H_0	Sensible heat flux density at zero evaporation	W m^{-2}
H_{max}	Sensible heat flux density at maximum evaporation	W m^{-2}
k	Von Karman constant	-
kB^{-1}	$\ln(\frac{z_{0,m}}{z_{0,h}})$	-
K^*	Net shortwave radiation flux density	W m^{-2}
$K^\uparrow$	Outgoing shortwave radiation flux density	W m^{-2}
$K^\downarrow$	Incoming shortwave radiation flux density	W m^{-2}
K_e	Turbulent exchange coefficient for water vapor	m^2 s^{-1}
K_h	Turbulent exchange coefficient for heat	m^2 s^{-1}
ℓ^*	Length scale	m
ℓ^*_{dom}	Dominant length scale	m
L	Monin Obukhov stability length	m
$L^\uparrow$	Outgoing longwave radiation flux density	W m^{-2}
$L^\downarrow$	Incoming longwave radiation flux density	W m^{-2}
$NDVI$	Normalized Difference Vegetation Index	-
$NDVI_{max}$	Maximum NDVI	-

continued on next page...

Symbol	Interpretation	Unit
p	Pressure	Pa
p_0	Surface pressure	Pa
p_h	Pressure at boundary layer height	Pa
q	Specific humidity	kg kg^{-1}
q_h	Specific humidity at boundary layer height	kg kg^{-1}
q^*	Humidity scale	kg kg^{-1}
Q^*	Net radiation flux density	W m^{-2}
r_0	Surface albedo	-
r_a	Aerodynamic resistance	s m^{-1}
$r_{a,0}$	Aerodynamic resistance at zero evaporation	s m^{-1}
$r_{a,max}$	Aerodynamic resistance at maximum evaporation	s m^{-1}
r_e	Resistance to water vapor transfer	s m^{-1}
r_h	Resistance to heat transfer	s m^{-1}
r_s	Surface resistance	s m^{-1}
R_d	Gas constant for dry air	J kg^{-1} K^{-1}
R_v	Gas constant for moist air	J kg^{-1} K^{-1}
s	Slope of the vapor pressure curve	Pa K^{-1}
t	Time	s
T	Temperature	K
T_0	Surface temperature	K
T_a	Air temperature	K
$(T_0 - T_a)_0$	Temperature difference at zero evaporation	K
$(T_0 - T_a)_{max}$	Temperature difference at maximum evaporation	K
u	Horizontal component of wind speed	m s^{-1}
u_g	x-component geostrophic velocity G	m s^{-1}
u^*	Friction velocity	m s^{-1}
v_g	y-component geostrophic velocity G	m s^{-1}

continued on next page...

Symbol	Interpretation	Unit
w	Vertical component of wind speed	$\mathrm{m\ s^{-1}}$
$Wf(u,s)$	Continuous wavelet transform	-
$Wf[n]$	Discrete wavelet transform	-
W_u	Relative humidity	-
x	Distance	m
z	Height above the surface	m
z_{0h}	Roughness length for heat	m
z_{0m}	Roughness length for momentum	m
z_{0v}	Roughness length for water vapor	m

Chapter 1

Introduction

1.1 Spatial and temporal scales of atmospheric and hydrological processes

Atmospheric and hydrological processes occur at a wide range of both temporal and spatial scales. Temporal scales range from seconds (10^0 s) to years (10^8 s), whereas spatial scales range from centimeters (10^{-2} m) to thousands of kilometers (10^6 m). The limits show that atmospheric and hydrological processes span about eight orders of magnitude in both space and time (Klemeš, 1983). Figure 1.1 shows a graphical overview of the spatial and temporal scale of several important hydrological and atmospheric processes.

The gray tones in Figure 1.1 show where most of the kinetic energy is present for the atmospheric and hydrological processes depicted. The time scale indicates whether processes are slow or fast, whereas the length scale indicates whether processes have a large or small spatial extent.

Processes related to (subsurface) hydrology can be characterized by small spatial scales (small spatial extent) together with a large temporal scale (slow processes). On the other hand processes related to the atmosphere have larger spatial scales (larger spatial extent) and smaller temporal scales (faster processes). In Figure 1.1 one can see that the temporal and spatial scale of atmospheric and hydrological processes are clearly separated. The description of atmospheric and hydrological processes in numerical models is therefore scale dependent, owing to the combination of non-linear dynamics, with regard to their temporal and spatial variability (Dyck and Baumert, 1991). Regional hydrological models will have small spatial intervals and relatively large time intervals, due to the nature of the hydrological processes. Atmospheric models will have larger spatial intervals and smaller time intervals than aforementioned hydrological models. Due to this scale discrepancy it is difficult to couple these two types of models. Milly and Dunne (1994) stated that a unified physical theory of land-atmosphere interactions, including both meteorological and hydrological components, cannot escape

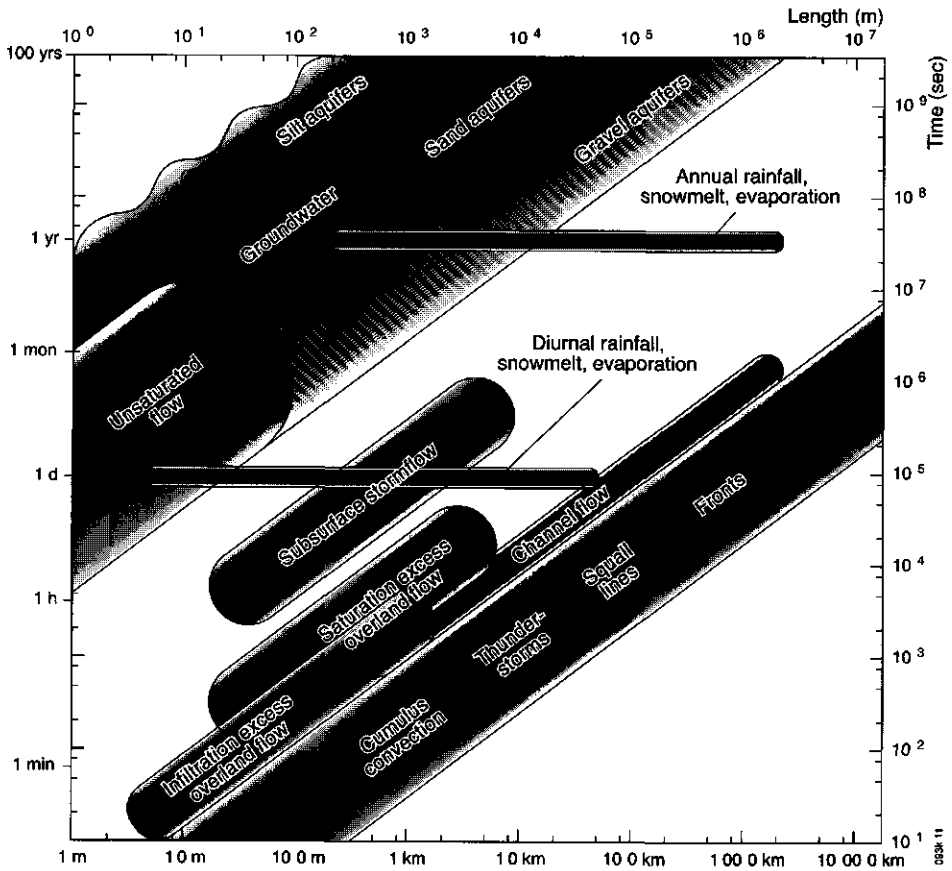

Figure 1.1: Atmospheric and hydrological processes at a range of characteristic temporal and spatial scales after Blöschl and Sivalapan (1995).

the difficulties arising from the many different scales that are either inherent in the system or imposed by our way of looking at it.

Scale is not a trivial notion: many definitions exist depending on the context where it is being used. In order to get some clarity on the concept of scale, three types of scale, each of them related to some step in the modeling process, can be distinguished: process scale, observation scale and model scale (Blöschl and Sivalapan, 1995). First the process and observation scale will be discussed, later on the model scale will be introduced.

1.1.1 Process scale

The process scale of a hydrological or atmospheric process can either be related to the temporal or the spatial scale. The term scale has been used to describe different properties of hydrological and atmospheric processes:

- Scale can refer to the lifetime (**duration**) or spatial extent (**coverage**) of an event in time respectively in space. It can be used to describe short-lived events like the duration of the peak-flow during floods. See Figure 1.2a
- The term spatial or temporal **period** can be used to describe periodic processes. The dominant spatial or temporal period will correspond with the peak value in a spectral power plot. Most of the spatial or temporal variability is present at that particular scale. See Figure 1.2b.
- The third definition of the process scale is the **correlation length.** It has been used for processes that exhibit some kind of spatial or temporal correlation. The correlation length refers to the distance between points at which the autocorrelation is smaller than a predefined threshold value (usually taken as 0). Sometimes the term **integral scale** is used instead of correlation length. See Figure 1.2c.

Processes can exhibit more than one typical process scale. In a spectral power plot more than one peak would show up. Also a process can have no distinct spatial or temporal scale implying that the spatial or temporal variability is spread regularly across a large range of scales.

1.1.2 Observation scale

The scale of observation depends on the method of observation and instrumentation characteristics. The definitions of the observation scale are similar to those being used to describe the process scale:

- Spatial or temporal **extent**: The total distance or amount of time over which data has been sampled defines the spatial or temporal extent also known as coverage, expressed in area or time units. See Figure 1.3a.

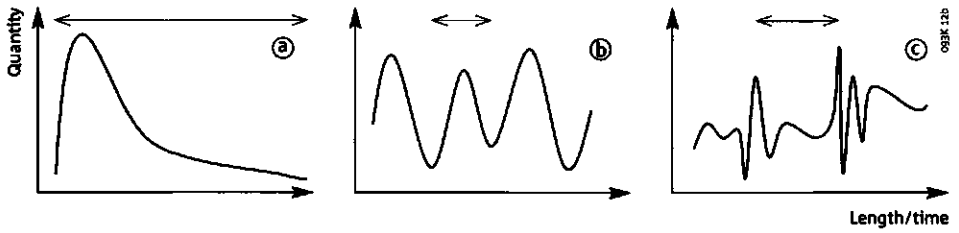

Figure 1.2: a) Duration or coverage of a process, b) period of a process, c) correlation length or integral scale of a process.

- Temporal or spatial **resolution**: The temporal or spatial resolution is defined by the interval at which the data is sampled. See Figure 1.3b.
- **Integration** volume or time. The integration volume is the volume for which the measurement is valid. The integration time is the time that it takes to conduct a single measurement. See Figure 1.3c.

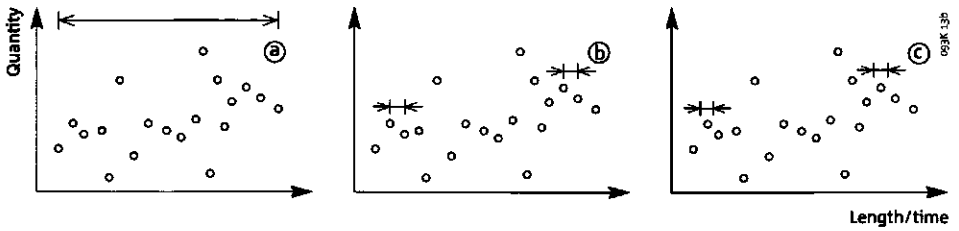

Figure 1.3: a) Extent of an observation, b) resolution of an observation, c) integration volume or time of an observation.

The spatial or temporal resolution has a great impact on how processes are being monitored. Processes should be observed preferably at a scale smaller or at least equal to the process scale. Unfortunately this is seldom true. For example rainfall is measured routinely on a daily basis at most rainfall stations, whereas rainstorms hardly ever last longer than a day, see Figure 1.1.

The observation scale can have consequences for the quality of the data and comprehension of processes. A process with a process scale larger than the spatial or temporal extent of the observation appears as a trend in the data. Whereas a process with a process scale smaller than the spatial or temporal resolution of the observation will appear as noise in those data.

In the following sections first a general introduction to atmospheric models is given with specific interest to land surface models which describe the coupling of atmospheric and hydrological processes. It will be shown that

soil water content is an important variable in land surface models. The use of remote sensing data for providing input maps of soil water content for land surface models is discussed. Finally the central research question will be defined, and an outline of the thesis given.

1.2 Description of land surface processes in atmospheric models

An atmospheric model is a 3-dimensional model, describing the transport of momentum, water and heat in the atmosphere. It determines climatic quantities such as temperature, snow cover, precipitation, soil water content and cloud cover. Within the model the surface of the earth is divided into coarse grid cells whereas the atmosphere is divided into several layers with variable height. In the lowest layer the interaction between atmosphere and surface is modeled. There are two different applications of atmospheric models: weather forecasting and climate research.

- The atmospheric models used in climate research are generally known as Global Circulation Models (GCM). A GCM is usually integrated for very long periods (up to 1000 years) and has a coarse resolution for the surface grid (typically 2.5° × 2.5°, which corresponds with ≈ 275 km × 275 km on the equator). Important for the success of the simulation is the adequate physical parameterization of the most significant processes. Land surface boundary conditions have great impact on the model results (Garrat, 1993).

- For the purpose of weather forecasting, atmospheric models are integrated for a period of up to 10 days, having a minimal resolution of about 50 x 50 km (meso scale model). This type of model is known as Numerical Weather Prediction Model (NWPM). In operational applications a NWPM will be run a few times per day. The success of a NWPM, besides an adequate parameterization of the processes, depends on a reliable estimate of the actual state of the atmosphere, oceans and the land surface (van den Hurk et al., 1997).

As stated before, the performance of a NWPM depends on a proper initialization of the model state. This initialization consists of a blend between the model forecast in the past and observations of the present state of the atmosphere and land surface. The quality of the initial data and the blending process (data assimilation) are the major features determining the prediction skill of a NWPM. Since data assimilation is nearly continuous in time, the model is kept in the right track by the data. Therefore, for a NWPM, the continuous availability of reliable global data is crucial for the determination of the initial state of the model. Another concept of scale has to be introduced here: the model scale.

1.2.1 Model scale

The model scale is the intermediate scale between the observation and process scale. A model describes processes, and therefore is bound to the process scale. However observations are used as input for models and this fact will also constrain the model scale. Therefore the model scale is partly related to processes and partly to the observations available. Unfortunately in most cases the process scale does not coincide with the observation scale. To bridge that gap, observations have to be (dis)aggregated. Information about the scale of processes has to be known a priori in order to (dis)aggregate properly.

1.2.2 Land surface model

A Land Surface Model (LSM) associated with a NWPM or GCM simulates the exchange of heat, moisture and momentum between atmosphere and land surface, i.e. the surface energy balance. The surface energy balance describes the partitioning of net radiation flux density (Q^*) into soil heat flux density (G_0), sensible heat flux density (H) and latent heat flux density (λE). The processes described in the LSM vary over smaller length scales than the large scale circulation patterns, and possibly smaller than the model grid cell size. However those small scale land surface processes have a significant influence on the large scale circulation patterns. The partitioning of net available energy ($= Q^* - G_0$) into λE and H has an impact on the formation of clouds and as a consequence on the amount of precipitation, the radiation balance and the distribution of water vapor in the atmosphere.

The partitioning of net available energy into λE and H is to a large extent controlled by the availability of soil water. Soil water content is therefore among the most significant parameters for a reliable surface flux description (Shukla and Mintz, 1982; Milly and Dunne, 1994). However in most NWPMs the soil water content does not have a physical meaning, but is used as memory of the system and as a controller of the energy partitioning. Depending on the type of land surface model used in the NWPM, even a properly estimated soil water content may lead to an erroneous surface energy partitioning because the coupling of water and energy balances on meso scale may not be correctly parameterized.

1.2.3 Soil water content

Traditionally for the determination of the initial state of soil water content NWPMs use a climatological data set of soil water content. A climatological data set has been set up on the basis of long time series of observations of precipitation and surface variables (Claussen et al., 1994; Wilson and Henderson-Sellers, 1985). Both data sets have a global coverage. The data set reflects the average value of soil water content throughout the year. This

could lead to a poor performance of the model in years which are much drier or wetter than average. To solve this problem more advanced models consider soil water content as a prognostic variable. These models use the computed soil water content of the last model run as initialization for the new model run. The danger exists that in the course of time the result tends to drift towards extreme dry or wet weather (Moene et al., 1995). Therefore the ideal situation is to update the soil water content of NWPMs on a regular basis by an independent data source, to prevent drifting, and to reflect better the present state of the soil water content.

Due to the spatial variability of soil physical characteristics and vegetation characteristics, field measurements of the exchange of water and heat between land and atmosphere cannot be considered representative of larger heterogeneous areas. Therefore it is impossible to use field measurements in a direct way to initialize a NWPM. Even for validation of atmospheric models field measurements are not very suitable due to the difference in observation and process scale. Obviously field measurements are not suited for the initialization process. For the purpose of initialization it seems that remote sensing data are a suitable candidate. *Low resolution remote sensing data* have the advantage of a spatial extent much larger than the size of a single NWPM grid cell. Also the high temporal resolution of low spatial resolution imagery is an important factor. Data are available on a daily basis for a large area. On the other hand *high resolution remote sensing data* have a spatial resolution, which is comparable to the process scale of the land surface processes. These data will show much more detail and will give a better view on the variability of land surface processes.

1.2.4 Remote sensing of soil water content

Numerous studies have been conducted to map soil water content using remote sensing data. Especially the use of passive or active microwave sensors has been extensively studied (Jackson, 1997; Engman, 1990). However as mentioned before the soil water content used in land surface models is not a physical variable. Its function in the model is to control the energy partitioning of the net radiation into sensible and latent heat flux and is therefore dependent on the type of parameterization used in the model. A new approach proposed by van den Hurk et al. (1997) updates soil water content using optical and thermal infrared remote sensing data. The remote sensing data are used to determine the surface energy balance of land surfaces. A correction to initial soil water content is calculated from a comparison between the evaporative fraction fields produced by a numerical weather prediction model and the satellite algorithm.

The evaporative fraction (Λ) is an alternative expression of the surface energy balance and is an indicator of water availability (Bastiaanssen, 1995). The evaporative fraction Λ is the ratio between latent heat flux (λE) and the

net available energy ($Q^*-G_0 = \lambda E + H$), i.e. $\Lambda = \lambda E/(\lambda E + H)$. If $\Lambda = 1$, land surface evaporation is maximal, when $\Lambda = 0$, there is no evaporation. The approach using Λ will lead to a better estimation of the surface energy balance by the LSM and, as a consequence, to a better simulation of the atmospheric processes in the NWPM.

Unfortunately remote sensors do not measure surface energy balance fluxes directly. Remote sensing data can provide estimates of land surface characteristics such as surface albedo, vegetation cover and surface temperature. These land surface characteristics can be used to estimate surface fluxes using physical (Taconet et al., 1986) or empirical algorithms (Bastiaanssen, 1995). From the surface fluxes, wetness indicators can be calculated. Wetness indicators describe the relation between latent and sensible heat flux in a simplified manner. The wetness indicator relevant for this study is the evaporative fraction Λ.

The current research will not concentrate on the estimation of the soil water content at the meso scale as such because it does not necessarily yield a proper energy balance. A proper estimation of the energy partitioning is selected as ultimate goal and the soil water content is adapted accordingly, given the formulation of the LSM used in the NWPM. In this way a proper surface energy balance is ensured. As a consequence, information is needed about energy partitioning, i.e. the evaporative fraction Λ, at the size of a NWPM grid cell, or generally speaking for the meso scale. This information can either be obtained from airborne or satellite sensors.

This leads to the following research question:

How to areally aggregate wetness indicators, accounting for their length scales and resolution at which they can be sampled by advanced airborne or satellite sensors, from pixel to meso scale for updating soil water content in a Numerical Weather Prediction Model.

In the following section problems which arise when aggregating wetness indicators will be addressed.

1.3 Aggregation of wetness indicators

Satellite remote sensing data generally have a higher spatial resolution (< 5 km) than the grid cells of a NWPM (> 50 km). Remote sensing data can be used to infer wetness indicators. In order to use wetness indicators as input for a NWPM grid cell, they have to be aggregated to the scale of a NWPM grid cell. However this is not a straightforward procedure. A simple averaging procedure will not work always. This is only possible when the algorithm involved is scale invariant. Hu and Islam (1997) indicated that two aspects play an important role to determine whether the algorithm is

scale invariant or not.

- The scale of observation versus the scale of the processes involved.
- The type of model used to infer wetness indicators from remote sensing data, whether it is linear or non-linear.

In Table 1.1 the combination of both effects on the aggregation process are depicted schematically.

Table 1.1: Effect of observation scale and model type on aggregation process.

Type of model	*Process scale* > *Observation scale*	*Process scale* < *Observation scale*
Linear model	1) Scale invariant aggregation algorithm (linear averaging)	2) Scale invariant aggregation algorithm
Non-linear model	3) Scale invariant aggregation algorithm (conservation principle)	4) **No** scale invariant aggregation algorithm

The four possibilities will be explained here in more detail. Each case will be discussed with regard to the central question in this thesis: the aggregation of wetness indicators, derived from remote sensing data, to the scale of a NWPM grid cell.

1. *Process scale > Observation scale & Linear model.* Here the spatial resolution of the remote sensing data is smaller than the actual process scale. This implies that the total variability present in the landscape with regard to the process is captured. If the wetness indicator can be described as a linear combination of the remotely sensed observations, then linear averaging to any scale is correct. While the remote sensing data are expressed as a radiance flux per unit of area, it does not matter whether the input remote sensing data or the resulting wetness indicators will be aggregated. The aggregation algorithm, in this case linear averaging, is scale invariant.

2. *Process scale < Observation scale & Linear model.* The spatial resolution of the remote sensing data is larger than the actual process scale. The total variability present in the landscape with regard to the process is not captured completely. However in this case remote sensing data are expressed as a radiance flux per unit of area. The remote sensing data can then be interpreted as a correct aggregated value. And while the remote sensing data model is linear, still an average value of

the resulting wetness indicator will give the correct aggregated value. In another case where the input data is not expressed per unit of area a simple linear averaging procedure cannot be used. The aggregation process in this **specific** case is scale invariant.

3. *Process scale > Observation scale & Non-linear model.* The spatial resolution of the remote sensing data is smaller than the actual process scale. The total variability with regard to the process is captured. A simple linear aggregation scheme will not work here, since the algorithm is non-linear. A correct aggregation scheme can be derived by imposing a suitable conservation principle, e.g. conservation of energy. Such a scheme can be applied at all scales and gives a correct result. There will be no error due to aggregation.

4. *Process scale < Observation scale & Non-linear model.* The spatial resolution of the remote sensing data is larger than the actual process scale. The total variability with regard to the process will not be completely captured. Also the wetness indicator cannot be described as linear function of the remotely sensed observations. These two conditions imply that the aggregation process is not scale invariant. Using an aggregation scheme based on a conservation principle an estimate of the error due to aggregation can be given.

The algorithms involved in calculating wetness indicators from remote sensing data are generally non-linear. Field measurements obtained at the EFEDA, European Field Experiment in a Desertification-threatened Area (Bolle et al., 1993) field experiment have been analyzed on the nature of the relationship between surface temperature and surface heat fluxes (Pelgrum and Bastiaanssen, 1997). It is shown that there is *no statistical significant linear relationship* between the surface temperature and any of the surface fluxes. As a consequence low spatial resolution remote sensing data may not be used a priori in surface energy balance algorithms. It also means that in table 1.1 only situation 3) and 4) are applicable in the case of our specific research question.

In order to find the right aggregation procedure it becomes important to know whether low resolution remote sensing data will be sufficient to capture the overall variability present in the landscape. This should be checked with high resolution remote sensing data from which one possibly can infer length scales of land surface processes. In this thesis a technique to infer process scales from remote sensing data will be discussed. In the next paragraph the outline of this thesis will be given.

1.4 Outline

In Chapter 2 the parameterization of land surface processes in land surface models will be discussed. Special interest will be paid to the parameterization of the evapotranspiration. Also the algorithm SEBI (Menenti and Choudhury, 1993) to derive the evaporative fraction Λ from remote sensing data will be presented. The SEBI algorithm uses the land surface characteristics surface albedo, r_0, surface temperature, T_0 and vegetation index, $NDVI$ as input data. These land surface characteristics can be derived from remote sensing data. The SEBI algorithm will be used to derive Λ at different spatial scales, ranging from pixel scale to the scale of the NWPM models.

In Chapter 3 the theory behind the aggregation of land surface characteristics and model results derived from remote sensing data will be discussed. A general framework is presented and the sources of the error due to aggregation are identified. Also two approaches to quantify the error due to aggregation are presented. The first approach is based on the linearization of the underlying model using Taylor series. The second approach is geometrical and uses the convex hull to quantify the possible error due to aggregation.

In Chapter 4 a technique to quantify the length scales of land surface characteristic by means of wavelets will be presented. First the mathematics behind the wavelets is explained. A measure for the length scale of land surface characteristics is given by the wavelet variance. Several wavelets will be tested on their use for detecting length scales.

In Chapter 5 three data sets are described. The first data set is obtained at the Barrax site during the EFEDA experiment in 1991 and consists of high resolution airborne imagery. The Barrax area is characterized by the presence of pivot irrigation systems in an arid area, resulting in a large spatial variability of the land surface. The second data set originates from the Jornada Long Term Ecological Range. This research area is located north of Las Cruces, New Mexico, USA, and characteristic of a natural landscape under a arid climate. High resolution airborne imagery will be used for the analysis. The third data set concerns the Central part of the Netherlands. This landscape is characteristic of a mainly agricultural landscape under a moderate humid climate. For the analysis use will be made of Landsat imagery recorded in the summer of 1995.

Chapter 6 will describe the length scale analysis using wavelet analysis for the three data sets presented in Chapter 5. The wavelet variance will be used as a measure for the length scale. The dominant length scale for all three regions will be identified for the land surface characteristics: r_0, T_0 and $NDVI$. Temporal variability for those three land surface characteristics will be analyzed using the four Landsat images of the Netherlands.

In Chapter 7 the framework developed in Chapter 3 to quantify the error

due to aggregation of heat fluxes and evaporative fraction calculated with the SEBI algorithm will be applied for the three data sets presented in Chapter 5. A comparison between the linearization approach and the convex hull approach identified in Chapter 3 will be made

Finally the summary and conclusions will be presented and a perspective for future research will be given.

Chapter 2

Parameterization of land surface processes

In this Chapter the theory and modeling of land surface processes will be discussed. Special attention will be paid to evapotranspiration. First the surface energy balance is introduced, followed by a definition of the Atmospheric Boundary Layer (ABL). Solutions to estimate the evapotranspiration flux density will be presented for the different layers within the ABL. Finally a solution will be given that is valid for the whole ABL. Based on the latter the Surface Energy Balance Index (SEBI) methodology has been developed. This methodology uses as main input the remotely sensed land surface characteristics of surface albedo r_0, surface temperature T_0 and $NDVI$.

2.1 Surface energy balance

The surface energy balance constraints the transfer of energy between the earth surface and the atmosphere:

$$Q^* = G_0 + H + \lambda E \tag{2.1}$$

Where Q^* is the net radiation flux density (W m^{-2}) received at the surface, being divided into the soil heat flux density G_0 (W m^{-2}), the sensible heat flux density H (W m^{-2}) and the latent heat flux density λE (W m^{-2}). The latent heat of evaporation λ (J kg^{-1}) is the amount of energy needed for the evaporation E(kg m^{-2} s^{-1}). The signs of the flux densities $\{G_0, H, \lambda E\}$ are positive when directed *away* from the surface. Net radiation flux density is positive when directed *towards* the surface. In this formulation the surface is defined as a plane rather than a layer, so heat storage is neglected.

Net radiation flux density can also be written as a sum of radiation terms, i.e. the radiation balance:

$$Q^* = K^{\downarrow} - K^{\uparrow} + L^{\downarrow} - L^{\uparrow} \tag{2.2}$$

The upward radiation terms are denoted with $^{\uparrow}$ and the downward radiation terms with $^{\downarrow}$. The four radiation terms are:

- $K^{\downarrow}$, incoming shortwave radiation flux density (W m^{-2}). $K^{\downarrow}$ has direct and diffuse components. The diffuse component is due to scattering by molecules and suspended particles and, in cloudy conditions, to reflection from clouds (Garrat, 1992). The transmissivity τ (-), is the ratio between the direct shortwave radiation arriving at the surface and the direct shortwave radiation present at the top of the atmosphere.

- $K^{\uparrow}$, outgoing shortwave radiation flux density (W m^{-2}). The surface does not behave as a lambertian reflector, meaning that the reflection changes with view angle. The surface albedo r_0 (-) is the ratio of the outgoing shortwave radiation flux densitiy and the incoming shortwave radiation flux density. The surface albedo can range from 0.05 for water to 0.95 for fresh snow. For vegetation r_0 varies approximately between 0.10 and 0.20 and depends on the type and state of vegetation. Net shortwave radiation flux density K^* (W m^{-2}) is defined as:

$$K^* = K^{\downarrow} - K^{\uparrow} = (1 - r_0)K^{\downarrow} \tag{2.3}$$

- $L^{\uparrow}$, outgoing longwave radiation flux density (W m^{-2}). The Stefan Boltzmann law describes the longwave radiation flux density emitted from the earth surface:

$$L^{\uparrow} = \varepsilon_0 \sigma T_0^4 \tag{2.4}$$

  where T_0 is surface temperature (K) and ε_0 is surface emissivity (-). The Stefan Boltzmann constant σ has a value of 5.67*10^{-8} W m^{-2} K^{-4}. For natural surfaces ε_0 varies between 0.9 and 1.0.

- $L^{\downarrow}$, incoming longwave radiation flux density (W m^{-2}) which is the result from emission of the atmosphere including clouds. Also here the Stefan Boltzmann law can be applied to calculate $L^{\downarrow}$:

$$L^{\downarrow} = \varepsilon' \sigma T_a^4 \tag{2.5}$$

  where ε' is apparent emissivity (-) and T_a is the air temperature (K). The value of ε' ranges between 0.6 and 0.9 based on the concentration of water vapour and dust in the atmosphere and the thermal stratification.

2.2 Turbulent surface energy flux densities

The sensible and latent heat flux densities, H and λE, are turbulent flux densities. Turbulent processes are responsible for the vertical transport of heat

and vapor in the atmospheric boundary layer, as well as in other directions. Within the ABL land surface processes influence most of the atmospheric processes. Garrat (1992) gives the following practical definition for the atmospheric boundary layer:

> The atmospheric boundary layer is the layer of air directly above the Earth's surface in which the effects of the surface are felt directly on time scales less than a day, and in which significant flux densities of momentum, heat or matter are carried by turbulent motions on a scale of the order of the depth of the boundary layer or less.

The atmospheric boundary layer itself also can be divided into several distinct layers. Figure 2.1 shows a schematic boundary layer based on descriptions by Garrat (1992) and Brutsaert (1982). The ABL is divided into two large layers:

- The inner surface layer where the structure of the flow is mainly dependent on land surface characteristics. It is a fully turbulent layer where the vertical turbulent flux densities do not change with height when a homogeneous surface is considered. For a heterogeneous surface the vertical length scale also depends on the horizontal length scale (McNaughton and Raupach, 1996).
- The outer layer where the structure of the flow is less dependent on the nature of the surface but where the Coriolis force due to the rotation of the Earth is more important. Throughout the outer layer potential temperature θ (K) and specific humidity q (kg kg^{-1}) are constant.

The potential temperature θ is the temperature where the temperature variations due to changes in pressure are removed:

$$\theta = T \left(\frac{p_0}{p} \right)^{\frac{R_d}{c_{pd}}} \tag{2.6}$$

where T is temperature (K), p is pressure (Pa), p_0 is a reference pressure (usually taken to be 100 kPa), R_d is the gas constant for dry air (287.04 J kg^{-1} K^{-1}) and c_{pd} is specific heat for dry air (1004.67 J kg^{-1} K^{-1}).

The transition between inner and outer layer is not abrupt but characterized by an overlapping region. Within the inner layer an interfacial (roughness) layer can be distinguished. This layer is situated directly on top of the land surface and is barely higher than the roughness elements present on the land surface. Within the interfacial layer molecular diffusion is an important process by which heat and mass are exchanged between surface and air.

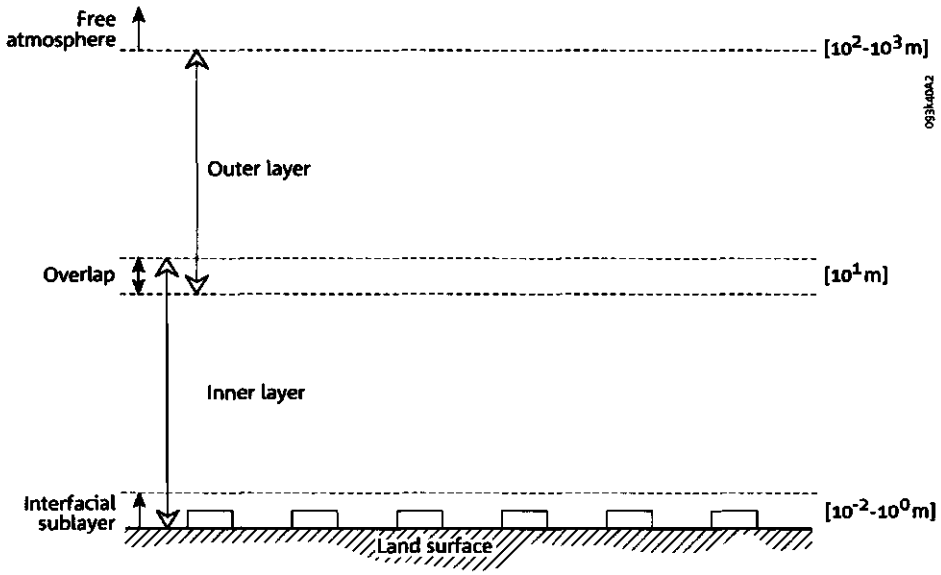

Figure 2.1: Schematic division of the Atmospheric Boundary Layer (ABL).

The height h (m) of the atmospheric boundary layer can vary from a few hundred meters in stable conditions (e.g. nighttime conditions) up to several kilometers in strong convective conditions (e.g. deserts in mid-summer). The surface layer height amounts usually to 10% of the total atmospheric boundary layer height.

The transfers of vapor, momentum and heat within the ABL are turbulent processes. Two major driving forces of turbulence can be distinguished.

- *Shear*: Roughness elements on the land surface cause changes in wind speed perpendicular to the surface. If the gradient of wind speed with height becomes too large the flow will become unstable and will cause turbulence. This turbulence is referred to as either mechanical turbulence or forced convection.

- *Buoyancy*: When the sun is heating the surface, the temperature of the air just above the surface will become higher than the overlying air temperature. Because the air density ρ_a (kg m^{-3}) decreases by increasing temperature, the warm air at the surface tends to rise, while the overlying colder air, due to gravity, tends to sink. To correct the potential temperature for gradients in air density with height the virtual potential temperature θ_v (K) (for unsaturated air) is introduced:

$$\theta_v = (1 + 0.61q)\theta \tag{2.7}$$

The atmosphere where buoyancy is not present is called neutral. When buoyancy is present the atmosphere can either be stable or be non stable. The atmosphere is called stable when the virtual potential temperature at the surface θ_{v0} is lower than the virtual potential temperature of the overlying surface layer θ_v (e.g. nighttime conditions). The atmosphere is called unstable when θ_{v0} is higher than θ_v (e.g. convective conditions).

Turbulence can be described using a notation developed by Reynolds (1894): the turbulent variables are decomposed into a mean and a turbulent fluctuation. The turbulent fluctuation is the deviation from the mean. For instance the turbulent variable A can be described as:

$$A = \overline{A} + A' \tag{2.8}$$

where A is the value of a certain turbulent variable at time t, $\overline{A}$ the average of A over a certain time period and A' the deviation of A at time t. With meteorological measurements A is usually averaged over a period of 15 to 30 minutes. An important property of the Reynolds' notation is, when A and B are both turbulent variables:

$$\overline{(AB)} = \overline{A}\,\overline{B} + \overline{A'B'} \tag{2.9}$$

The last right hand side term is equal to the covariance of the two turbulent properties A and B. Hence the average of the product of two turbulent properties introduces an *extra* term.

Evaporation flux density E can be described as the product of the vertical component of the wind speed w (m s^{-1}), with specific humidity q (kg kg^{-1}) and moist air density ρ_a (kg m^{-3}): $w\rho_a q$ (kg m^{-2} s^{-1}). Actually with E being a turbulent property, the average value $\overline{E}$ is a better indicator of the process

$$\overline{E} = \overline{w\rho_a q} = \overline{w\rho_a}\,\overline{q} + \overline{(w\rho_a)'q'} \tag{2.10}$$

Using some of the properties of Reynolds' notation, $\overline{E}$ can be rewritten as:

$$\overline{E} = \overline{\rho_a}\overline{w'q'} \tag{2.11}$$

Replacing q by $c_p(T - T_0)$ where c_p is the specific heat (J kg^{-1} K^{-1}) and further assuming that T_0 is equal to $\overline{\theta}$ yields this definition for the sensible heat flux density $\overline{H}$:

$$\overline{H} = \overline{\rho_a} c_p \overline{w'\theta'} \tag{2.12}$$

For turbulent conditions the equations describing the change of temperature, humidity and wind speed in time are impossible to solve analytically. Numerical solutions are practically not feasible, that is why the Reynolds notation has been introduced. The problem with the description of the turbulent flux densities by means of the Reynolds notation is the introduction of extra terms (see equation 2.9). The number of unknowns is therefore not

longer equal to the number of equations, which makes it impossible to solve: *the closure problem*. The closure problem is a general problem in turbulence studies. To solve the equations describing turbulence is only possible when another set of equations based on a reduced number of variables is being introduced. Dimensional analysis can be applied to reduce the number of variables.

2.3 Flux profile relationships for the surface layer

Dimensional analysis identifies the relevant physical properties of a process. These properties are organized into a *reduced* number of dimensionless quantities. Dimension analysis establishes the possible existence of a functional relationship between these dimensionless quantities. The function itself still has to be determined by experiment (Brutsaert, 1982). The technique of dimensional analysis can also be used to describe the profiles of specific humidity, wind speed and temperature in the lower part of the boundary layer i.e. the inner layer. The relationships derived for this particular problem are called flux profile relationships.

Generally the wind profile is first described, being a prerequisite for the understanding of turbulent transfer of water vapor and heat. In the case of a neutral surface layer (no buoyancy) the wind profile can be described by:

$$\frac{d\overline{u}}{dz} = \frac{u^*}{k(z - d_0)} \tag{2.13}$$

This relation is also known as the logarithmic wind profile law. The gradient of wind speed u (m s^{-1}) with height z (m) is described by the friction velocity u^* (m s^{-1}), which is a measure of shear stress while the von Karman constant k (-) is usually taken as 0.41. The zero displacement height d_0 (m) decreases with decreasing specific leaf area density and becomes negligible at low values of specific leaf area density (Inoue, 1963).

The wind speed at reference height z, $\overline{u}$ can be described by integrating equation 2.13 from the roughness length for momentum z_{0m} (m) to the reference height z:

$$\overline{u} = \frac{u^*}{k} \ln\left(\frac{z - d_0}{z_{0m}}\right) \tag{2.14}$$

Physically z_{0m} can be defined as the height above the surface where the logarithmic wind speed profile decreases to 0.

Equations 2.13 and 2.14 are only valid for neutral conditions in the surface layer, because only turbulence generated by shear stress is considered. Under non-neutral conditions also the turbulence generated by buoyancy should be included. Monin and Obukhov (1954) introduced a dimensionless variable where the effects of both shear stress and buoyancy on turbulence

are included:

$$\xi = \frac{z - d_0}{L} \tag{2.15}$$

The factor ξ (-) is the stability parameter, and L is the Monin-Obukhov length (m), a length scale for mixed convection. The Monin-Obukhov length L is defined as the ratio of mechanical production of turbulent kinetic energy (shear stress) divided by the thermal convective production (buoyancy) of turbulent kinetic energy:

$$L = -\frac{\rho_a u^{*3}}{kg\left[\left(\overline{H}/\overline{\theta}c_p\right) + 0.61\overline{E}\right]} \tag{2.16}$$

where g is the acceleration due to gravity (m s^{-2}). With ξ one can see that turbulence depends on the following physical properties: the height above the surface level, $\{z,\ d_0\}$; the shear stress at the surface $\{u^*,\ \rho_a\}$; buoyancy $\{g,\ \overline{H},\ \overline{\theta},\ c_p,\ \overline{E}\}$. The von Karman constant k and the minus sign were introduced for convenience. The physical meaning of the Monin Obukhov length is that $z = -L$ should be equal to the height in the boundary layer where the contribution of shear stress to turbulence equals the contribution of buoyancy to turbulence. However this is not completely true because the assumption of logarithmic profiles does not hold for the whole atmospheric boundary layer. The Monin Obukhov length is therefore somewhat larger than aforementioned height (Brutsaert, 1982). A typical range of $|L|$ is between 1 and 200 m. Note that L is negative in case of an unstable atmosphere and positive in the case of a stable atmosphere.

The wind profile for the non-neutral surface layer can now be described as:

$$\frac{d\overline{u}}{dz} = \frac{u^*}{k(z - d_0)}\phi_m(\xi) \tag{2.17}$$

The Monin-Obukhov function for momentum transfer, $\phi_m(\xi)$ (-), corrects the wind profile for buoyancy.

For the heat and water vapor profiles equations similar to equation 2.17 have been developed on the basis of the stability parameter ξ:

$$\frac{d\overline{\theta}}{dz} = \frac{\theta^*}{kz}\phi_h(\xi) \tag{2.18}$$

$$\frac{d\overline{q}}{dz} = \frac{q^*}{kz}\phi_e(\xi) \tag{2.19}$$

where $\phi_h(\xi)$ and $\phi_e(\xi)$ are the Monin-Obukhov functions for heat and water vapor transfer respectively. The temperature scale θ^* (K) and humidity scale q^* (kg kg^{-1}) are defined as:

$$\theta^* = -\frac{\overline{H}}{\rho_a c_p u^*} \tag{2.20}$$

$$q^* = -\frac{\overline{E}}{\rho_a u^*} \tag{2.21}$$

Combination of equations 2.18-2.19 and 2.20-2.21 leads to the definition of the sensible heat and evaporation flux densities:

$$\overline{H} = -\rho_a c_p K_h \frac{\partial \overline{\theta}}{\partial z} \tag{2.22}$$

$$\overline{E} = -\rho_a K_e \frac{\partial \overline{q}}{\partial z} \tag{2.23}$$

where K_h and K_e are the turbulent exchange coefficients for heat and water vapor respectively ($m^2\ s^{-1}$):

$$K_h = \frac{kzu^*}{\phi_h(\xi)}; \quad K_e = \frac{kzu^*}{\phi_e(\xi)} \tag{2.24}$$

Several large field experiments on homogeneous land surfaces (Crawford, 1965; Dyer, 1967; Yaglom, 1977) have been conducted to determine $\phi_h(\xi)$ and $\phi_e(\xi)$ with the expressions developed by Dyer and Hicks (1970) being the most frequently used. A distinction is made between unstable and stable conditions.

unstable conditions ($\xi < 0$)	$\phi_h(\xi) = \phi_e(\xi) = (1 - 16\xi)^{-0.5}$	(2.25)
stable conditions ($\xi > 0$)	$\phi_h(\xi) = \phi_e(\xi) = 1 + 5\xi$	(2.26)

Using equations 2.22 and 2.23 to derive H and λE is not recommended, because measurement of derivatives is difficult to perform in practice. A better approach is to discretize equations 2.22 and 2.23, by integrating from z_1 to z_2, where z_2 is defined at a higher level than z_1.

$$H = -\rho_a c_p \frac{\overline{\theta}(z_2) - \overline{\theta}(z_1)}{r_h} \tag{2.27}$$

$$E = -\rho_a \frac{\overline{q}(z_2) - \overline{q}(z_1)}{r_e} \tag{2.28}$$

The resistance to heat transfer, r_h ($s\ m^{-1}$) and the resistance to water vapor transfer, r_e ($s\ m^{-1}$) are defined as the integral of the inverse turbulent exchange coefficients K_h and K_e from z_1 to z_2:

$$r_h = \int_{z_1}^{z_2} \frac{dz}{K_h}; \quad r_e = \int_{z_1}^{z_2} \frac{dz}{K_e} \tag{2.29}$$

The Monin-Obukhov functions are also integrated from 0 to ξ leading to a stability correction ψ_x:

$$\psi_x(\xi) = \int_0^{\xi} \left[\frac{1 - \phi_x(\xi)}{\xi}\right] d\xi \tag{2.30}$$

The subscript x can be replaced by either h or e. Using equations 2.25 and 2.26 leads to the following definitions for the integrated stability functions ψ:

$$\text{unstable conditions } (\xi < 0) \qquad \psi_h(\xi) = \psi_e(\xi) = 2\ln\left[\frac{1+x^2}{2}\right] \tag{2.31}$$

$$\text{with} \qquad x = (1-16\xi)^{0.25}$$

$$\text{stable conditions } (\xi > 0) \qquad \psi_h(\xi) = \psi_e(\xi) = -5\xi \tag{2.32}$$

Inserting the definitions of the stability corrections equations 2.31 and 2.32) in equations 2.27 and 2.28 yields the following definition of the resistance to heat transfer and of the resistance to water vapor transfer:

$$r_h = \frac{\left[\ln\left(\frac{z_2-d_0}{z_1-d_0}\right) - \psi_h\left(\frac{z_2-d_0}{L}\right) + \psi_h\left(\frac{z_1-d_0}{L}\right)\right]}{ku^*} \tag{2.33}$$

$$r_e = \frac{\left[\ln\left(\frac{z_2-d_0}{z_1-d_0}\right) - \psi_e\left(\frac{z_2-d_0}{L}\right) + \psi_e\left(\frac{z_1-d_0}{L}\right)\right]}{ku^*} \tag{2.34}$$

Because the stability function ψ is equal for heat and water vapor transfer, r_h and r_e are equal. Sometimes this common resistance is also referred to as the aerodynamic resistance r_a (s m^{-1}). *Note that the above parameterization is only valid for the surface layer*, which occupies only the lowest 10 percent of the atmospheric boundary layer (Brutsaert, 1982).

2.4 Flux profile relationships for the atmospheric boundary layer

Several attempts have been made to formulate bulk transfer coefficients for heat and mass for the whole atmospheric boundary layer. Basically two different techniques of determining bulk transfer equations for the whole ABL can be distinguished:

- *Asymptotic matching.* With this technique the profiles of the outer layer and the surface layer are being matched (Csanady, 1967; Blackadar and Tennekes, 1968).
- *Simple Joining.* Joining the profile of the outer layer and the surface layer derives the bulk transfer coefficients (Brutsaert and Mawdsley, 1976).

In this thesis the latter technique will be discussed. First the profiles for the outer layer are introduced.

2.4.1 Mean profiles in the outer layer

A formal extension of the Monin-Obukhov model is proposed, but the Monin-Obukhov ϕ functions do not depend only on ξ in the outer layer. Therefore another set of dimensionless variables has to be introduced. Those dimensionless variables are composed of physical properties whose effect on the description of the mean profiles is not negligible at higher elevations.

The first physical property is the height of the boundary layer. Two concepts are in use to describe the boundary layer height:

- *Rotational height scale* h_r (m). This thickness scale is derived for a steady, horizontally homogeneous, and neutral boundary layer. The rotational height scale is defined by:

$$h_r = \frac{cu^*}{|f|} \tag{2.35}$$

  which takes into account the Coriolis forces by means of the parameter f (s^{-1}). This Coriolis parameter represents the influence of the Earth's rotation and depends on the latitude. The value of constant c (-) is still a point of discussion. Values for c range from 0.15 to 0.40 are given in the literature, with the majority of values around 0.20. Garrat (1992) provides an overview of values cited in literature.

- *Observed height scale* h_i (m). The rotational height scale h_r has some major drawbacks. Deardorff (1972) pointed out that even under slightly unstable atmospheric conditions the boundary layer height should be observed, rather than by calculating h_r. So whenever possible measured profiles of mean wind, temperature and specific humidity should be used to infer the boundary layer height h_i.

The other physical property that has to be taken into account for the outer layer is that the pressure gradient may change with height. The vertical gradient of the horizontal pressure gradient, also known as *baroclinity*, affects the turbulence structure. The baroclinicity is related to the horizontal temperature gradients by the thermal wind equations:

$$\frac{\partial u_g}{\partial z} = -\frac{g}{fT}\frac{\partial \overline{T}}{\partial y} \tag{2.36}$$

$$\frac{\partial v_g}{\partial z} = -\frac{g}{fT}\frac{\partial \overline{T}}{\partial x} \tag{2.37}$$

where u_g and v_g are the x and y components of the geostrophic velocity G which is the steady horizontal flow along the isobars.

Six variables for the surface boundary layer have been distinguished $\{z - d_0,\ L,\ h_r,\ h_i,\ \partial u_g/\partial z,\ \partial v_g/\partial z\ \}$ which should be transformed to five

dimensionless variables. Several combinations are possible; one of those possibilities is this parameterization:

$$\eta_i = \frac{(z - d_0)}{L}; \mu_i = \frac{h_i}{L}; \nu_0 = \frac{h_i}{h_r}; \beta_{xi} = \frac{1}{f}\frac{\partial u_g}{\partial z}\nu_0^2; \beta_{yi} = \frac{1}{f}\frac{\partial v_g}{\partial z}\nu_0^2 \qquad (2.38)$$

This combination is suitable when the observed boundary layer height h_i is the predominant thickness parameter. With these parameters the similarity functions ϕ for the profiles of water vapor and air temperature are described by:

$$-\frac{ku^*(z - d_0)\rho_a}{E}\frac{d\bar{q}}{dz} = \phi_{be}(\eta_i, \mu_i, \nu_0, \beta_{xi}, \beta_{yi}) \qquad (2.39)$$

$$-\frac{ku^*(z - d_0)\rho_a c_p}{H}\frac{d\bar{\theta}}{dz} = \phi_{bh}(\eta_i, \mu_i, \nu_0, \beta_{xi}, \beta_{yi}) \qquad (2.40)$$

The subscript b stands for boundary layer. Integration of the equations 2.39 and 2.40 lead to the following laws for the mean profiles:

$$\bar{q}_h - \bar{q} = -\frac{E}{ku^*\rho_a}\Phi_{be} \qquad (2.41)$$

$$\bar{\theta}_h - \bar{\theta} = -\frac{H}{ku^*\rho_a c_p}\Phi_{bh} \qquad (2.42)$$

where $\bar{q}_h$ and $\bar{\theta}_h$ are the specific humidity and potential temperature at the top of the boundary layer. Formulations of the functions Φ_{be} and Φ_{bh} will not be discussed here.

2.4.2 Mean profiles for the atmospheric boundary layer

As stated before the procedure of simple joining the profiles for the outer layer and surface layer will be presented. The hypothesis is that within the overlap region between both layers both profiles are valid. So by joining equations 2.27 and 2.28 which are valid for the surface layer and equations 2.41 and 2.42 which are valid for the outer layer, $\bar{q}_h$ and $\bar{\theta}_h$ in the overlap region can be eliminated. The result is a relationship between the surface flux densities E and H and the remaining external parameters: the values of specific humidity and potential temperature at both the surface and the boundary layer height, indicated by the subscripts s and h respectively:

$$\bar{q}_s - \bar{q}_h = \frac{E}{a_v ku^*\rho_a}[\ln\left(\frac{h}{z_{0v}}\right) - D] \qquad (2.43)$$

$$\bar{\theta}_s - \bar{\theta}_h = \frac{H}{a_h ku^*\rho_a c_p}[\ln\left(\frac{h}{z_{0h}}\right) - C] \qquad (2.44)$$

where a_h (-) and a_v (-) are constants being equal to 1, z_{0v} (m) is the roughness length for vapor, z_{0h} (m) is the roughness length for heat, C and D are

similarity functions. Both roughness lengths can be visualized as the level above d_0 where $\overline{q}$ or $\overline{\theta}$ would assume its surface value if the logarithmic profile were extrapolated downward outside its actual range of validity (Brutsaert, 1982).

Similar to equation 2.27 and 2.28 an alternative expression for the aerodynamic resistance r_a (s m^{-1}) can be derived, ignoring a_h and again assuming that the aerodynamic resistance to heat, r_h is equal to the aerodynamic resistance to vapor r_v:

$$r_a = \frac{\ln\left(\frac{h}{z_{0h}}\right) - C}{ku^*} \tag{2.45}$$

The similarity function is labeled C of which several descriptions are available in literature. Yamada (1976) developed a definition of C:

$$C_i = 12 - 8.335\,(1 - 0.03106\mu_i)^{-\frac{1}{3}} \tag{2.46}$$

where $\mu_i = h_i/L$. The subscript i in equation 2.46 is added because the dominant boundary layer variable in this formulation is the observed boundary layer height, h_i. All other dimensionless variables are ignored.

2.5 Combination equation for evaporation

Another way of solving the latent heat flux density at the Earth's surface is to combine the energy balance (equation 2.1) with the formulation derived by the Monin-Obukhov similarity theory (equations 2.27 and 2.28) leading to a combination equation for the latent heat flux density. An important assumption is that the stability functions for vapor and heat are equal, which implies that r_h and r_e are equal and as mentioned before are referred to as r_a, the aerodynamic resistance, see equations 2.33 and 2.34. The following set of equations have to be combined:

$$Q^* = G_0 + H + \lambda E \tag{2.47}$$

$$H = \rho_a c_p \frac{T_0 - T}{r_a} \tag{2.48}$$

$$\lambda E = \frac{\rho_a c_p}{\gamma} \frac{e_0 - e}{r_a} \tag{2.49}$$

Note that the temperature T has replaced potential temperature θ because in the surface layer they are practically the same. The subscript 0 refers to the surface. Also the latent heat flux density is written as a function of the gradient of vapor pressure e (Pa) instead of specific humidity q. In the above formulation γ is the psychrometric constant (Pa K^{-1}) being defined as:

$$\gamma = \frac{c_p p}{0.622\lambda} \tag{2.50}$$

In a standard atmosphere (T=293 K, p = 101325 Pa) γ has a value of 67 Pa K^{-1}.

The three equations 2.47, 2.48 and 2.49 have four unknowns (H, E, e_0 and T_0). An additional equation is needed to solve above set of equations. Penman (1948) found such a relationship by assuming that the surface was covered with water. Therefore the surface vapor pressure e_0 is equal to the saturated vapor pressure e^* (Pa), which is a function of the surface temperature:

$$e_0 = e^*(T_0) \tag{2.51}$$

Still a problem remains because equation 2.51 is non linear. Penman (1948) used a Taylor-series to linearize equation 2.51 by removing all non-linear terms from the Taylor-series:

$$e^*(T_0) \approx e^*(T) + s(T_0 - T) \tag{2.52}$$

where s is the derivative of e^* at temperature T, sometimes referred to as the slope of the vapor pressure curve (Pa K^{-1}). Substituting equations 2.51 into equation 2.49 and combining those with 2.47 and 2.48 yields the Penman equation:

$$\lambda E = \frac{s r_a (Q^* - G_0) + \rho_a c_p (e^* - e)}{r_a (\gamma + s)} \tag{2.53}$$

Equation 2.53 is only valid for open water surfaces or a surface fully covered by wet vegetation. Monteith (1965) has elaborated the Penman concept to make it also valid for vegetation that is not completely wet. In this parameterization the vegetation is represented by a big leaf. Within this leaf, stomata are present which regulate the evaporation by adjusting the size of their aperture. The aperture depends on air temperature, incoming shortwave radiation, soil moisture availability and vapor pressure deficit. An extra resistance has been introduced to compensate for those effects: r_s the surface resistance (s m^{-1}). Two resistances in series, r_a and r_s now control the latent heat flux density and equation 2.49 changes into:

$$\lambda E = \frac{\rho_a c_p}{\gamma} \frac{e_0 - e}{r_a + r_s} \tag{2.54}$$

This definition of the latent heat flux density leads to the Penman-Monteith equation:

$$\lambda E = \frac{s r_a (Q^* - G_0) + \rho_a c_p (e^* - e)}{r_a (\gamma + s) + \gamma r_s} \tag{2.55}$$

Many land surface models use equation 2.55 to calculate the latent heat flux density. Remote sensing data can be used to get an areal estimation of the latent heat flux density. The next paragraph describes an algorithm that solves the energy balance based on a modified form of the Penman-Monteith equation using r_0 and T_0 as input, where r_0 and T_0 are derived from remote sensing data.

2.6 Surface Energy Balance Index (SEBI)

The Penman-Monteith equation (equation 2.55) forms the basis of the surface energy balance index (SEBI) method (Menenti and Choudhury, 1993). SEBI uses a modified form of the Penman-Monteith equation together with the formulation of the mean profiles for the whole atmospheric boundary layer to map the evapotranspiration on a regional basis.

Within SEBI the temperature difference between surface and air, $T_0 - T_a$ is chosen as the indicator of actual evaporation. The Penman-Monteith equation can be used to derive theoretically values of $T_0 - T_a$ for zero and maximum evaporation. The observed $T_0 - T_a$ can then be used to estimate the actual evaporation. Substituting equations 2.48 and 2.55 into 2.1 gives the following definition of $T_0 - T_a$ in relation to other variables relevant to land surface evaporation:

$$T_0 - T_a = \frac{[(r_a + r_s)/\rho_a c_p](Q^* - G_0) - (1/\gamma)(e^* - e)}{1 + s/\gamma + r_s/r_a} \tag{2.56}$$

In Equation 2.56 r_s can be seen as an internal resistance to evaporation. The evaporation process at the land surface in the case of actual evaporation does not take place at the land surface itself, but at an evaporation front. This evaporation front is the interface between liquid water and moist air. The moist air is vapor saturated in this case. Two flow regions results: one between evaporation front and land surface and one between land surface and some reference level in the atmosphere (Menenti and Choudhury, 1993). The first flow region is constrained by r_s, the second by r_a. Only when the evaporation front lies at the land surface, i.e. when $r_s = 0$, there will be maximum evaporation E_{max}. Note that in this thesis maximum evaporation is not the same as potential evaporation. Potential evaporation is defined as the evaporation of a reference surface fully covered by vegetation and with no moisture stress. The maximum evaporation is defined as the evaporation when $\Lambda = 1$, and is therefore dependent on the amount of net available energy present at the surface.

Equation 2.56 can be used to calculate the limits of $T_0 - T_a$ corresponding with maximum and zero evaporation. When the surface resistance r_s becomes 0 there will be maximum evaporation. The associated temperature difference $(T_0 - T_a)_{max}$ is:

$$(T_0 - T_a)_{max} = \frac{[r_{a,max}/\rho_a c_p](Q^* - G_0) - (1/\gamma)(e^* - e)}{1 + s/\gamma} \tag{2.57}$$

When the surface resistance r_s becomes infinite, there will be zero evaporation. The associated temperature difference $(T_0 - T_a)_0$ will then be:

$$(T_0 - T_a)_0 = \frac{r_{a,0}}{\rho_a c_p}(Q^* - G_0) \tag{2.58}$$

Two new versions of the aerodynamic resistance are introduced, $r_{a,max}$, the aerodynamic resistance coupled with maximum evaporation (s m^{-1}) and $r_{a,0}$, the aerodynamic resistance coupled with zero evaporation (s m^{-1}) .

The ratio of actual and maximum evaporation, i.e. the evaporative fraction Λ, can now be written as :

$$\Lambda = \frac{E}{E_{max}} = 1 - \frac{H - H_{max}}{H_0 - H_{max}} \tag{2.59}$$

In Equation 2.59 H_{max} is defined as the sensible heat flux density at maximum evaporation (W m^{-2}) and H_0 as the sensible heat flux density at zero evaporation (W m^{-2}). Using Equation 2.48 the temperature differences can be used to derive Λ:

$$\Lambda = \frac{E}{E_{max}} = 1 - \frac{(T_0 - T_a)/r_a - (T_0 - T_a)_{max}/r_{a,max}}{(T_0 - T_a)_0/r_{a,0} - (T_0 - T_a)_{max}/r_{a,max}} \tag{2.60}$$

Actual evaporation is a simple function of surface temperature only if every other land surface property remains constant. However T_a changes with T_0 and is not valid to use as a constant in equation 2.60. Therefore (Menenti and Choudhury, 1993) proposed using the potential temperature at boundary layer height, θ_h instead of T_a, because θ_h is constant for a large area and does not change with T_0. Figure 2.2 shows the possibility of using (remotely) observed T_0 values together with theoretically derived values of $T_0 - T_a$ for maximum and zero evaporation, $(T_0 - T_a)_{max}$ and $(T_0 - T_a)_0$ respectively, to scale the land surface evaporation. This is the general principle behind SEBI.

In equation 2.60 T_0 can be derived from thermal infrared remote sensing data. Still besides remotely sensed T_0 a lot more additional input is needed to solve equation 2.60. In the remainder of this section for each of the terms presented in equation 2.60 will be explained how to derive them, using either remote sensing data or field measurements and assimilation data sets. The variables derived from field measurement and assimilation data sets are said to be constant for the area under consideration.

An assimilation data set is generated from two sources of input data. For a large number of atmospheric variables, observations are mixed with output from numerical weather prediction models or global climate models.

In order to discriminate between variables who have to be measured in-situ and those who have to be derived from remote sensing data the following notation is used. Variables typeset in bold face have to be obtained from field measurements or data assimilation. The spatial variables which can be derived from remote sensing data are denoted with (x,y). At the end of this section an overview will be given of all input variables needed to run SEBI.

- $(T_0 - T_a)$

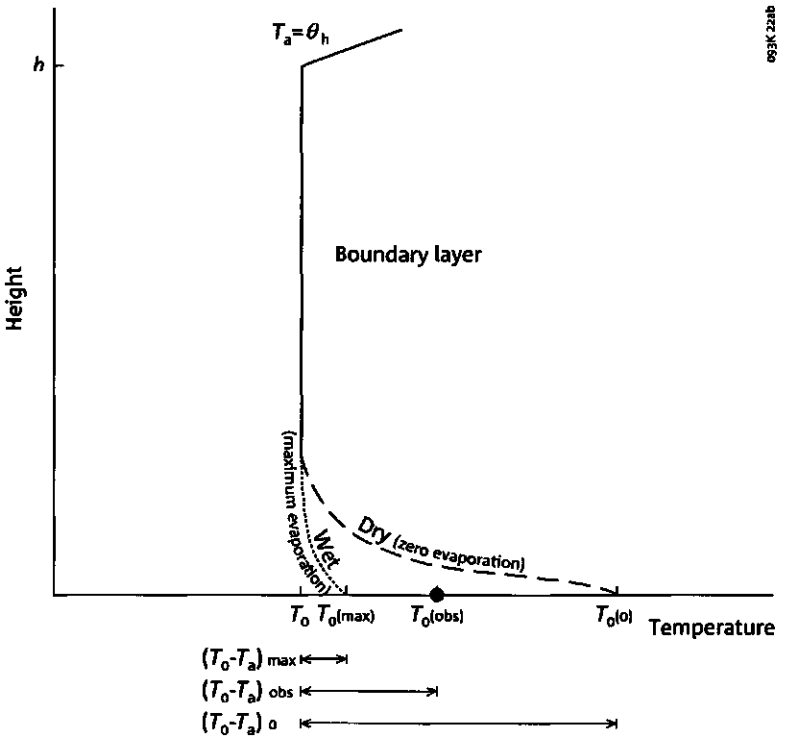

Figure 2.2: Illustration of the principle behind the SEBI algorithm. The observed temperature difference, $(T_0 - T_a)_{obs}$ is used as an indicator for the evaporative fraction, Λ. The two theoretically derived temperature differences, $(T_0 - T_a)_0$ and $(T_0 - T_a)_{max}$ for respectively zero and maximum evaporation give the natural range for Λ.

First the observed surface temperature T_0 should be converted to potential temperature θ using equation 2.6. Then the observed temperature difference reads:

$$(T_0 - T_a) = T_0(x,y)\left(\frac{p_0}{p_s}\right)^{0.286} - \theta_h \tag{2.61}$$

The reference pressure p_0 is 100 kPa.

- $r_{a,0}$ and $r_{a,max}$

  The Monin-Obukhov relationships derived for the whole boundary layer (see paragraph 2.4, equation 2.45) should be used to calculate $r_{a,0}$ and $r_{a,max}$. In equation 2.45 the similarity function C_i is a function of the dimensionless variable $\mu_i = h_i/L$). Values for μ_i which are used to define the maximum and zero evaporation are:

  Maximum evaporation: $\mu_i = 0$
  Zero evaporation: $\mu_i = -150$

  A large negative value of μ_i is sufficient instead of a value of $-\infty$, because $dC_i/d\mu_i$ goes asymptotically to 0. C_i is now given by equation 2.46. The two resistances are defined as:

$$r_{a,0} = \frac{\ln\left(\frac{h_i}{z_{0,h}}\right) - C_{i,0}}{ku^*} \tag{2.62}$$

$$r_{a,max} = \frac{\ln\left(\frac{h_i}{z_{0,h}}\right) - C_{i,max}}{ku^*} \tag{2.63}$$

  The roughness length for heat, $z_{0,h}$ is parameterized in SEBI using the $NDVI$. First the roughness length for momentum, $z_{0,m}$ is derived using an empirical relationship with the $NDVI$, $z_{0,m}$ is then converted to $z_{0,h}$ using a factor f_{z_0}:

$$z_{0,h} = f_{z_0} z_{0,m} = f_{z_0}\left(a_0 + \frac{1}{2}\left(\frac{NDVI(x,y)}{NDVI_{max}}\right)^{b_0}\right) \tag{2.64}$$

  where $NDVI_{max}$ is the maximum $NDVI$ value possible (≈ 0.9), $a_0 = 0.005$ m and $b_0 = 2.5$ m. The last two constants are still a point of discussion. The factor f_{z_0} accounts for the difference between $z_{0,m}$ and $z_{0,h}$ and is highly variable for different land surfaces.

- $(T_0 - T_a)_0$

  The temperature difference at zero evaporation, $(T_0 - T_a)_0$ is given by equation 2.58. Only the net available energy $Q^* - G_0$ is still unknown. Net radiation flux density Q^* is given by:

$$Q^* = (1 - r_0(x,y))\, \boldsymbol{K}^{\downarrow} + \boldsymbol{L}^{\downarrow} - \varepsilon\sigma T_0(x,y)^4 \tag{2.65}$$

  where the surface emissivity ε_0 is given by van de Griend and Owe (1993):

$$\varepsilon_0 = 1.009 + 0.047 \ln(NDVI(x,y)) \tag{2.66}$$

  The ratio of G_0 and Q^*, f_{G_0} is described as:

$$f_{G_0} = c_0 + (c_1 - c_0)\left(1 - \frac{NDVI(x,y)}{NDVI_{max}}\right) \tag{2.67}$$

  where $c_0 = 0.05$ the ratio of G_0 and Q^* for vegetation (Monteith, 1973) and $c_1 = 0.30$ the ratio of G_0 and Q^* for bare soil (Fuchs and Hadas, 1972). The net available energy, $Q^* - G_0$ can then be written as:

$$Q^* - G_0 = (1 - f_{G_0})Q^* \tag{2.68}$$

- $(T_0 - T_a)_{max}$

  The temperature difference at maximum evaporation is given by equation 2.57. In comparison with equation 2.58 an extra term is included: the vapor pressure deficit $(e^* - e)$. The saturated vapor pressure e^* is given by:

$$e^* = e_{s,0} 10^{\frac{a\overline{T}}{b+\overline{T}}} \tag{2.69}$$

  where a and b are constants, respectively 7.5 and 237.3 and $e_{s,0}$ is the saturated vapor pressure at 273.15 K being 610.7 Pa. The average temperature $\overline{T}$ (°C) is defined as the average temperature of θ_h and T_0:

$$\overline{T} = 0.5 * (\boldsymbol{\theta_h} + T_0(x,y)) - 273.15 \tag{2.70}$$

  Actual vapor pressure e is given by:

$$e = \boldsymbol{p_h} \boldsymbol{q_h} \frac{R_v}{R_d} \tag{2.71}$$

  where R_v is the gas constant for moist air (461.5 J kg^{-1} K^{-1}) and p_h (Pa) and q_h (kg kg^{-1}) are respectively the pressure and specific humidity at boundary layer height h_i.

- r_a

Finally the actual aerodynamic resistance r_a can be estimated using:

$$r_a = \frac{\ln\left(\frac{h_i}{z_{0,h}}\right) - C_i}{ku^*} \tag{2.72}$$

The stability factor C_i is interpolated between $C_{i,0}$ and $C_{i,max}$ by means of $T_0 - T_a$:

$$C_i = C_{i,0} + \frac{(T_0 - T_a) - (T_0 - T_a)_0}{(T_0 - T_a)_{max} - (T_0 - T_a)_0}(C_{i,max} - C_{i,0}) \tag{2.73}$$

In table 2.1 the variables which have to be estimated using either field measurements or data assimilation data sets are given. In Chapter 7 three case studies on the use of SEBI are presented.

Table 2.1: Areally constant input variables for SEBI

Symbol	Description	Unit
h_i	observed boundary layer height	
θ_h	potential temperature at boundary layer height	K
p_h	air pressure at boundary layer height	Pa
q_h	specific humidity at boundary layer height	kg kg^{-1}
p_s	surface pressure	Pa
u^*	friction velocity	m s^{-1}
f_{z_0}	ratio between $z_{0,m}$ and $z_{0,h}$	-
$K^{\downarrow}$	Incoming shortwave radiation flux density	W m^{-2}
$L^{\downarrow}$	Incoming longwave radiation flux density	W m^{-2}

Chapter 3

Spatial aggregation of radiometric observations

In this chapter the aggregation of radiometric observations will be discussed. In this thesis the central objective is: *to derive input fields for land surface models (LSMs) using radiometric observations.* The radiometric observations for this particular case will be replaced by satellite remote sensing data. These data will be used to derive the land surface characteristics surface albedo r_0, surface temperature T_0 and the Normalized Difference Vegetation Index $NDVI$. These land surface characteristics will be used as input for the SEBI model, thereby producing distributed maps of evaporative fraction Λ.

The resolution of the satellite remote sensing is smaller than the LSM grid cell size. Therefore the remote sensing data have to be aggregated. The error due to aggregation from one scale level to another will be quantified using two strategies. The first strategy is only valid for continuous, weakly non-linear models; the second strategy is also valid for highly non-linear, discontinuous models as well. First two methods of aggregation for spatially distributed variables, (e.g. radiometric observations, remote sensing data, land surface characteristics) will be defined.

3.1 Aggregation of spatially distributed variables

The aggregation of spatially distributed variables for use in spatial models is not trivial. Aggregating results obtained from a spatial model from the local scale to a large(r) scale by means of linear averaging can introduce errors. Therefore the results have to be aggregated in a proper way. Already in Chapter 1 the two aspects which influence the aggregation of spatially distributed variables have been mentioned: the heterogeneity of the land surface and the non-linearity of the spatial model. In Figure 3.1 the aggregation of spatially distributed variables is illustrated.

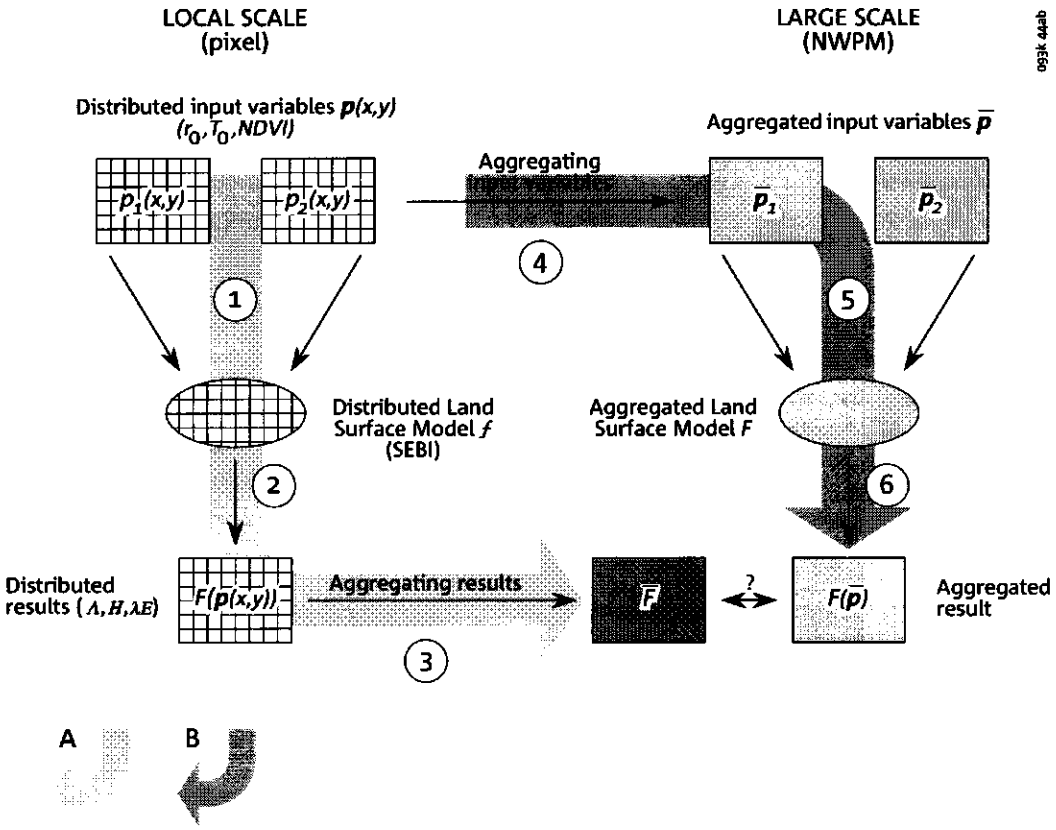

Figure 3.1: Scheme illustrating the aggregation of spatially distributed variables. Path A (arrows 1,2 and 3) illustrates the aggregation of the results which are derived from a distributed model f using distributed input variables. Path B (arrows 4,5 and 6) illustrates the aggregation of input variables before use in an aggregated model F, thereby producing an aggregated result. The corresponding terms for the different parameters of the aggregation process for the case described in this thesis are given within brackets

Two different ways of aggregation from the local scale to a larger scale can be distinguished:

- *the aggregation of the results which are derived from a distributed model f using distributed input variables* (path A in Figure 3.1) and
- *the aggregation of input variables before use in an aggregated model F, thereby producing an aggregated result* (path B in Figure 3.1)

The aggregation of the results is illustrated by path A in Figure 3.1. A distributed model f uses spatially distributed input variables $\boldsymbol{p}(x,y)$ as input (Arrow 1). The spatially distributed input data $\boldsymbol{p}(x,y)$ consists of n variables: $\boldsymbol{p}(x,y) = [p_1(x,y), p_2(x,y), .., p_n(x,y)]$, where $n \geq 1$. Figure 3.1 shows an example with two variables $n = 2$. The results of the distributed model are denoted as $f(\boldsymbol{p}(x,y))$ (Arrow 2). The distributed results $f(\boldsymbol{p}(x,y))$ are then aggregated from the local scale to the large scale resulting in the aggregated result $\overline{F}$ (Arrow 3).

Along path B in Figure 3.1, the spatially distributed input data $\boldsymbol{p}(x,y)$ are averaged from the local scale to the large scale by taking the arithmetic average, resulting in an averaged input $\overline{\boldsymbol{p}}$ (Arrow 4). The averaged input $\overline{\boldsymbol{p}}$ may consist of n averaged input variables: $\overline{\boldsymbol{p}} = [\overline{p}_1, \overline{p}_2, .., \overline{p}_n]$. The averaged input $\overline{\boldsymbol{p}}$ is then used as input in the aggregated model F (Arrow 5). The aggregated model F produces the aggregated result $F(\overline{\boldsymbol{p}})$ (Arrow 6).

$\overline{F}$ and $F(\overline{\boldsymbol{p}})$ will be the same if the distributed model is linear and/or the input data is completely homogeneous. When neither conditions are met a difference between $\overline{F}$ and $F(\overline{\boldsymbol{p}})$ will occur. This is the error due to spatial aggregation by averaging spatially distributed variables. In this chapter the difference between both aggregated results will be quantified using two different strategies.

The aggregation scheme to be applied for the aggregation of radiometric observations to derive input fields for land surface models is described now. The general terms in the scheme have to be replaced by more specific terms. Radiometric observations are the spatially distributed variables in Figure 3.1. The local scale is equal to the resolution of the radiometric observation, whereas the large scale is equal to the size of the NWPM grid cell which is coupled with the LSM. The resolution of the radiometric observations ranges from several meters to kilometers, whereas the NWPM grid cell has a size of at least 25×25 km^2.

To obtain input for LSMs from radiometric observations the distributed model f is divided into two parts. In the first part the radiometric observations are converted by means of conversion algorithms to land surface characteristics such as surface albedo, surface temperature, vegetation index, surface roughness and surface emissivity. In the second part the land surface characteristics are used as input for a LSM. The LSM will produce the surface energy balance for all pixels present in the image. As a result Figure

3.1 will become more complicated. Step 1 (denoted by arrow 1) is now split up into two. First for the conversion of the radiometric observations to land surface characteristics, afterwards for the surface energy balance algorithm.

Both the conversion and the surface energy balance algorithm may be non-linear. In this thesis the local and large scale model, f and F, are assumed identical (identical equations). Therefore only the resolution of the observation will cause differences in $F(\overline{\boldsymbol{p}})$ at different spatial scales.

The variability in the radiometric observations represents the variability present in the landscape. An important remark is that path A in Figure 3.1 will only produce correct results when the total heterogeneity of the land surface has been captured by the radiometric observations. This means that the resolution of the observation should be (much) smaller than the length scale of the land surface processes. In Chapter 4 a technique for determining the length scale of a land surface process using remote sensing data will be discussed.

The aggregation of the distributed high resolution radiometric observations $F(\boldsymbol{p}(x,y))$ to $\overline{F}$(Arrow 3 in Figure 3.1) should be consistent with fundamental physical principles, such as conservation of energy. If the variable that is calculated by the surface energy balance algorithm is a flux density, then arithmetic averaging of all flux densities produces the correct aggregated flux density, because all energy released at the land surface is correctly added up.

Since most land surface models are non-linear and the land surface is never completely homogeneous differences between $\overline{F}$ and $F(\overline{\boldsymbol{p}})$ are likely to occur. The quantification of the difference between $\overline{F}$ and $F(\overline{\boldsymbol{p}})$ is significant for the proper use of land surface models. If the difference is small and within reasonable limits then the model can easily be applied at all scales. When the difference is large the model should be applied only when the scale of the process is smaller or equal to the scale of the observation. In that way the total variability of the landscape can be captured and the individual observations can be considered homogeneous. Two aspects in determining the difference between $\overline{F}$ and $F(\overline{\boldsymbol{p}})$ have to be quantified:

- the influence of the *non-linearity of the model* on the difference between $\overline{F}$ and $F(\overline{\boldsymbol{p}})$
- the influence of the *land surface heterogeneity* on the difference between $\overline{F}$ and $F(\overline{\boldsymbol{p}})$

In this chapter two different approaches for quantifying the above mentioned aspects will be discussed. The first approach is based on a linearization of the land surface model by means of a Taylor expansion (Hu and Islam, 1997). This approach is only valid for continuous functions with a limited degree of non-linearity. The second approach is based on computational ge-

ometry, more precisely the concept of convexity (Raffy, 1994) and is valid for non-continuous functions as well.

3.2 Aggregation analysis by linearization

In the remainder of this chapter the notation presented in Figure 3.1 will be used.

3.2.1 Model with one variable ($n = 1$)

At first the simplest case will be considered where the model F depends on only one distributed variable $p(x,y)(n = 1)$. Note that in this case $p(x,y)$ is a scalar. The model is a continuous function f. The dependent model variable $f(p(x,y))$ can be approximated with a Taylor expansion, neglecting third and higher order terms. Then for any value of $p(x,y)$:

$$f(p(x,y)) = F(\overline{p}) + (p(x,y) - \overline{p}) \left.\frac{\partial f}{\partial p}\right|_{\overline{p}} + \frac{1}{2}(p(x,y) - \overline{p})^2 \left.\frac{\partial^2 f}{\partial p^2}\right|_{p*} \tag{3.1}$$

where $p*$ is a function of $p(x,y)$ and $p* \neq \overline{p}$ due to neglecting higher order terms. Note that f represents a model with distributed input and F a model with aggregated input. In the remainder of this thesis f and F will have the same formulation. The input variable $p(x,y)$ is defined over an area A. Integration over A yields the correct mean of the distributed result:

$$\begin{aligned} \overline{F} = \frac{1}{A}\int_A f(p(x,y))dA = & \underbrace{\frac{1}{A}\int_A F(\overline{p})dA}_{1} \\ & + \underbrace{\frac{1}{A}\left.\frac{\partial f}{\partial p}\right|_{\overline{p}} \int_A (p(x,y) - \overline{p})dA}_{2} \\ & + \underbrace{\frac{1}{2A}\int_A \left((p(x,y) - \overline{p})^2 \left.\frac{\partial^2 f}{\partial p^2}\right|_{p*} \right) dA}_{3} \end{aligned} \tag{3.2}$$

The first term on the right hand side is the value of the dependent model variable calculated with the average of $p(x,y)$ i.e. $\overline{p}$: $F(\overline{p})$. The second term is by definition zero and the third term is then the difference between $\overline{F}$ and $F(\overline{p})$. In the third term both effects of the non-linearity of the model and the heterogeneity of the land surface are incorporated. To separate both effects

the mean value theorem[1] is applied to this term:

$$\frac{1}{2A}\int_A \left((p_{(x,y)} - \overline{p})^2 \left.\frac{\partial^2 f}{\partial p^2}\right|_{p*} \right) dA = \frac{1}{2} \left.\frac{\partial^2 f}{\partial p^2}\right|_{p_x} \frac{1}{A}\int_A (p(x,y) - \overline{p})^2 dA \quad (3.3)$$

The difference introduced by the scaling process can then be defined as:

$$\overline{F} - F(\overline{p}) = \frac{1}{2} kV \quad (3.4)$$

$$\text{where} \quad k = \left.\frac{\partial^2 f}{\partial p^2}\right|_{p_x} \quad \text{and} \quad V = \frac{1}{A}\int_A (p(x,y) - \overline{p})^2 dA$$

The value p_x is realized somewhere in A. The difference between $\overline{F}$ and $F(\overline{p})$ is accounted for by the factors k and V.

The factor k is the difference introduced by the non-linearity of the function f. Note that when f is a linear function the second derivative will be zero, therefore $\overline{F}$ and $F(\overline{p})$ will be identical. The non-linearity term may be found directly from the model, if the function is continuous and therefore differentiable. The non-linearity term cannot be determined exactly because p_x is unknown a priori.

The factor V accounts for the heterogeneity of the variable $p(x,y)$ within the landscape. In the case of only one variable $p(x,y)(n = 1)$, V is equal to the variance of this variable. If $p(x,y)$ is completely homogeneous within the area A, the variance of $p(x,y)$ will be equal to zero. As a consequence $\overline{F}$ and $F(\overline{p})$ will be identical. Chapter 4 will show a method to calculate the variance for different scales.

3.2.2 Model with two or more variables ($n \geq 2$)

Land surface models may have more than one independent variable and radiometric observations in several spectral bands and directions may be used. Therefore the above formulation has to be extended to the case of more than one variable $p(x,y)$. Equation 3.1 will therefore change into the more general case for n variables $p_1(x,y), p_2(x,y), .., p_n(x,y)$:

$$f(\boldsymbol{p}(x,y)) = F(\overline{\boldsymbol{p}}) + (\boldsymbol{p}(x,y) - \overline{\boldsymbol{p}}) \left.\frac{\partial f}{\partial \boldsymbol{p}}\right|_{\overline{\boldsymbol{p}}} + \frac{1}{2}(\boldsymbol{p}(x,y) - \overline{\boldsymbol{p}})^2 \left.\frac{\partial^2 f}{\partial \boldsymbol{p}^2}\right|_{\boldsymbol{p}*} \quad (3.5)$$

In equation 3.5 the variable $p(x,y)$ has been replaced by the vector $\boldsymbol{p} = [p_1(x,y), p_2(x,y), .., p_n(x,y)]$. Following the same procedure as indicated for the case with one variable $p(x,y)(n = 1)$ the difference between $\overline{F}$ and $F(\overline{p})$ can be defined as:

$$\overline{F} - F(\overline{\boldsymbol{p}}) = \frac{1}{2} kV \quad (3.6)$$

[1] **The Mean Value Theorem:** If f is continuous on the closed interval $[a,b]$ and differentiable on the open interval (a,b), then there exists a number c in (a,b) such that $f'(c) = (f(b) - f(a))/(b - a)$

$$\text{where} \quad k = \left.\frac{\partial^2 f}{\partial \boldsymbol{p}^2}\right|_{\boldsymbol{p}_x} \quad \text{and} \quad V = \frac{1}{A}\int_A (\boldsymbol{p}(x,y) - \overline{\boldsymbol{p}})^2 dA$$

Because the term V is dependent on more than one variable not only the variance of all variables within $\boldsymbol{p}(x,y)$ will be needed but also the covariances for the variables in present in $\boldsymbol{p}(x,y)$ has to be calculated. When the input data consist of 2 variables (n=2) the difference can be calculated as:

$$\overline{F} - F(\overline{p}_1, \overline{p}_2) = \frac{1}{2}\left(\begin{array}{r} \frac{1}{A}\int_A (p_1(x,y) - \overline{p}_1)^2 dA \left.\frac{d^2 f}{\partial p_1^2}\right|_p + \\ \frac{1}{A}\int_A (p_2(x,y) - \overline{p}_2)^2 dA \left.\frac{d^2 f}{\partial p_2^2}\right|_p + \\ \frac{1}{A}\int_A (p_1(x,y) - \overline{p}_1)(p_2(x,y) - \overline{p}_2) dA \left.\frac{d^2 f}{\partial p_1 \partial p_2}\right|_p \end{array}\right) \quad (3.7)$$

The last term at the right hand side of equation 3.7 contains the covariance term of p_1 and p_2. The three terms together account for the combined effect of the degree of non-linearity of the model and the heterogeneity of the land surface on the scaling approach. The variance and non-linearity term cannot be written explicitly anymore.

The disadvantage of the Taylor expansion approach is that it only works for a continuous function f and for limited changes in the function values. When using complicated models with a large number of variables it could be a burdensome task to find the derivatives of f. Therefore a different approached developed by Raffy (1994) is presented which considers the problem of aggregation from the perspective of computational geometry.

3.3 Aggregation analysis using convexity approach

The approach described here is based on computational geometry. Some properties of computational geometry will be defined in advance (Preparata and Shamos, 1985):

- Convex: *A domain D is convex, for any two points p and q in D, if the line between p and q is entirely contained in D.* This is illustrated in Figure 3.2 where a convex and non-convex domain are shown. In the non-convex domain the line which connects p and q lies partly outside the domain D.

- Convex Hull: *The convex hull of a set of points S in E is the boundary of the smallest convex domain in E containing S.* This is illustrated in Figure 3.3 where for a number of points the convex hull is drawn. The convex hull can also be conceived as an elastic band that spans around the points, minimizing its length.

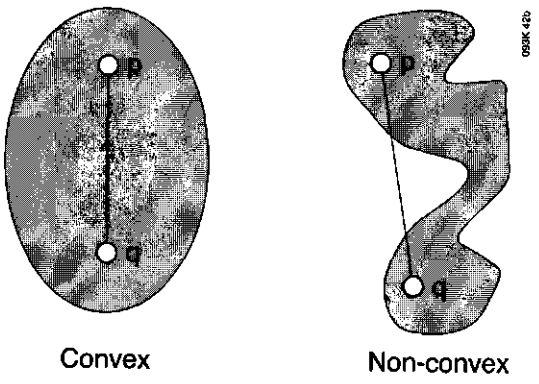

Figure 3.2: Illustration of a convex and non-convex domain.

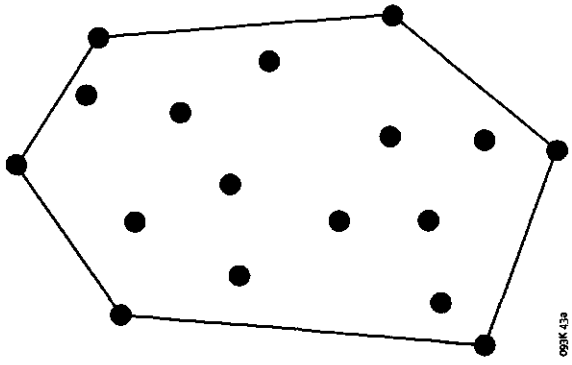

Figure 3.3: The convex hull of a set of points.

The approach described in this paragraph aims at estimating the domain where solutions of a spatially distributed model f may exist. The input $\boldsymbol{p}(x,y)$ of f consists of n spatially distributed variables $[p_1(x,y), p_2(x,y), \ldots p_n(x,y)]$. In Figure 3.4 an observation with a low and high resolution of the same region A is shown.

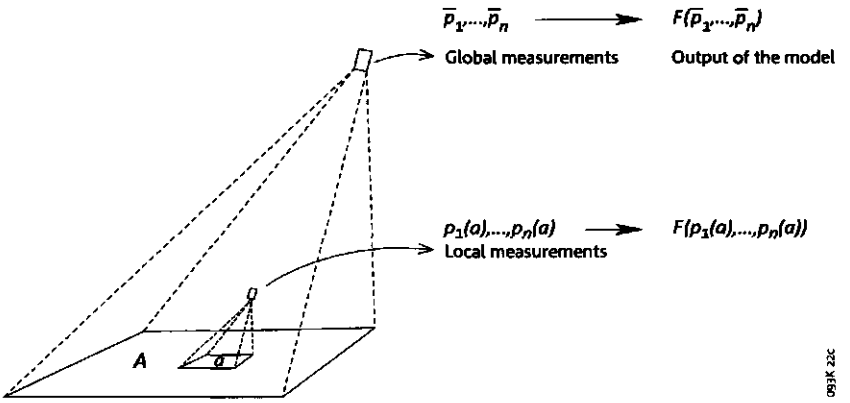

Figure 3.4: A low and high resolution observation of the region A.

At low resolution the whole area A is observed at once, resulting in n values for the input variable $\overline{p}$: $\overline{p_1}, \overline{p_2}, .., \overline{p_n}$. At high resolution only a segment, a, of the domain A is observed. If the area A is covered by $x \times y$ segments equal to the size of a then there will be $x \times y \times n$ values for the independent variable $\boldsymbol{p}(x,y)$. The value of the output calculated by the aggregated model F using the low resolution measurement $\overline{p}$ of A is denoted $F(\overline{p})$. The aggregated output of model f based on the high resolution observations $\boldsymbol{p}(x,y)$ of A is denoted $\overline{F}$. In Figure 3.1 the different ways of obtaining $\overline{F}$ and $F(\overline{\boldsymbol{p}})$ were illustrated.

The approach described here will focus on the possible error by using low resolution data instead of high resolution data: i.e. the difference between $\overline{F}$ and $F(\overline{\boldsymbol{p}})$. This difference will be described without using any a priori assumption on the variable $\boldsymbol{p}(x,y)$. The global measurement $\overline{p}$ of an area A can be the product of any distribution of $\boldsymbol{p}(x,y)$ when the following condition is satisfied, (conservation of energy):

$$\overline{p} = \frac{1}{A} \int_A p(a) da \tag{3.8}$$

This is illustrated in Figure 3.5 where for a global (low resolution) measurement of the area A two possible distributions of local (high resolution)

measurements are given.

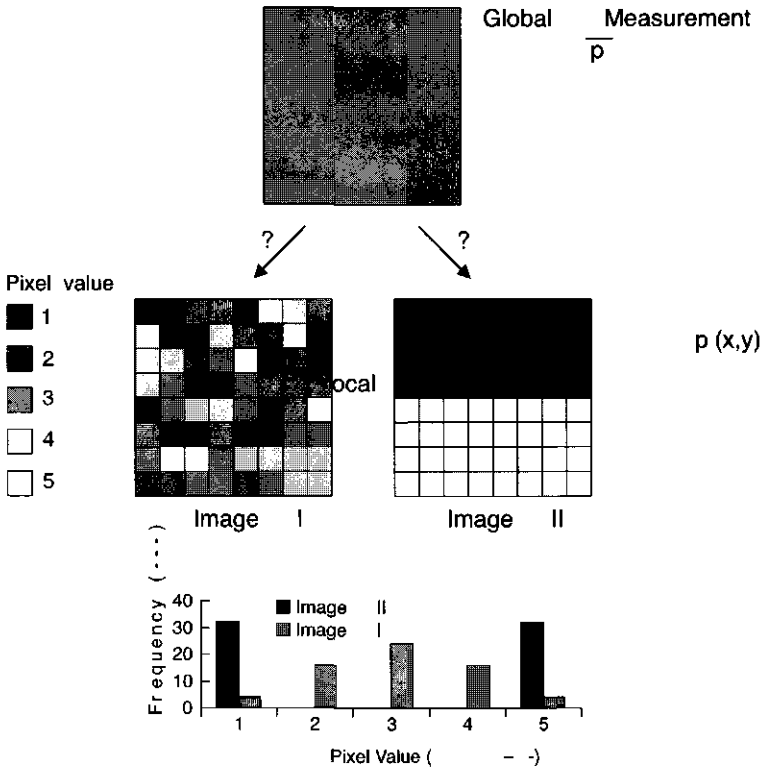

Figure 3.5: Illustration of possible distributions of local measurements of the variable p: $\boldsymbol{p(x,y)}$ (e.g. high resolution remote sensing data) given a global measurement of p: $\overline{p}$ (e.g. low resolution remote sensing data)

Figure 3.5 shows that the mean of both distributed variables $p(x,y)$ is equal to the value of the global measurement $\overline{p}$. However the distribution functions of either set of local measurements $p(x,y)$ are completely different. Applying these two distributions to the (non-linear) distributed model f gives different results for the aggregated output $\overline{F}$. Therefore all possible distribution functions should be taken into account when trying to define the boundaries of the spatial model f. The set containing all possible combinations of distributions of $\boldsymbol{p}(x,y)$ is denoted P. If there are no limits on $\boldsymbol{p}(x,y)$ then P will be a set of infinite extent. However the local measurements $\boldsymbol{p}(x,y)$ are defined within the domain D which is a bounded domain of $\mathbf{R_n}$. This means that the maximum and minimum values within the distributions of $\boldsymbol{p}(x,y)$ are finite. The number of distributions of $\boldsymbol{p}(x,y)$ is therefore finite. In the case of radiometric observations the measurements $\boldsymbol{p}(x,y)$ are radiances. The minimum value of radiances will always be larger than zero. *The domain D is determined by the maximum spatial variability of the local*

measurements $\boldsymbol{p}(x,y)$. Two cases have to be distinguished:

- the domain D is convex and
- the domain D is non-convex.

Figure 3.6 illustrates both cases.

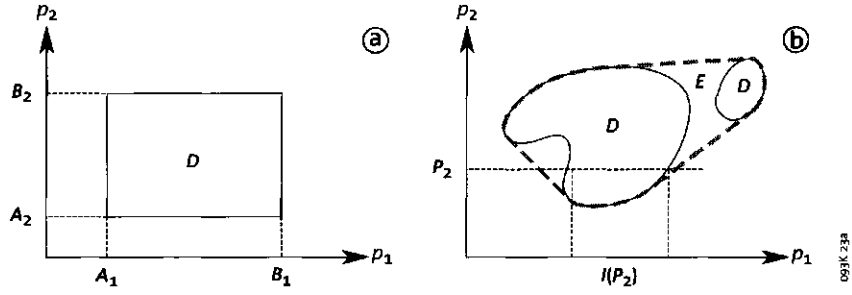

Figure 3.6: The two different classes of domain D for the spatially distributed variable $p(x,y)$ when the number of variables $n = 2$, a) convex domain D and b) a non-convex domain D and its convex hull E.

In Figure 3.6a the domain D is shown for the case of measurements in two bands, p_1 and p_2. The natural bounds of p_1 are A_1 and B_1, respectively the minimum and maximum value. The natural bounds of p_2 are A_2 and B_2. In this example the two bands are not correlated, making the domain D a rectangle, which is a convex set, see Figure 3.2. In Figure 3.6b the domain D is shown for a case where an area A is composed of various landtypes with for each landtype specific boundaries for p_1 and p_2. In this example the two bands are correlated. If $p_2(x,y) = P_2$ then Figure 3.6b shows that p_1 only exist in a limited range: $I(p_2)$. Therefore there are disjoint regions making D a non-convex set.

The high resolution measurements $\boldsymbol{p}(x,y) \in P$ are not distinguishable by a sensor which can only measure the global measurement $\overline{p}$. Using all the distributions of $\boldsymbol{p}(x,y)$ present in P as input for the land surface model f gives the complete range of solutions for $\overline{F}$. *Raffy (1994) showed that the set of all possible in situ values of* $\overline{F}$ *when* $\boldsymbol{p}(x,y) \in P$ *constitute exactly an interval*:

$$\overline{F} \in \left[F_{\vee}(\overline{p}), F^{\wedge}(\overline{p})\right] \tag{3.9}$$

where $F_{\vee}$ and $F^{\wedge}$ are respectively the lower and upper boundary of the convex hull of the graph of F. In other words, the function $F_{\vee}$ is the supremum[2]

[2]The supremum is the least upper bound of a set. The upper bound is any quantity such that no member of a set exceeds it.

of all the convex functions which minor F. The function $F^{\wedge}$ is the infimum[3] of all the concave functions which major F. These functions can be interpreted as 'bounding' models (or 'bounding' functions). *The bounding models can be interpreted as a measure for the non-linearity of function F.*

How D is linked with the bounding models F_V and $F^{\wedge}$ is shown in the following paragraph. This link describes the effects of the spatial variability of the landscape and the non-linearity of the model f.

The derivation of the bounding models F_V and $F^{\wedge}$ is explained for the case of a model f with one variable (n=1). Also here two cases are considered, one where the domain D is convex and another one where D is non-convex. In Figure 3.7 the model f and its bounding models F_V and $F^{\wedge}$ are drawn for the convex and non-convex case.

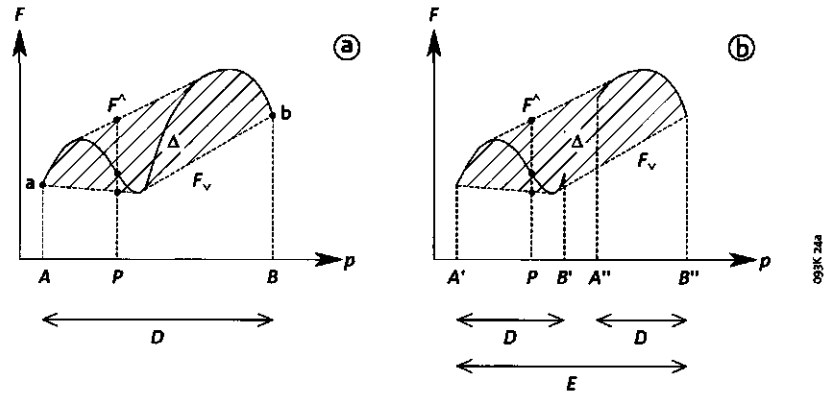

Figure 3.7: The model F and its bounding models F_V and $F^{\wedge}$ for a) a convex domain and b) a non-convex domain.The dashed area denoted by Δ shows all possible solutions for F given the variability of p. F_V and $F^{\wedge}$ are equal for both domains.

Figure 3.7 shows that *The bounding models F_V and $F^{\wedge}$ are respectively the inferior and superior boundaries of the convex hull of the graph of F.* In the convex case (Figure 3.7a) the bounding models can be represented respectively by an elastic which envelops f from the bottom and from the top. Both bounding models begin in the point a and end in b, the distance between these two points is equal to the natural range of the input variable p, which is defined by the convex domain D. All possible solutions are defined within the area denoted by Δ. Figure 3.7a shows the range of possible solutions for $p(x,y) = P$. In the non-convex case (Figure 3.7b) the domain D is split up in two separate domains $[A', B']$ and $[A", B"]$. The convex

[3]The infimum is the greatest lower bound of a set. The lower bound is any quantity such that no member of a set is less than it.

hull of domain D is E. We consider the convex hull which is defined by $[A', B'']$ and follow the same procedure as with the convex case. Note that the function F is discontinuous for Figure 3.7b.

The procedure does not change significantly when the number of variables is larger than 1. The difference between the bounding models $F_\vee$ and $F^\wedge$ is an estimate of the maximum difference between $\overline{F}$ and $F(\overline{\boldsymbol{p}})$, i.e. the maximum error due to aggregation. There might be a distribution of $p(x, y)$ which gives this maximum error.

Whenever the area A is homogeneous that means that the set P containing all possible distribution functions of $\boldsymbol{p(x,y)}$ is equal to the Dirac δ-distribution. All the n*x*y pixels of $\boldsymbol{p}(x,y)$ have the same value which is equal to $\overline{\boldsymbol{p}}$. Therefore the domain D can be defined by a single point, which leads to the result that the difference between $\overline{F}$ and $F(\overline{\boldsymbol{p}})$ is zero. In the case of a linear model F, the bounding models $F_\vee$ and $F^\wedge$ will be equal. This will also lead to the result that the difference between $\overline{F}$ and $F(\overline{\boldsymbol{p}})$ is zero.

Chapter 4

Wavelet analysis

This paragraph will discuss the wavelet transform, although no complete introduction to the theory of wavelets will be given. For an elaborate discussion on wavelets the books of Chui (1992), Daubechies (1992), and Mallat (1998) are recommended. For a review on the use of wavelets in geophysics the reader is referred to Kumar and Foufoula-Georgiou (1997) and Foufoula-Georgiou and Kumar (1994).

The wavelet transform is a relatively new mathematical technique. Within the last decade the application of the wavelet transform increased exponentially in many scientific and engineering fields. In this thesis the wavelet transform will be applied to estimate length scales of land surface characteristics using remotely sensed data. Only the properties of the wavelet transform relevant to the detection of length scales will be discussed in this chapter.

The general idea behind the wavelet transform is to use a localized function in time or space, the wavelet, as a tool to explore a data set. Analyzing a data set with a wavelet enables one to study features of the data set locally with a detail matched to their scale, i.e. broad features on a large scale and fine features on a small scale (Kumar and Foufoula-Georgiou, 1997). A wavelet has two important properties, the wavelet can be:

- expanded or compressed to study broad as well as fine features of the data set
- shifted through the data set showing the location of broad and fine features in the data set.

In other words:

> *"by using a wavelet transform one cannot only see the trees but also the forest".*

In order to properly explain the wavelet transform, first another type of transform has to be introduced: the Fourier transform. The Fourier transform has already been heavily used in all kind of applications. A comparison of both transforms will highlight the advantages of the wavelet transform for detecting dominant length scales of land surface properties using remotely sensed data.

4.1 The Fourier transform

The Fourier transform decomposes any continuous function into a sum of an infinite number of sine and cosine terms (Fourier, 1822). In the case of a discrete data set a finite number of sine and cosine terms will fit to the original data set. The Fourier transform of a (continuous) function f, dependent on time or space, leads to a new function $\hat{f}$ that depends on frequency ω or wavenumber κ. Frequency is the inverse of time whereas wavenumber is the inverse of wavelength. The Fourier transform can be used for detecting dominant frequencies in *stationary*[1] signals.

The Fourier transform $\hat{f}$ of a continuous function f is defined as:

$$\hat{f}(\kappa) = \int_{-\infty}^{+\infty} f(x) e^{-i\kappa x} dx \tag{4.1}$$

where κ is wavenumber (m^{-1}) and x distance (m). Note that wavenumber also can be replaced by frequency ω (s^{-1}), x will then be replaced by time t (s). The individual elements in $\hat{f}$ are called Fourier coefficients.

The complex exponential $e^{-i\kappa t}$ can be written as a function of cosines and sines by using Euler's notation:

$$e^{-i\kappa x} = \cos(\kappa x) - i \sin(\kappa x) \tag{4.2}$$

It can now be clearly seen that the original function will be decomposed into an integral series of sines and cosines, each sine and cosine having a different wavenumber. The dominant wavenumbers of a function will have Fourier coefficients with the highest values. Wavenumbers not present in the function will have Fourier coefficients equal or close to zero.

One of the features of the Fourier transform is that it is possible to reconstruct the original function f using the coefficients of the Fourier transform $\hat{f}$. This is known as the *inverse* Fourier transform:

$$f(x) = \frac{1}{2\pi} \int_{-\infty}^{+\infty} \hat{f}(\kappa) e^{i\kappa x} d\kappa \tag{4.3}$$

[1] A signal is defined stationary in this thesis when the mean and variance do not change with location in the signal. (second order stationarity)

Each Fourier coefficient stands for a wavenumber. By setting some Fourier coefficients in $\hat{f}$ to 0 and applying the inverse Fourier transform it is possible to filter certain wavenumbers out of the original data set.

In order to use the Fourier transform for a discrete data set, equations describing the continuous (inverse) Fourier transform should be discretized. The discrete Fourier transform is calculated as:

$$\hat{f}[k] = \sum_{n=0}^{N-1} f[n] \exp\left(\frac{-i2\pi kn}{N}\right) \tag{4.4}$$

where n is position, k is frequency or wave number and N the number of data points. The inverse discrete Fourier transform is then defined as:

$$f[n] = \frac{1}{N} \sum_{k=0}^{N-1} \hat{f}[k] \exp\left(\frac{i2\pi kn}{N}\right) \tag{4.5}$$

The discrete Fourier transform can now be applied in an operational way. Unfortunately the number of computations increase exponentially with increasing N. In order to still use the discrete Fourier transform in an operational way the Fast Fourier Transform (FFT) has been developed.

4.1.1 The Fast Fourier Transform (FFT)

The Fourier transform found its way into a large number of applications thanks to the development of the Fast Fourier Transform (FFT). Cooley and Tukey (1965) developed the FFT using ideas Carl Friedrich Gauss postulated around 1805. The FFT reduces the number of calculations from N^2 computations to $N \log N$ computations for a Fourier transformation of a data set with N values. Especially for large data sets the FFT needs considerably less calculations to perform a Fourier transform. Along with the early development of computers the FFT can now be used in an operational way. It has been used to solve problems in many scientific and engineering fields, most notably signal and data processing.

A major disadvantage of the Fourier transform is that it works with global functions, namely sines and cosines with different wavenumbers. Therefore the Fourier transform is not very suitable to detect (abrupt) changes in a *non-stationary* data set. The Fourier transform translates a data set expressed in units of time or space to frequency or wavenumber units or vice versa. It is therefore not possible to describe a data set in terms of time or space units **and** frequency or wavenumber units using a Fourier transform. As a consequence the Fourier transform is not a suitable tool to show **where** changes in a data set take place and simultaneously to measure how large those changes are. A first solution developed to solve this problem was the windowed Fourier transform.

4.1.2 The windowed Fourier transform

The windowed Fourier transform has been introduced by Gabor (1946) to measure localized frequency components of sounds. The main idea behind it is to divide a data set into parts of equal size. For each of those parts of the data set a Fourier transform is applied. This will provide local information instead of global information. The data set is not being examined as a whole but part by part. Therefore non-stationary signals which may have locally stationary parts will be better described using a windowed Fourier transform rather than by using a Fourier transform.

The main disadvantage of the windowed Fourier transform is that a choice has to be made between either detail in frequency or detail in time and space. If the windowed Fourier transform is applied to small parts sudden changes can be located, but low frequency components are not discovered. Working with large windows low frequencies are better detected, but time/space localization is worse.

4.2 The continuous wavelet transform

The wavelet transform is better suited to localize both sudden changes in a data set as well as determining the broad features. The wavelet transform is a local function whose size can be adjusted **and** be shifted within a data set. High frequency components can be detected and localized by moving a small wavelet over a data set, whereas low frequency components can be detected by using a larger wavelet with a similar shape as the small one.

The standard wavelet is a function ψ with a zero average. The function is centered in the neighborhood of 0. The standard wavelet is better known as the "mother" wavelet. A whole family of wavelets can be generated from the "mother" wavelet using the scale factor s and translation factor u:

$$\psi_{u,s}(x) = \frac{1}{\sqrt{s}}\psi\left(\frac{x-u}{s}\right) \tag{4.6}$$

The scale factor s expands or contracts the "mother" wavelet, whereas the translation factor u shifts the wavelet in a certain direction. If $s > 1$ the wavelet will be expanded, and if $s < 1$ the wavelet will be contracted. The translation factor u will shift the wavelet center from 0 to $0 + u$. Instead of distance x the wavelet can also be a function of time t.

The function $\psi(x)$ has to fulfill two conditions before it can be called a wavelet. The wavelet has a norm equal to 1 (i.e. $[\int |\psi(x)|^2\, dt = 1$) with:

1. compact support, or sufficiently fast decay, to obtain localization in space and

2. zero mean, as stated before, although higher order moments may also be zero.

The first property ensures that $\psi(t)$ is not a sustaining wave, the second that it is has a wiggle. The requirement of the zero mean is called the admissibility condition of the wavelet. The normalizing constant $1/\sqrt{s}$ is chosen such that $\psi(t)$ has the same norm for all scales s (Kumar and Foufoula-Georgiou, 1997).

Two popular examples of continuous wavelet transforms are the Mexican Hat wavelet and the Morlet wavelet. The Mexican hat wavelet is the second derivative of the Gaussian function:

$$\psi(x) = \frac{2}{\sqrt{3}}\pi^{-1/4}(x^2 - 1)e^{-x^2/2} \tag{4.7}$$

The Morlet wavelet is a complex wavelet, where the real part gives information about the amplitude and the imaginary part gives information about the phase:

$$\psi(x) = \pi^{-1/4}e^{-i\omega_0 x}e^{-x^2/2} \qquad \omega_0 \geqslant 5 \tag{4.8}$$

Figure 4.1a gives an example of the Mexican Hat wavelet with different scaling and translation factors. Figure 4.1b gives for the same scaling and translation factors the real part of the Morlet wavelet. The Morlet wavelet has better localization properties, because of the faster decay of the wave, which makes it a more compact wavelet.

The wavelet transform $Wf(u,s)$ of a continuous function $f(x)$ is defined as:

$$Wf(u,s) = \int_{-\infty}^{+\infty} f(x)\frac{1}{\sqrt{s}}\psi^*\left(\frac{x-u}{s}\right)dx \tag{4.9}$$

where ψ^* is the complex conjugate[2] of ψ. The wavelet transform measures the variation of f in the neighborhood of u, on a scale proportional to s. The wavelet transform provides a flexible time-scale (or space-scale) window that tightens when focusing on small-scale features and widens on large-scale features. In other words, the wavelet is zooming in and out. The wavelet transform is sometimes referred to as a mathematical microscope, where s equals the magnification factor.

The *inverse* wavelet transform is given by:

$$f(x) = \frac{1}{C_\psi}\int_0^{+\infty}\int_{-\infty}^{+\infty} s^{-2}Wf(u,s)\psi_{u,s}(x)duds \tag{4.10}$$

where C_ψ is a constant depending on the choice of the wavelet. The inverse wavelet transform can be used to reconstruct the original data set. Analogous to the Fourier transform, certain wavelet coefficients can be set to 0 to filter out certain frequencies/wavenumbers **at** particular locations. Note the difference with the Fourier transform, where frequencies/wavenumbers can

[2]Complex conjugate: the imaginary part of a complex number is negated, such that $a + ib$ becomes $a - ib$

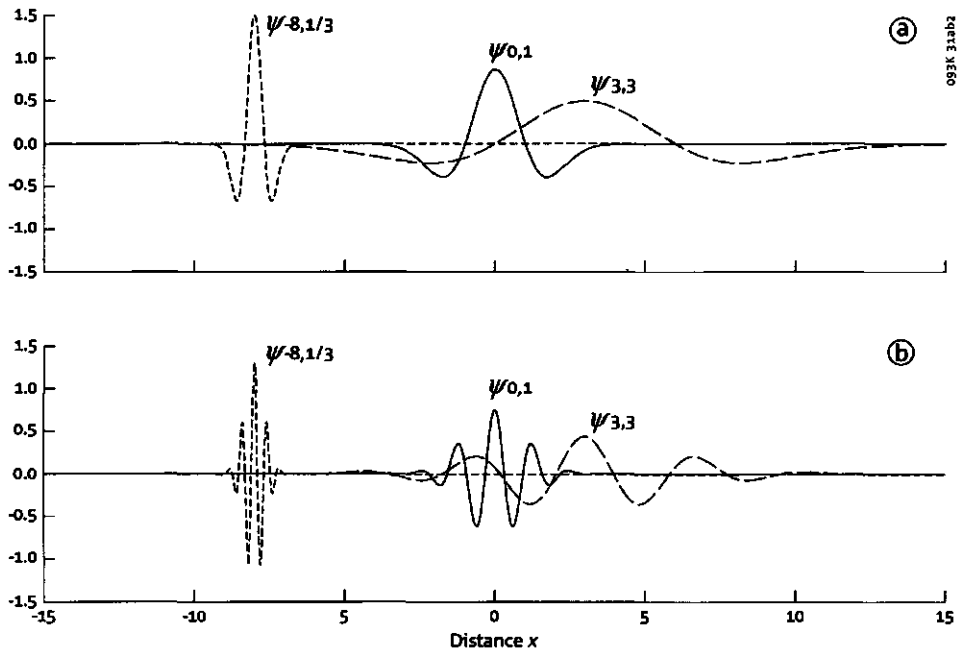

Figure 4.1: a) The Mexican hat wavelet for various scale parameters s and translation parameters u as a function of distance x. If $s < 1$ the wavelet is contracted, if $s > 1$ the wavelet is expanded. If $u < 0$ the wavelet is shifted to the left, if $u > 0$ the wavelet is shifted to the right. b) The real part of the Morlet wavelet with the same scale and translation parameters as used in a) (After Herrmann (1997)).

only be filtered out for the whole data set. By choosing the wavelet coefficients with the largest value and ignoring those with values close or equal to zero, one still could obtain a good approximation of the original data set using limited information.

Like the windowed Fourier transform the continuous wavelet transform is a redundant representation of a data set. Obtaining relevant information from a redundant representation is often a difficult task.

4.3 The discrete wavelet transform

The discrete wavelet transform is a discretization of the continuous wavelet transform. With the discrete wavelet transform the information present in a data set will be reproduced either in a redundant or non-redundant fashion depending on the wavelet and discretization scheme applied. A discretization scheme known as the fast wavelet transform (FWT) will be discussed. The FWT is based on an orthogonal discrete wavelet transform. The FWT represents the data set in a non-redundant fashion. It forms the basis of the multi scale analysis, which will be explained in Paragraph 4.5.

Let $\psi[n]$ be a wavelet consisting of K elements, defined on a discrete data set with N values. For $1 \leq a_j \leq N/K$, a discrete wavelet scaled by a_j is defined by:

$$\psi_j[n] = \frac{1}{\sqrt{a^j}} \psi\left(\frac{n}{a^j}\right) \tag{4.11}$$

where j is the scale parameter j being an integer ≥ 0, a is dilation step, and n is position. The resulting discrete wavelet has $K \times a^j$ non-zero values on $[0, N]$ and is extended into an N periodic signal. If $a = 2$ it is called a dyadic representation.

The discrete wavelet transform is defined as:

$$Wf[n, a^j] = \sum_{m=0}^{N-1} f[m] \psi_j^*[m - n] \tag{4.12}$$

4.3.1 The orthogonal wavelet transform

In this thesis the only discrete wavelet transform which will be considered is the orthogonal wavelet transform. The orthogonal wavelet transform is a special case of the discrete wavelet transform. They are difficult to construct, but give a representation without redundancy and lend themselves to fast algorithms (Burke-Hubbard, 1996). The orthogonal wavelet transform also uses a dyadic representation (i.e. $a = 2$).

The orthogonal wavelet transform uses two basis functions: the discrete wavelet $\psi[n]$ and the scaling function $\phi[n]$. These two functions are orthogonal, i.e. their product equals zero. The wavelet $\psi[n]$ and its corresponding scaling function $\phi[n]$ are not explicit functions. The scaling function is

formed using the scaling function coefficients h together with the following recursive function, also called the dilation equation:

$$\phi[n] = \sum_{k=0}^{K-1} h_k \phi[2n-k] \tag{4.13}$$

where h is the scaling function filter containing K scaling function coefficients. The index k starts at 0. The dilation equation can be used to construct the scaling function.

Once the scaling function is known the wavelet can be defined using the following two relationships:

$$\psi[n] = \sum_{k=0}^{K-1} g_k \phi[2n-k] \tag{4.14}$$

$$\text{with} \qquad g_k = (-1)^k h(1-k)$$

where g is the wavelet filter. The wavelet filter follows directly from the scaling function filter h.

The simplest example of an orthogonal discrete wavelet is the Haar wavelet, being defined as (Haar, 1910):

$$\psi(x) = \begin{cases} 1 & \text{if} \quad 0 \leqslant x < \frac{1}{2} \\ -1 & \text{if} \quad \frac{1}{2} \leqslant x < 1 \\ 0 & \text{otherwise} \end{cases} \tag{4.15}$$

Another popular form of the orthogonal discrete wavelet is the family of Daubechies wavelets (Daubechies, 1988). Daubechies developed wavelets that are both compact and orthogonal. The simplest Daubechies wavelet is characterized by 4 scaling function filter coefficients:

$$\begin{aligned} h_0 &= (1+\sqrt{3})/4\sqrt{2} \\ h_1 &= (3+\sqrt{3})/4\sqrt{2} \\ h_2 &= (3-\sqrt{3})/4\sqrt{2} \\ h_3 &= (1-\sqrt{3})/4\sqrt{2} \end{aligned} \tag{4.16}$$

In Figure 4.2 the Haar and Daubechies-4 wavelets and scaling functions are shown. The Haar wavelet is very compact but not very smooth. The Daubechies-4 wavelet is a fairly smooth function with reasonable compact support.

The orthogonal wavelet transform can be used to decompose a function into a wavelet series. All discrete functions $f[n]$ can be approximated by a linear combination of the wavelet $\psi_j[n]$ and the scaling function $\phi_L[n]$ at scale level $j = L$:

$$f[n] = \sum_{k=0}^{2^{-L}N-1} a_L[k]\phi_L[n] + \sum_{j=1}^{L} \sum_{k=0}^{2^{-j}N-1} d_j[k]\psi_j[n] \tag{4.17}$$

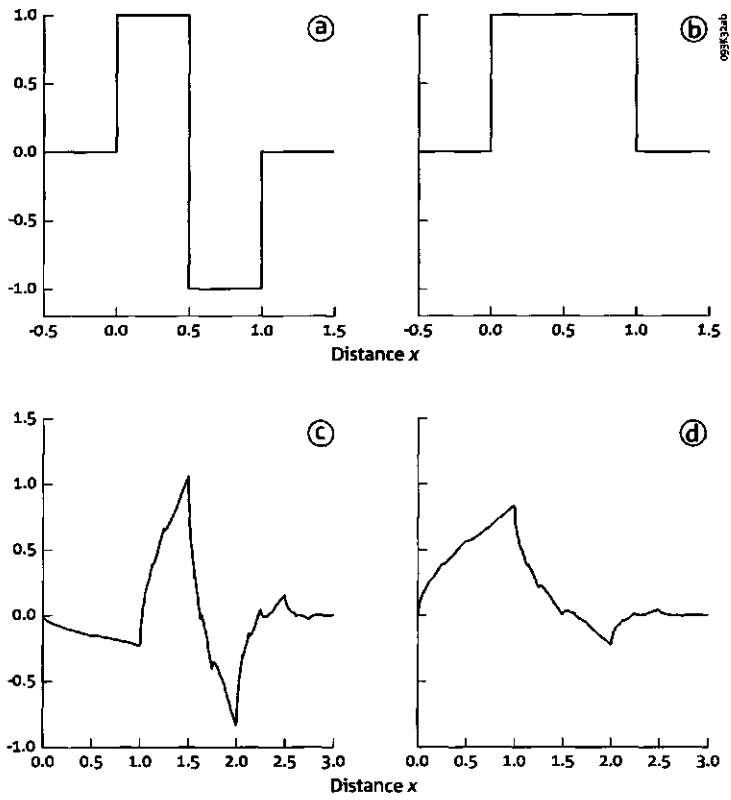

Figure 4.2: **a**) The Haar wavelet, **b**) The Haar scaling function, **c**)The Daubechies-4 wavelet, **d**) The Daubechies-4 scaling function.

where $L = {}^2\log(N)$ and a_L is the scaling function coefficient at scale level $j = L$. The wavelet coefficient $d_j[k]$ measures the contribution of the wavelet ψ_j of scale 2^j at location $k2^j$ to the function f. The question remains how to decompose a signal into its wavelet coefficients d_j. Mallat (1989) came up with an algorithm which decomposes a data set with N elements into N wavelet coefficients: the fast wavelet transform (FWT).

4.4 The fast wavelet transform

The fast wavelet transform is an algorithm where a data set is decomposed into wavelet coefficients using orthogonal discrete wavelets. The orthogonal discrete wavelet $\psi[n]$ can be seen as a high-pass filter consisting of the wavelet filter coefficients g, whereas the corresponding scaling function $\phi[n]$ can be seen as a low-pass filter with scaling function coefficients h. A high-pass filter emphasizes the differences within a data set in contrast to a low-pass filter which evens out the data set. In signal processing the combination of a high-pass and a low-pass filter is known as a quadrature mirror filter. In this paragraph the fast wavelet transform will be described formally.

Let $\overline{x}[n] = x[-n]$ and (Mallat, 1998):

$$\check{x}[n] = \begin{cases} x[p] & \text{if} \quad n = 2p \\ 0 & \text{if} \quad n = 2p+1 \end{cases} \tag{4.18}$$

This is similar to taking every 2^{nd} element in a data set. The wavelet and scaling function coefficients can be recovered as:

$$a_{j+1}[p] = \sum_{n=-\infty}^{+\infty} h[n-2p]a_j[n] = a_j \otimes \bar{h}[2p] \tag{4.19}$$

$$d_{j+1}[p] = \sum_{n=-\infty}^{+\infty} g[n-2p]a_j[n] = a_j \otimes \bar{g}[2p] \tag{4.20}$$

The sign $\otimes$ means that a (circular) convolution is performed. Assuming a periodic data set a circular convolution is defined as:

$$f \otimes h[n] = \sum_{p=0}^{N-1} f\,[n-p]\,h\,[p] \tag{4.21}$$

The original function can be reconstructed using the wavelet and scaling functions:

$$\begin{aligned} a_j[p] &= \sum_{n=-\infty}^{+\infty} h[p-2n]a_{j+1}[n] + \sum_{n=-\infty}^{+\infty} g[p-2n]d_{j+1}[n] \\ &= \check{a}_{j+1} \otimes h[n] + \check{d}_{j+1} \otimes g[n] \end{aligned} \tag{4.22}$$

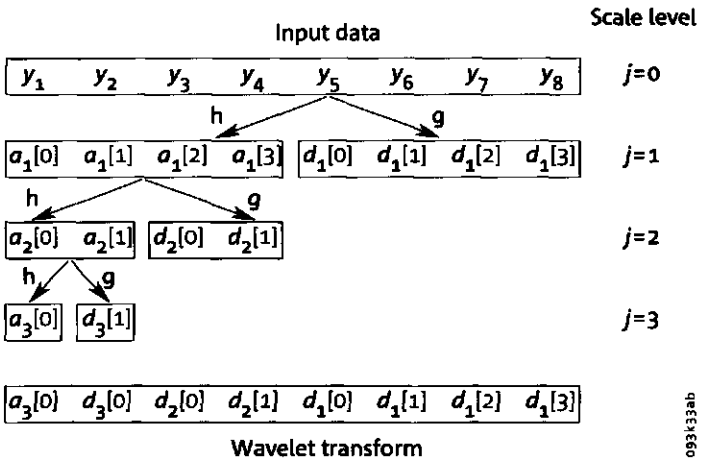

Figure 4.3: The fast wavelet transform (Equations: 4.19 and 4.20) applied to a dataset of 8 observations

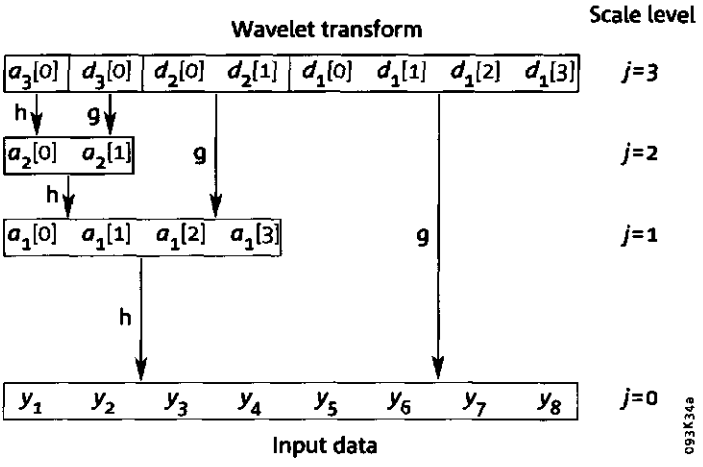

Figure 4.4: The *inverse* fast wavelet transform (Equation 4.22) applied to a wavelet transformed dataset of 8 observations

Figure 4.3 and 4.4 show in a graphical way how the forward and inverse fast wavelet transform work.

The forward wavelet transform decomposes the original data set of N elements (N should be a power of 2) into $\frac{1}{2}N$ **wavelet** coefficients d_1 and $\frac{1}{2}N$ **scaling function** coefficients a_1 using the filters g and h respectively. The filters are convoluted with the original data set and every second element of the resulting product is taken $[n = 0, 2, 4, \ldots, N-2]$. The next step in the algorithm is to decompose the scaling function coefficients of level a_1 into $\frac{1}{4}N$ wavelet coefficients d_2 and $\frac{1}{4}N$ scaling function coefficients a_2 using the filters h and g again. At each subsequent step the remaining scaling function coefficients will be divided into wavelet and scaling function coefficients using the above mentioned procedure.

The fast wavelet transform is the basis for the multi scale analysis of a data set (Mallat, 1989). The inverse fast wavelet transform processes the result of the forward wavelet transform, where the detail coefficients are convoluted with the wavelet filter g, and the smooth coefficients are convoluted with the scaling function filter h (see Figure 4.4).

4.4.1 Fast wavelet transform for images

For the analysis of remote sensing data the fast wavelet transform should be performed in a 2-D fashion. One option is to use the fast wavelet transform in three different directions: vertical, horizontal and diagonal. This procedure is also referred to as the *nonstandard decomposition* (Stollnitz et al., 1995). First all the rows in the image are decomposed into wavelet coefficients and scaling function coefficients using the FWT as described in the previous section. Subsequently the FWT is applied to the columns of the resulting image. This results in an image with four different sections: a section with scaling function coefficients, a section with horizontal wavelet coefficients, a section with vertical wavelet coefficients and a section with diagonal wavelet coefficients. The next step is to apply the same procedure to the section with the scaling function coefficients until the whole image is decomposed into horizontal, vertical and diagonal wavelet filter coefficients. The approach is illustrated in Figure 4.5.

The sample image is a surface albedo image of the Barrax area, Spain, derived from TMS-NS001 airborne imagery, acquired at June 29, 1991. The resolution of the data is 18.5 m. The circles in the image are pivot irrigation systems.

4.5 Multi scale analysis

The fast wavelet transform can be used to decompose a data set into details, smooths and roughs. Such an analysis is called a multi scale analysis (Mallat, 1989). The details show how much variability is present at each scale

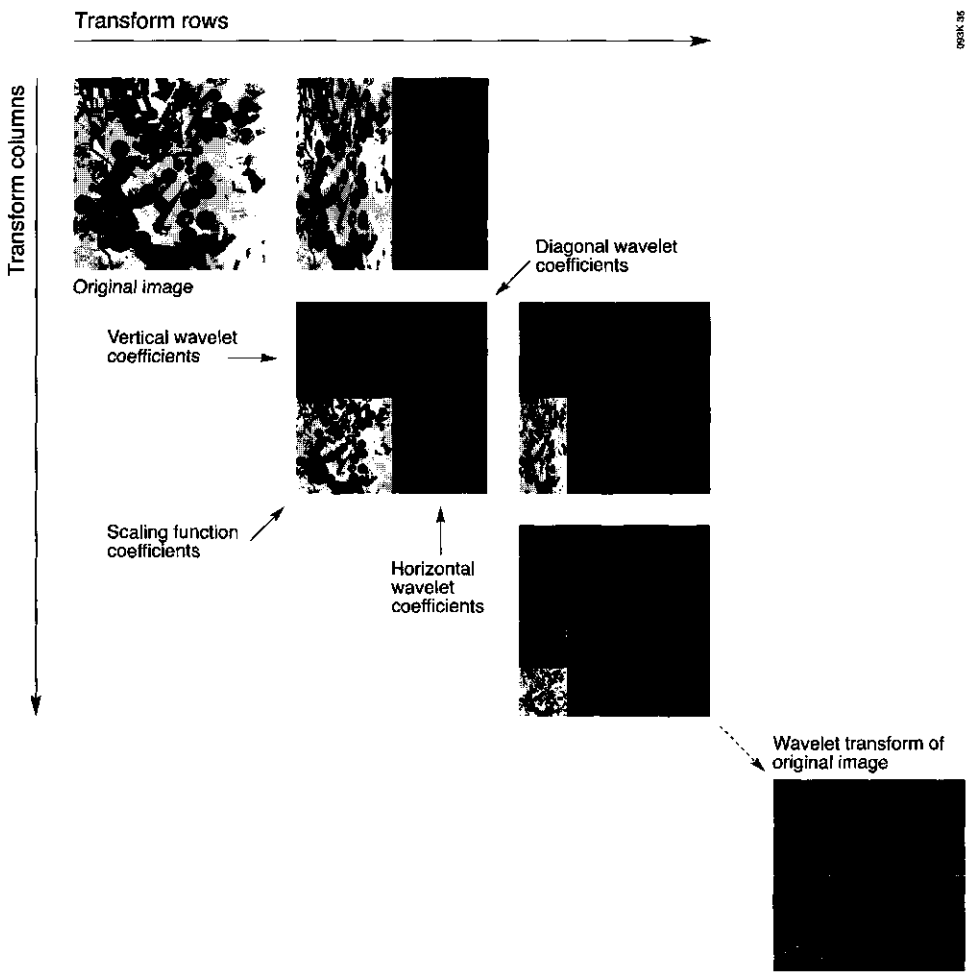

Figure 4.5: Nonstandard decomposition of a sample image, using the fast wavelet transform (After Stollnitz et al. (1995)). The sample image is the surface albedo r_0 image of Barrax, Spain, derived from TMS-NS001 imagery, acquired at June, 29, 1991

level j. Details of scale level j can be found by taking an inverse fast wavelet transform using only the wavelet coefficients found by the fast wavelet transform at that particular scale level j. The smooths at scale level j can be found taking an inverse fast wavelet transform using only the wavelet coefficients for all scale levels equal to and larger than scale level j. The roughs at scale level j can be found taking an inverse fast wavelet transform using only the wavelet coefficients for all scale levels less than scale level j. If the Haar wavelet is applied, the smooths correspond with linearly averaged versions of the data set. This makes the Haar wavelet a good analysis tool for aggregation studies.

Figure 4.6 shows an example of a multi scale analysis of a sample data set using the Haar wavelet. The sample is taken from a surface albedo image from Barrax, Spain. The albedo is derived from data taken by the TMS-NS001 acquired at 29 June 1991. The geometrical resolution of the data is 18.5 m. At scale level $j = 0$ (resolution = 18.5 m) the smooths depict the original data. At scale level $j = 1$ (resolution = 37 m) the smooths show the data at a resolution twice as coarse. The details at scale level $j = 1$ show the amount of detail lost in the process of smoothing. The roughs and details are identical for scale level $j = 1$. At scale level $j = 2$ the details show the difference between the smooths of scale level $j = 1$ and $j = 2$, whereas the roughs show the differences between the smooths at scale level $j = 0$ and the present scale level (level $j = 2$).

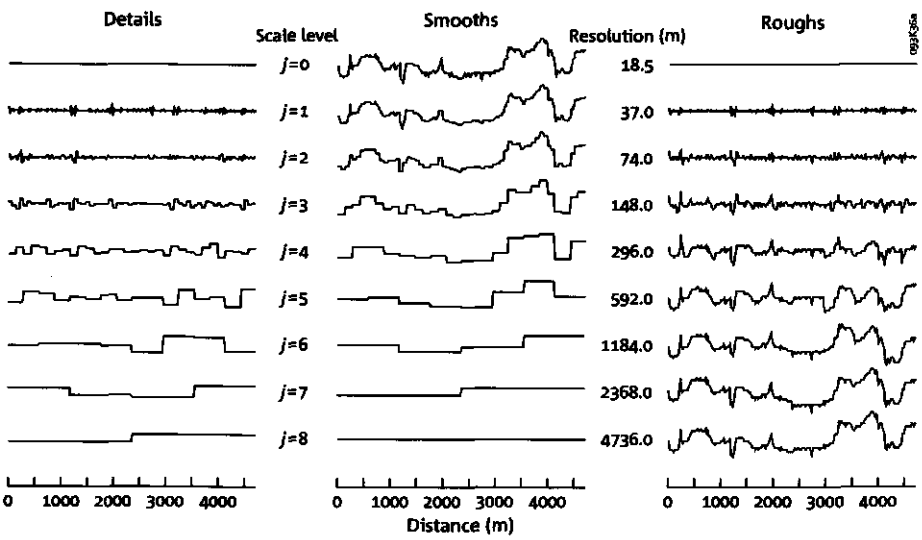

Figure 4.6: A multi scale analysis by means of the Fast Wavelet Transform using the Haar wavelet of a sample of the surface albedo r_0 image, Barrax, June 29, 1991 of Figure 4.5 (original image) using the Haar wavelet.

The roughs at a given scale level equal the summation of the details at scale levels less than that given scale level. The roughs show how much information or detail is lost in the process of smoothing. At the highest scale levels all the smooths equal the mean value of the input data set, whereas the roughs at the highest scale level equal the input data set itself.

The multi scale analysis can also be applied to images. An image can be decomposed into details, roughs and smooths using the fast wavelet transform. Figure 4.7 gives an example of a multi scale analysis using the previously introduced surface albedo r_0 image of Barrax (See Figure 4.5). Only the results for a few scale levels are given.

Figure 4.7 also shows that an image can be subdivided into roughs, smooths and details. In this example the Haar wavelet has been used. The smooths are therefore similar to linearly aggregated versions of the input image. The roughs show how much detail has been lost in the proces of smoothing (i.e. aggregation). Especially at scale level $j = 5$ the roughs are more similar to the input image than the smooths. Much of the information present in the image has been lost in the process of smoothing. However looking at the smooths at scale level $j = 1$ and $j = 3$ we still can detect the most dominant features of the image, in this case the pivot irrigation systems. This shows that the multi scale analysis can be an useful tool for detecting length scales of land surface characteristics.

4.6 Wavelet variance

A quantification of the length scale can be achieved by using the wavelet variance as indicator. The wavelet coefficients are a measure of the intensity of the local variations of the signal, for the scale under consideration. The value of a wavelet coefficient will be large when the dilation of the wavelet is close to the size of a irregular feature in the signal. The value of a coefficient will be negligible when the local signal is regular for that particular scale (Ranchin and Wald, 1993). The variance of the wavelet coefficients, the wavelet variance, is thus a natural tool for investigating the spatial scales of variability in remote sensing data (Percival, 1995). The wavelet variance $\hat{\sigma}^2_{f,j}$ is defined as:

$$\hat{\sigma}^2_{f,j} = \frac{1}{N} \sum_{p=1}^{n_j} d_j[p]^2 \tag{4.23}$$

where $\hat{\sigma}^2_{f,j}$ is the sample wavelet variance of data set f at scale j and $d_j[p]$ is the wavelet coefficient at position p and scale level j. N is the number of elements in the total data set. The number of data points at scale level j is given by $n_j = N/2^j$.

As an example the wavelet variance for the sample data set of Figure 4.6 is given in Figure 4.8

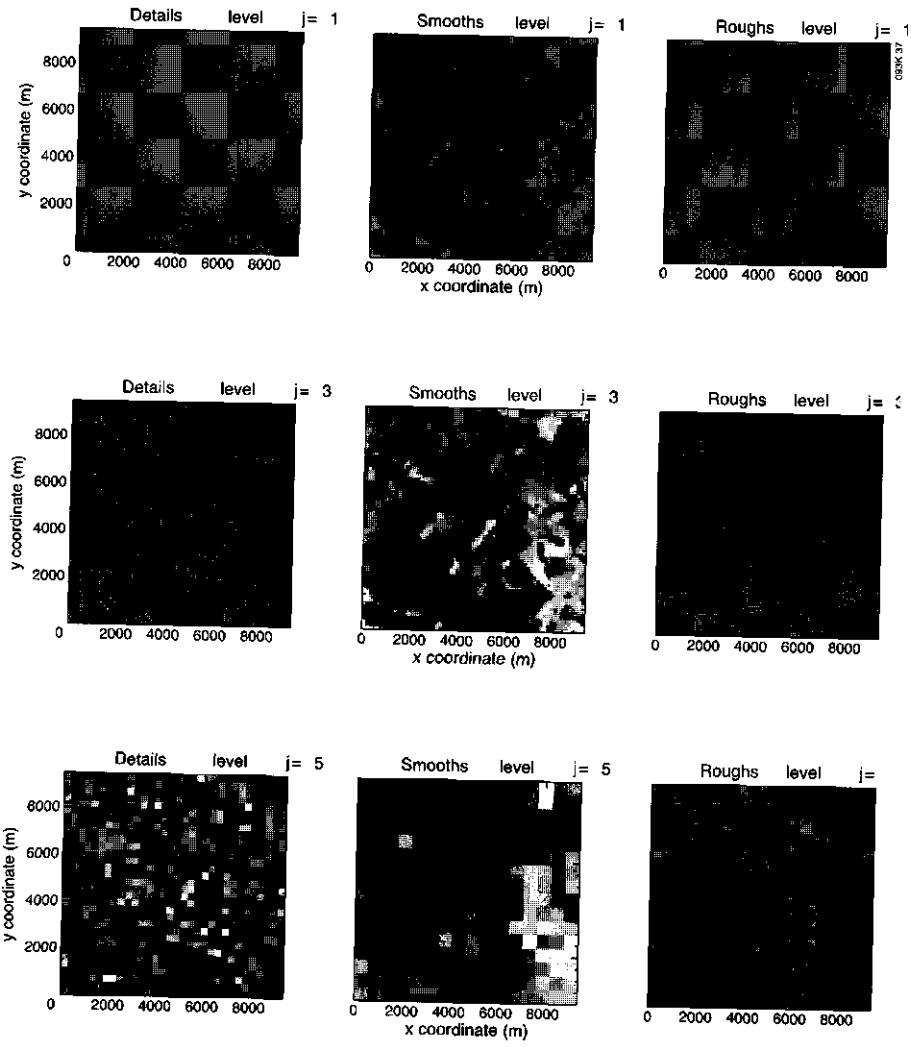

Figure 4.7: Multi scale analysis by means of the Fast Wavelet Transform using the Haar wavelet, of the surface albedo r_0 image, Barrax, June 29, 1991. The roughs, smooths and details are given for scale levels $j = 1, 3, 5$.

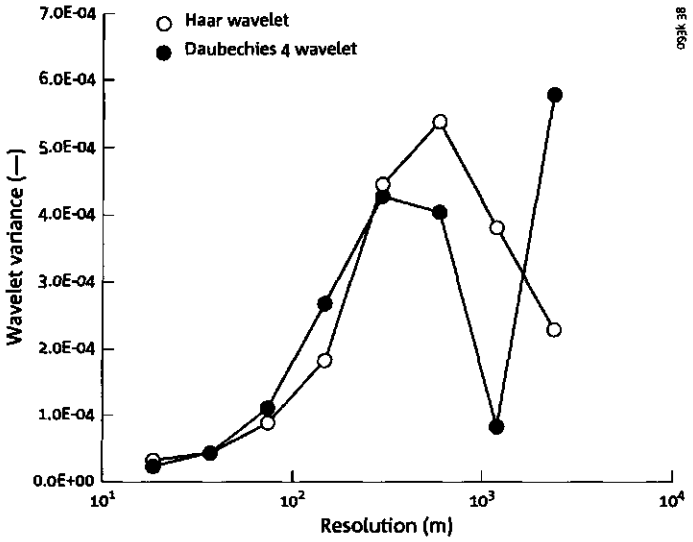

Figure 4.8: Wavelet variance of a sample in the surface albedo r_0 image, Barrax, June 29, 1991, already presented in Figure 4.6. Two wavelets have been used: Haar and Daubechies-4 (note the logarithmic scale of the x-axis).

Figure 4.8 shows that the wavelet variance is low at the smallest resolutions, showing that there is scarce information in the small scale details. The maximum wavelet variance of the Haar wavelet is at 592 m (notice the logarithmic scale of the x-axis). The maximum wavelet variance of the Daubechies wavelet variance is at 2368 m and another peak is visible at 296 m. This graph shows that at approximately 296 and 592 m the most dominant features are present in the sample data set.

Besides the wavelet variance also the wavelet covariance can be calculated. In many applications the analysis is not limited to one data set, but to several. In the framework of this thesis three land surface characteristics are being examined: r_0, T_0 and the $NDVI$. The wavelet covariance indicates the degree of common relationship between two data sets at different spatial scales. The wavelet covariance $\hat{\sigma}^2_{fg,j}$ for two data sets f and g can be calculated as:

$$\hat{\sigma}^2_{fg,j} = \frac{1}{N} \sum_{p=1}^{n_j} d_j^f[p] d_j^g[p] \tag{4.24}$$

where $\hat{\sigma}^2_{fg,j}$ is the sample wavelet covariance of data set f and g at scale j and $d_j^f[p]$ is the wavelet coefficient at position p and scale level j for data set f and $d_j^g[p]$ is the wavelet coefficient at position p and scale level j for data set g.

The wavelet (co)variance can also be calculated for an image. Figure 4.9

gives the wavelet variance of the image of Figure 4.7. Figure 4.9 shows that for both the Daubechies-4 and Haar wavelet the maximum wavelet variance is achieved at the scale of 296 m. Looking at the image in Figure 1.5 the scale of 296 m corresponds with the most dominant feature present in the image: the pivot irrigation systems. If the Barrax area would be sampled at a geometrical resolution lower than 296 m (i.e pixel size $\geq$ 296 m) much of the variability present in the image would not be captured.

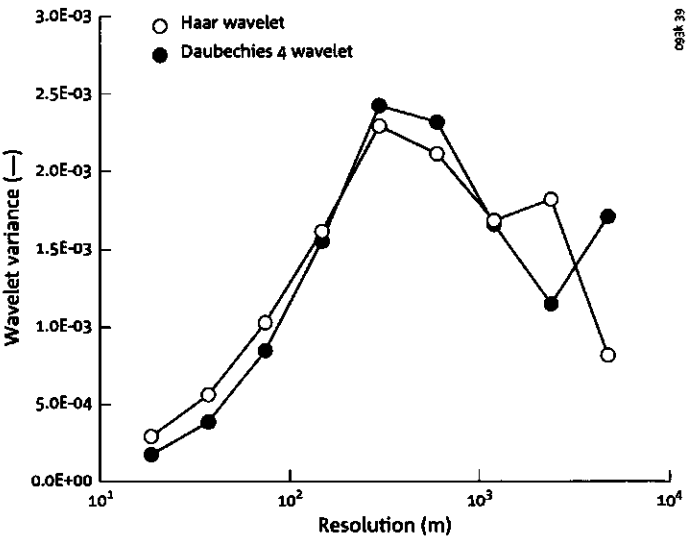

Figure 4.9: Wavelet variance of the surface albedo r_0 image, June 29, 1991 (see Figure 4.7). Two wavelets have been used: Haar and Daubechies-4 (note the logarithmic scale of the x-axis).

In this thesis the wavelet variance will be used as a measure of the length scales of land surface characteristics derived from radiometric observations. The assumption is that the dominant length scales in the landscape will also have a large wavelet variance at that particular scale.

In the following paragraph this hypothesis is tested using test images with predefined length scales.

4.7 Length scale analysis by means of wavelet analysis

In order to test the reliability of the wavelet variance as a measure of the length scale of objects in a remote sensing image a numerical experiment has been set up. In this experiment 1000 images with a size of 256 $\times$ 256

pixels have been simulated using a random generator. The random generator produced normal distributions with unit random variance. Each image could exist of one, two or three dominant length scales with sizes ranging of 1, 2, 4, 8, 16, 32, 64 or 128 pixels. For each image the wavelet variance has been calculated. The wavelet variance gives the variance of the image for each scale level. The wavelet variance would be a good indicator of the length scale if the scale levels with the highest wavelet variance would correspond with the simulated (randomly chosen) length scales.

In this test nine types of orthogonal discrete wavelets have been tested:

- Haar Wavelet (2 coefficients)
- Daubechies Wavelet (4 and 20 coefficients)
- Coifflet Wavelet (6 and 30 coefficients)
- Beylkin Wavelet (18 coefficients)
- Symmlet Wavelet (8 and 20 coefficients)
- Vaidyanathan Wavelet (24 coefficients)

A higher number of coefficients indicates a less compact but more smooth wavelet. In Figure 4.10 the nine type of wavelets and corresponding scaling functions are plotted, except for the Haar wavelet which already has been plotted in Figure 4.2a.

In Table 4.1 the results of the simulation experiments are given. A correct estimation is whenever the dominant length scales present in the image were identified correctly using the maximum wavelet variance hypothesis, regardless of the right order.

From Table 4.1 it is clear that the *Haar wavelet is the best wavelet to use to identify length scales with use of the wavelet variance hypothesis.* Especially when there is only one dominant length scale present in the image the Haar wavelet is almost always correct. The other wavelets perform also quite well at identifying one dominant length scale. Only if there is more than one length scale present in the image the performance of the wavelets, except for the Haar wavelet, dramatically decrease. In this thesis the Haar wavelet will be used for estimating length scales of land surface characteristics using remote sensing imagery.

Another strong argument to choose for the Haar wavelet has to do with the aggregation analysis by means of linearization explained in Paragraph 3.2. Equation 3.7 shows that the difference between $\overline{F}$ and $F(\overline{\boldsymbol{p}})$ is partly explained by the variance(s) (and covariances) of the variable $\boldsymbol{p}(x, y)(n \geq 1)$. *In the case of the Haar wavelet the cumulative variance and covariance are equal to the variance and covariances of* $\boldsymbol{p}$ *in Equation 3.7.* The wavelet variance and covariance should be cumulated up to the scale level of the

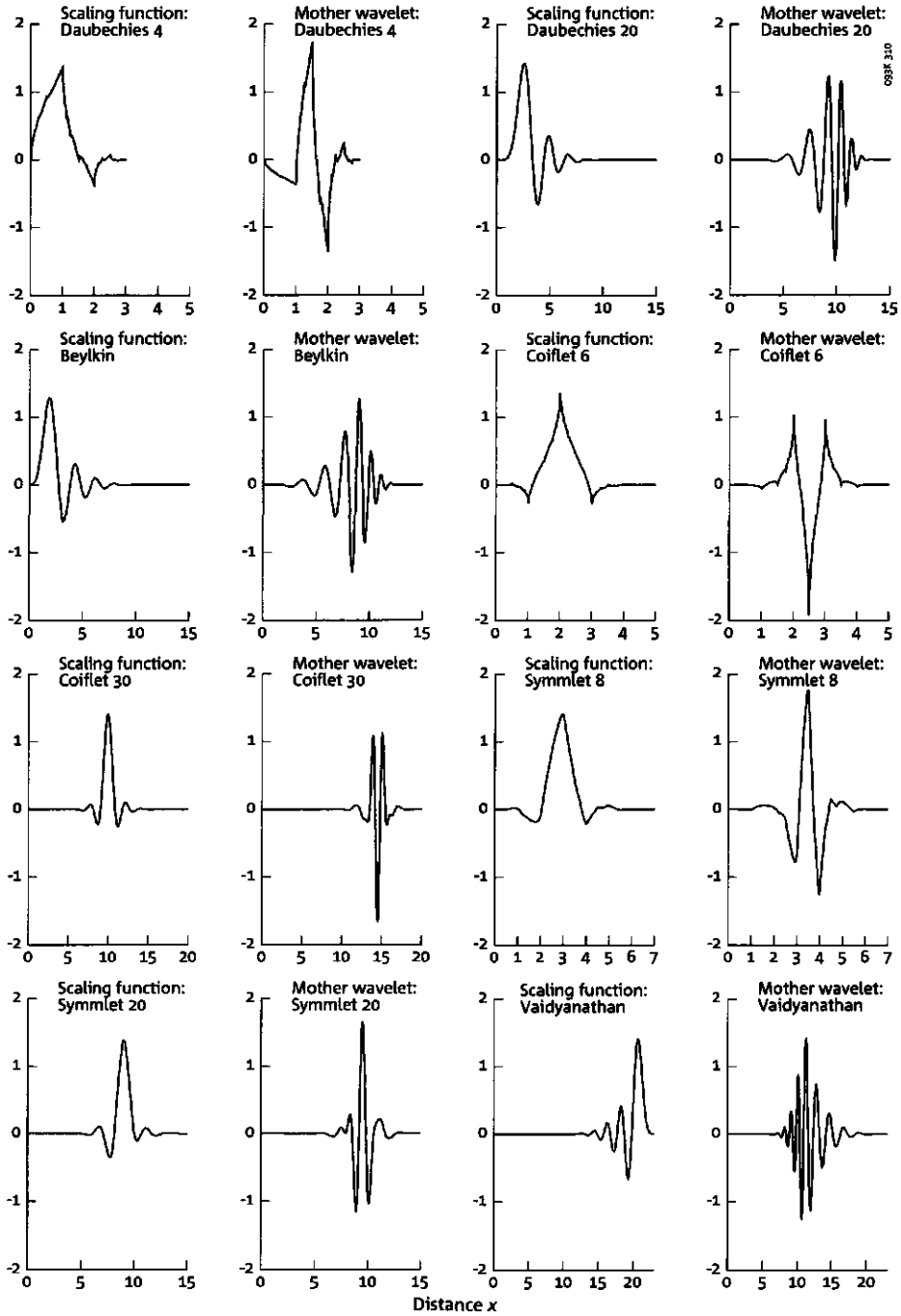

Figure 4.10: The wavelets used in the numerical length scale test of 1000 images of 256*256 pixels. Both the wavelet and scaling function are given. The Haar wavelet is given in Figure 4.2a

Table 4.1: Results of length scale simulation where 9 different wavelets were used to retrieve the length scale of 1000 randomly generated images of 256*256 pixels.

Wavelet	Type of Simulation	All dominant length scales identified (%)	One dominant length scale not identified (%)	None of the dominant length scales identified (%)
Haar	total	**87.70**	0.10	12.20
	1 dominant length scale	99.71	-	0.29
	2 dominant length scales	87.10	0.00	12.90
	3 dominant length scales	75.24	0.00	24.76
Daubechies 4	total	**57.60**	3.00	39.40
	1 dominant length scale	91.28	-	8.72
	2 dominant length scales	47.51	0.00	12.90
	3 dominant length scales	31.75	0.00	68.25
Daubechies 20	total	**63.40**	4.50	32.10
	1 dominant length scale	86.92	-	13.08
	2 dominant length scales	58.94	0.00	41.06
	3 dominant length scales	42.54	0.00	57.46
Coiflet 6	total	**38.40**	16.80	44.80
	1 dominant length scale	60.17	-	39.83
	2 dominant length scales	30.50	0.00	60.41
	3 dominant length scales	23.17	0.00	76.83
Coiflet 30	total	**42.80**	10.10	47.10
	1 dominant length scale	73.84	-	26.16
	2 dominant length scales	32.84	3.23	63.93
	3 dominant length scales	19.68	0.00	80.32
Beylkin	total	**27.70**	17.30	55.00
	1 dominant length scale	55.81	-	44.19
	2 dominant length scales	15.54	6.16	78.30
	3 dominant length scales	10.16	0.00	89.84
Symmlet 8	total	**42.00**	8.80	49.20
	1 dominant length scale	75.29	-	24.71
	2 dominant length scales	28.74	0.88	70.38
	3 dominant length scales	20.00	0.00	80.00
Symmlet 20	total	**36.10**	13.90	50.00
	1 dominant length scale	65.12	-	34.88
	2 dominant length scales	25.81	5.57	68.62
	3 dominant length scales	15.56	0.00	84.44
Vaidyanathan	total	**39.30**	10.80	49.90
	1 dominant length scale	72.09	-	27.91
	2 dominant length scales	25.81	3.23	70.97
	3 dominant length scales	18.10	0.32	81.59

aggregated results. This can be explained by the fact that the smooths at scale level j resulting from the multi scale analysis of a certain data set using the Haar wavelet produces the same result when that data set is resampled to scale level j by means of linear averaging. This makes the Haar wavelet a suitable tool for aggregation analysis.

Chapter 5

Description of the study areas

The field and remote sensing data used in this thesis have been collected at three test sites. The first site is chosen because of the extremes in land use: irrigated and rainfed agriculture: Barrax, Spain. The second site is representative of an arid climate regime: The Jornada experimental range in New Mexico, USA. The third site is representative of a temperate oceanic climate: the Central Part of the Netherlands.

5.1 Barrax

The Barrax site was one of the three experimental sites in the European Field Experiment in a Desertification threatened Area (EFEDA) field campaign (Bolle et al., 1993) held in June 1991. The EFEDA project aimed at describing the energy and water transfer processes between soil, vegetation and the atmosphere in semi-arid conditions. The area is located in the South-East of Spain, between 2° - 3°30' W and 39° - 40° N. The field experiment consisted of a large number of simultaneous patch scale measurements on land surface flux densities and associated hydro-meteorological measurements. Also a large array of airborne remote sensing data has been gathered during the three weeks period of intensive field observations.

5.1.1 Location and climate

The Barrax site is located on the central plateau of Spain, the Meseta, with an altitude between 700 and 800 m. The Barrax site is 28 km north of Albacete. The regional water table is about 20-30 m below the surface. The geographical coordinates of the site are 39 ° 3' N 2° 6' W. The location of the Barrax site is shown in Figure 5.1

According to the revised Köppen climate classification the climate can be classified as a subtropical winter rain climate (Rudloff, 1981). Hot summers and mild winters characterize this climate. The continental character ap-

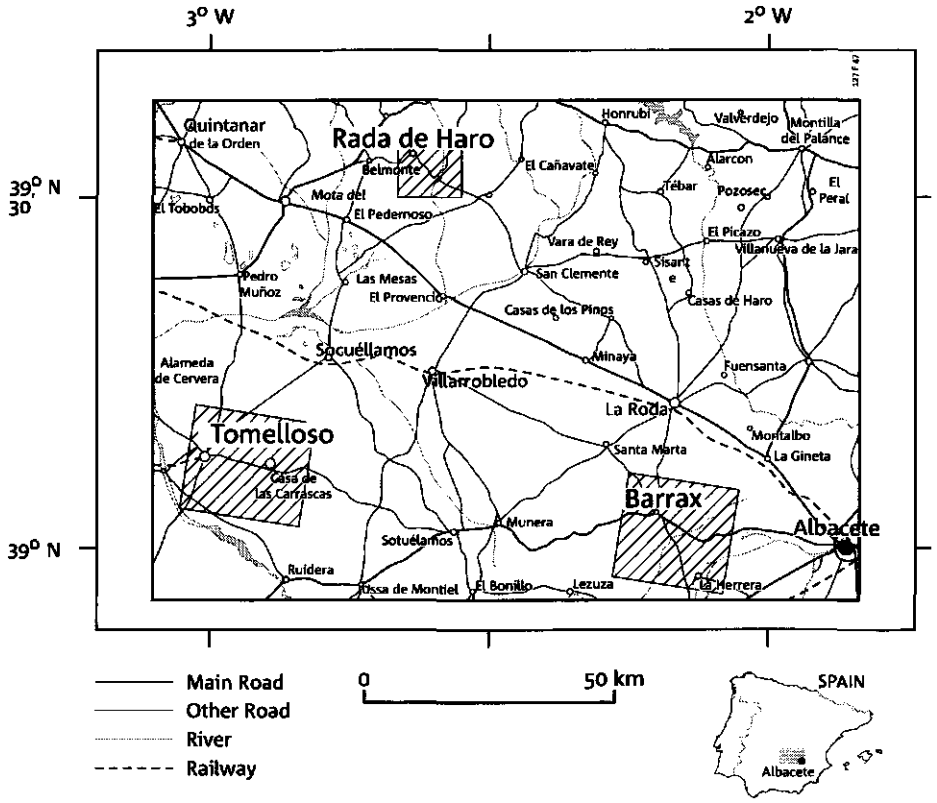

Figure 5.1: Location of Barrax site within the EFEDA gridbox. Also the other two sites, Tomelloso and Rada de Haro are shown.

pears from the sudden changes from cold months to high months. The mean monthly temperature is above 22 °C in the summer and the temperature can even reach values above 40 °C. The average winter temperature is below 6 °C. The daily temperature oscillation is larger in the summer than in the winter. In the summer the temperature oscillation can reach values up to 30 °C.

The mean annual rainfall is little more than 400 mm, making this area to one of the driest in Europe. The summer is dry, with the bulk of the precipitation falling in the spring and autumn. There is a large year-to-year variability. Figure 5.2 shows the mean annual precipitation for the weather station closest to the Barrax site, the Munera rainfall station.

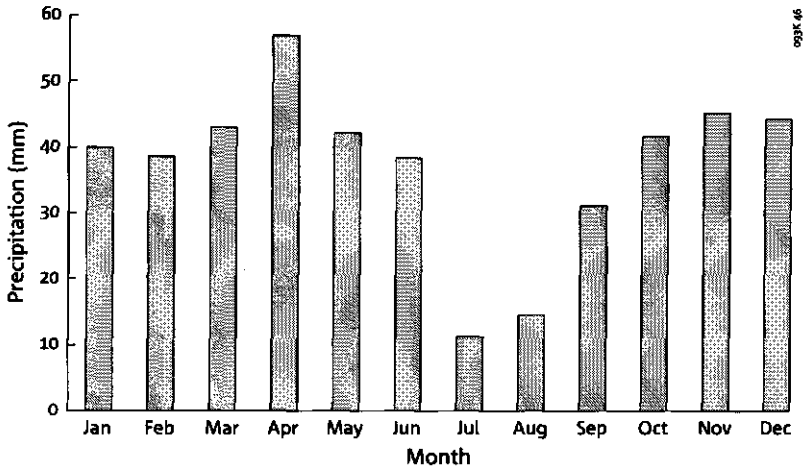

Figure 5.2: Mean annual precipitation for Munera weather station based on the period of 1951 – 1991.

At the beginning of the field experiment some thunderstorms with heavy rain were present in the study area. In the following days there was no rainfall anymore leading to a dry-down period.

The Barrax site is very flat with very poorly developed soils. The regional water table is about 20-30 m below the surface. The main cultivation is approximately 65% dry land (winter cereals, fallow) and 35% irrigated land (corn, barley, sunflower, alfalfa, onions, vegetables). There are two types of irrigation present in the region: surface irrigation and pivot irrigation.

5.1.2 Field data

In the Barrax site the main characteristic is the presence of irrigated fields and non-irrigated fields next to each other. For this purpose micrometeorological measurements have been made on three different surfaces: bare

soil, irrigated maize and fallow land. At these points energy balance fluxes have been measured together with other hydro-meteorological measurements. Also soil moisture measurements have been performed on a daily basis at 24 locations on 9 different fields. In Figure 5.3 measurements of the specific humidity, air temperature, solar radiation and wind speed on 29 June 1991 for the irrigated maize plot are shown.

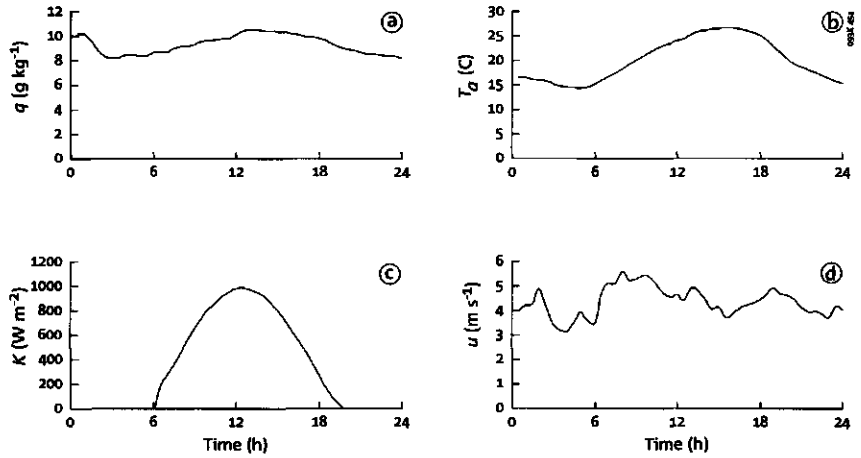

Figure 5.3: Daily course of a) specific humidity q, b) air temperature T_a, c) incoming shortwave radiation $K^{\downarrow}$ and d) wind speed u measured at the irrigated maize site, Barrax, June 29, 1991.

5.1.3 Remote sensing data

During the field campaign several aircrafts equipped with remote sensing devices have flown over the experimental area. The data which shall be used in this thesis comes from the TMS-NS001 scanner aboard the NASA-ER2 aircraft. The TMS measures in the same spectral bands as the Landsat TM satellite, see Table 5.4. The TMS-NS001 data have been recorded at 29 june 1991. The remote sensing data were used to obtain the following land surface characteristics: surface albedo, r_0, surface temperature, T_0 and the Normalized Difference Vegetation Index ($NDVI$). The $NDVI$ is defined as the ratio (NIR-R)/(NIR+R) where NIR is the reflectance in the near infrared and R is the reflectance in the red part of the electromagnetic spectrum. The reflectances for both bands were already derived during the calculation of the surface albedo. The $NDVI$ is an indicator for the amount of biomass. A high $NDVI$ value corresponds with a high amount of biomass, whereas a low $NDVI$ value corresponds with a low amount of biomass. The remote sensing data have been corrected for atmospheric influences.

In Table 5.1 the statistics for the land surface characteristics derived from

Table 5.1: Statistics of the land surface characteristics r_0, T_0 and $NDVI$, derived from airborne TMS-NS001 data for the Barrax area

Land surface characteristic	Minimum	Maximum	Mean	Median	Modus	Standard Deviation
r_0 (-)	0.071	0.439	0.226	0.224	0.196	0.054
T_0 (K)	293.650	318.650	306.174	308.65	308.65	4.424
$NDVI(-)$	0.031	0.773	0.386	0.320	0.284	0.118

the TMS-NS001 imagery are given. Note the large standard deviation for the T_0 and surface albedo compared to the standard deviation of the same land surface characteristics for the Landsat TM image of the Netherlands (see table 5.5). However the area of the Barrax is site is much smaller compared to that of the area covered by the Landsat TM image of the Netherlands, which is more than 50 times larger. This shows the large spatial variability present in the Barrax area. A n image of r_0 is shown i Plate A for the Barrax site.

5.2 Jornada Experimental Range

The Jornada Experimental Range in southern New Mexico, USA, has been a site of long-term ecological research for investigation of processes related to desertification. It has been included in the National Science Foundation (NSF) Long-Term Ecological Reserve (LTER) program as well as in the United Nations (UN) Man And the Biosphere (MAB) program. Already in the beginning of this century the first experimental research started. Since then an enormous amount of data concerning the state of the vegetation and ecosystem dynamics have been collected. In 1995 a campaign named JORNEX (the JORNada EXperiment) started collecting remotely sensed data from ground, airborne and satellite platforms to provide spatial and temporal data on the physical and biological state of the rangeland (Ritchie et al., 1996). In this thesis data collected during the June 1997 campaign will be used.

5.2.1 Location and climate

The Jornada Experimental Range, the largest Agricultural Research Service (ARS) field station (783 km^2), is situated 37 km north of Las Cruces, New Mexico. Most of the Experimental Range is located on the Jornada del Muerto Plain of the Chihuahuan Desert at about 1200 m elevation, bordered by the Rio Grande Valley in the west and the San Andres Mountains in the east, see Figure 5.4. The crest of the San Andres Mountains is about 2440 m and coincides with the eastern boundary of the Experimental Range.

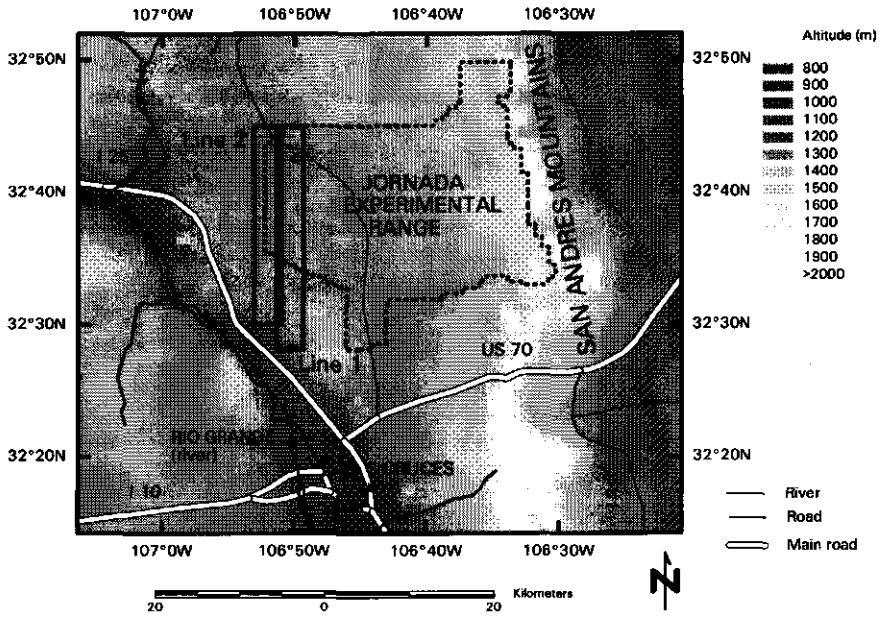

Figure 5.4: Location of the Jornada Experimental Range, Las Cruces NM, USA. Also the flight lines for the Daedalus recordings of June 19, 1997 are indicated.

The climate is characteristic for the northern region of the Chihuahuan desert, the most arid of the North American grasslands. The climate is classified according to the revised Köppen climate classification as a desert climate (Rudloff, 1981). Annual averages for precipitation and temperature are 241 mm and 15 °C, respectively. Approximately 55% of the annual precipitation occurs as localized thunderstorms during July, August and September. Droughts (<75% of average annual precipitation) are common, and have occurred in 18 years between 1915 and 1995. The frost-free period averages 200 days, but the effective growing season, especially for perennial grasses, is limited to the summer months. High temperatures, low humidity, and frequent winds during the summer result in large water losses by evaporation. Potential evaporation rates are approximately 10 times the average precipitation.

The remote sensing data used in this thesis were collected at June 19, 1997. For the year 1997 climatic data concerning rainfall and air temperature were collected at the New Mexico State University (NMSU) Jornada Range weather station. Data were retrieved from the World Wide Web site of the NMSU (http://weather.nmsu.edu).

Figure 5.5 shows the annual trend of rainfall and air temperature for the Jornada Range weather station in 1997. The year 1997 was wetter than normal, 267 mm in 1997 vs 241 mm on average. The year 1997 was also warmer than usual, 17.9 °C in 1997 vs 15 °C on average.

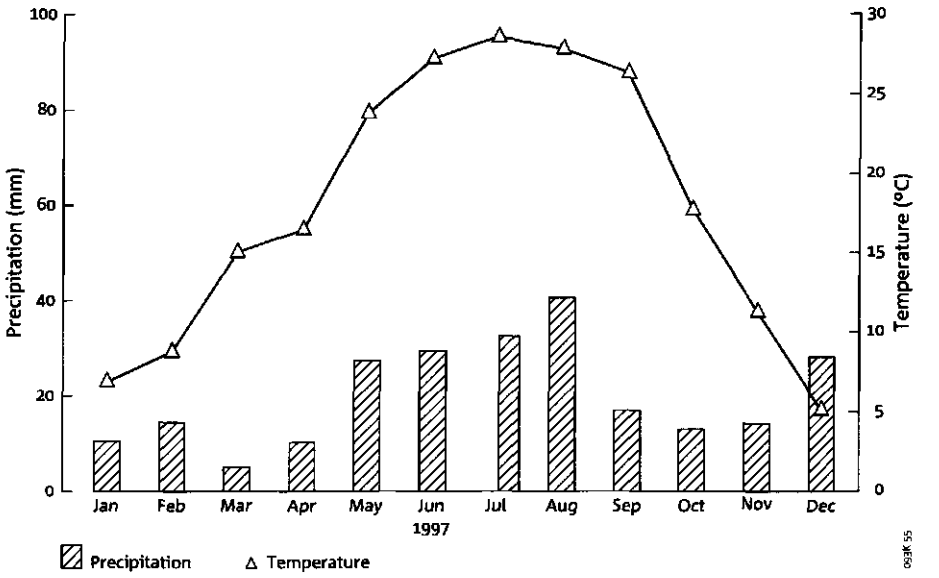

Figure 5.5: Annual trend of precipitation and temperature for the NMSU Jornada Range Weather Station in 1997.

Figure 5.6 shows that in the summer the average air temperature can rise well above 30 °C, whereas relative humidity is very low, resulting in a high evaporational demand, also because the amount of incoming solar radiation is very large.

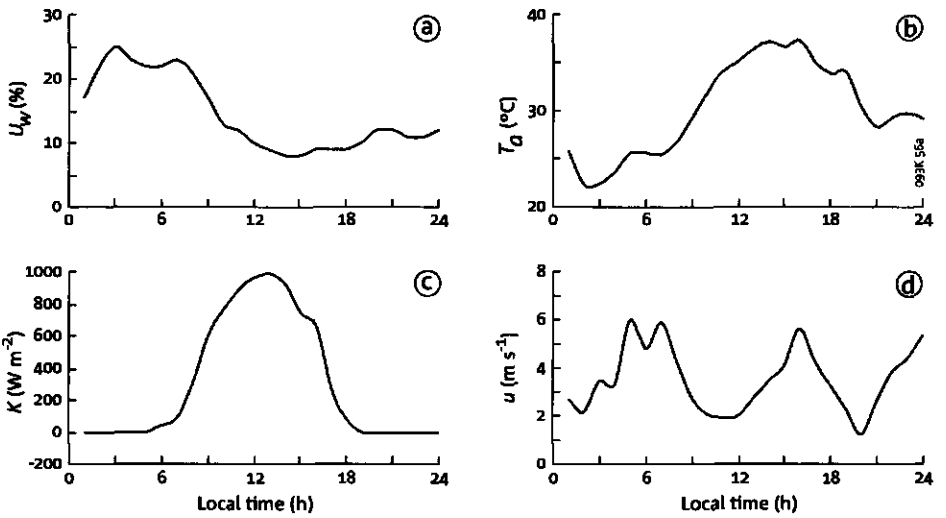

Figure 5.6: Daily course of a) relative humidity U_w, b) air temperature T_a, c) incoming shortwave radiation $K^{\downarrow}$ and d) windspeed u measured at the NSMU Jornada Range Weather Station, June 19, 1997.

The vegetation of the Jornada del Muerto plain is characteristic of a subtropical ecosystem in the hot desert biome. Grass communities dominated by black grama (*Bouteloua eriopoda*) have been susceptible to disturbances (such as prolonged drought and overgrazing). Encroachment by shrubs during the last century has been common. Large areas of former grassland, including the northern portion of the study area, are now dominated by honey mesquite (*Prosopis glandulosa*). This conversion resulted in the formation of coppice dunes on the deep, coarse-textured soils, increasing spatial heterogeneity of critically limited nutrients (especially N) required for plant growth (Schlesinger et al., 1990) as well as increasing wind erosion (Gibbens et al., 1993). The study area encompasses an ecotone between remnant black grama grassland and honey mesquite coppice duneland that developed during the past 80 years. Without subsequent intervention further desertification of this grassland is anticipated during the 21^{st} century.

Within the ecotone, three sites were chosen for intensive studies. The

sites were selected to represent a grass, mesquite, and grass-mesquite transition area. Black grama dominates the grass site which is within a long-term study area where grazing has been excluded. The site is relatively flat. Honey mesquite shrubs on coppice dunes dominate the mesquite site. The dunes vary in height from 1 to 4 m with honey mesquite on each of them. The area between the dunes is usually bare soil. The grass-shrub transition site (from now on indicated as transition site) is an area located between the grass and mesquite site with vegetation components from both. Some dunes are present but are usually less than 1 m high.

Since 1995 intensive mini-campaigns were held at the Jornada Experimental Range. All these campaigns lasted for about a week, and are planned to coincide with a Landsat TM overpass. In 1995 two campaigns have been executed: one in May (dry season) and another in September (wet season). Another three campaigns took place in 1996: February (winter), May (dry season) and September (wet season). In May/June and September 1997 another two campaigns took place. In each of these campaigns a wide range of airborne, satellite and ground measurements have been obtained. SC-DLO participated in the September 1995, September 1996 and September 1997 campaigns. The USDA-ARS Hydrology Lab is managing the JORNEX campaign.

5.2.2 Field data

The collection of ground data took place at the three sites mentioned above: mesquite, grass and transition site.

- **Thermal and multispectral measurements**

  A backpack-type apparatus (a "yoke") equipped with an IRT and an Exotech was used to make measurements over an area equivalent to one Landsat TM thermal band pixel (120*120m). Yoke measurements of temperature and radiance were made at the grass site during the September 1995 and September 1996 experimental period, during the aircraft flight and the Landsat overpass. At the other study sites surface temperatures were measured with hand-held Infra Red Thermometers (IRTs), during each flight for each study period. During the September 1997 campaign a hand held spectrometer (ASD) was employed to get spectral signatures of a large amount of vegetation species present in the Jornada Experimental Range.

- **Vegetation measurements**

  A transect of 150 m was established at each site. Within each line, height of the plants and litter were recorded. Also LAI measurements with a portable LI-COR instrument were made. Radiometric plant

canopy and soil reflactance measurements were taken at the grass and transition site in the September 1995 campaign.

- **Flux measurements**

  Surface energy fluxes have been measured continously since May 1995 using Bowen-ratio equipment at two sites: the grass site and the mesquite site. During the intensive field campaigns at these sites also eddy-correlation equipment has been used. At the transition site eddy correlation equipment was mounted at two heights in a 10 m high tower during the September 1995 field campaign. During the September 1996 campaign a 25 m high tower was placed.

- **Soil moisture measurements**

  During the September 1995 and 1996 campaigns soil moisture profiles were recorded with TDR at each site. The depth of the profiles varied from 0.5 m to 1 m.

5.2.3 Airborne remote sensing data

At each campaign radiometers mounted at aeroplanes were used to get remote sensing imagery with a high geometrical resolution. In this thesis use has been made of airborne Daedalus data. Some of the other airborne remote sensing data acquired will be introduced. Afterwards the Daedalus sensor will be discussed more extensively.

- **Video imagery**

  Video imagery was obtained with a three-camera multispectral digital video imaging system (Everitt et al., 1995). For the experiment the cameras were equipped with the following filters: visible yellow-green (0.555-0.565 μm), red (0.623-0.635 μm) and near infrared (0.845-0.857 μm). The system can store 1000 composite images of 640 $\times$ 480 pixel resolution. A GPS is integrated with the system. Imagery was acquired at altitudes of 300, 750 and 1500 m at the campaign of September 1995 and February 1996.

- **Thermal and Multispectral measurements**

  An Everest thermal infrared radiometer was used to get thermal airborne measurements. It has a band pass of approximately 8-13 ìm. An Exotech 4-band radiometer was used to make radiance measurements corresponding to the first 4 bands of the Landsat TM: blue (0.45-0.52 ìm), green (0.53-0.61 ìm), red (0.62-0.69 ìm) and near infrared (0.78-0.90 ìm). Flights were made on the days coinciding with a Landsat TM overpass.

Table 5.2: Configuration of the airborne Daedalus 1268 MSS sensor

Daedalus Band	TM Band	Wavelength interval (μm)
1	A	0.42 – 0.45
2	1	0.45 – 0.52
3	2	0.52 – 0.60
4	B	0.60 – 0.62
5	3	0.63 – 0.69
6	C	0.69 – 0.75
7	4	0.75 – 0.90
8	D	0.91 – 1.05
9	5	1.55 – 1.75
10	7	2.08 – 2.35
11	6	8.5 – 12.5 low gain
12	6	8.5 – 12.5 high gain
IFOV:	2.5 mrad	
Total Scan Angle:	86°	
Pixels/Scan line:	716	
Scan rate:	12.5/25/	
	50/100 scans s^{-1}	

- **Laser Altimetry**

  A laser altimeter used in the Jornex campaign is a pulsed gallium-arsenide diode laser, transmitting and receiving 4000 pulses per second at a wavelength of 904 nm. The vertical resolution was 5 cm for each measurement. Laser altimetry flights were made in May 1995, September 1995 and February 1996. In September 1995 also an imaging laser altimeter was flown.

- **Airborne Daedalus data**

  The Daedalus 1268 MultiSpectral Scanner (MSS) simulates the spectral characteristics of the Thematic Mapper multispectral scanners oribiting on Landsat 4 and Landsat 5. The seven TM bands are replicated with the MSS and four additional bands of discrete wavelengths are acquired. The MSS acquires TM band six (thermal infrared data) as two bands in low and high gain settings. The configuration of the scanner is given in Table 5.2.

  On June 19, 1997 three flight lines were flown over the Jornada Experimental Range. Two of those flights were flown at an altitude of 1524 m, resulting in a geometrical resolution of 4 m. In Figure 3.4 the two flight lines at an altitude of 1524 m are indicated. Also a third flight line at an altitude of 4877 m was flown, resulting in a geomet-

Table 5.3: Statistics of input images Jornada Experimental Range

Land surface characteristic	Site	Minimum	Maximum	Mean	Standard deviation
r_0 (-)	grass	0.093	0.228	0.138	0.014
	transition	0.098	0.220	0.156	0.015
	mesquite	0.097	0.223	0.176	0.021
T_0 (K)	grass	306.526	330.303	322.439	1.967
	transition	305.017	328.519	320.738	2.392
	mesquite	303.672	332.196	319.167	2.874
$NDVI$ (-)	grass	-0.039	0.312	0.025	0.018
	transition	-0.137	0.291	0.030	0.024
	mesquite	-0.058	0.338	0.017	0.041

rical resolution of 12 m. In all three cases the scan speed was 25 rps. The remote sensing data were gathered at approximately 17:00 GMT, which is around 10:00 h local time.

The remote sensing data were used to obtain the following land surface characteristics: r_0, T_0 and $NDVI$. The remote sensing data were corrected for atmospheric influences. In Table 5.3 the statistics for the input images of the Jornada Experimental Range are given. The standard deviation for all land surface characteristics is the smallest for the grass site and the largest for the mesquite site. The transition site, being a mixture of the other two sites has therefore a larger variability than the grass site but smaller than the mesquite site. The $NDVI$ for the Jornada ranges from -0.14 to 0.34 and indicates that there is very little green vegetation present. Mean values for all sites are around 0.02. n Plate B the r_0 image is given for the grass site. In Plate C and D the r_0 images are shown for the mesquite and transition site respectively.

5.3 The Netherlands

5.3.1 Location and climate

The climate in the Netherlands can be classified as a temperate oceanic climate with mild summers and cool winters using the revised Köppen climate classification (Rudloff, 1981). The weather is predominantly variable, with now and then periods of dry, sunny days alternated with rainy days. Storms are frequent and can be severe in coastal areas. The weather is mainly caused by depressions migrating generally from west to east. Sometimes a region of low or high pressure can be stationary over a wide area, causing stable weather for a period of several days or even weeks.

The field and remote sensing data of the Netherlands are all collected in the year 1995. Therefore a description of the climatic conditions of 1995 is given here (KNMI, 1996). In Figure 5.7 the annual trend of precipitation and temperature for the De Bilt weather station is shown, together with the average precipitation and temperature for the period 1961-1990.

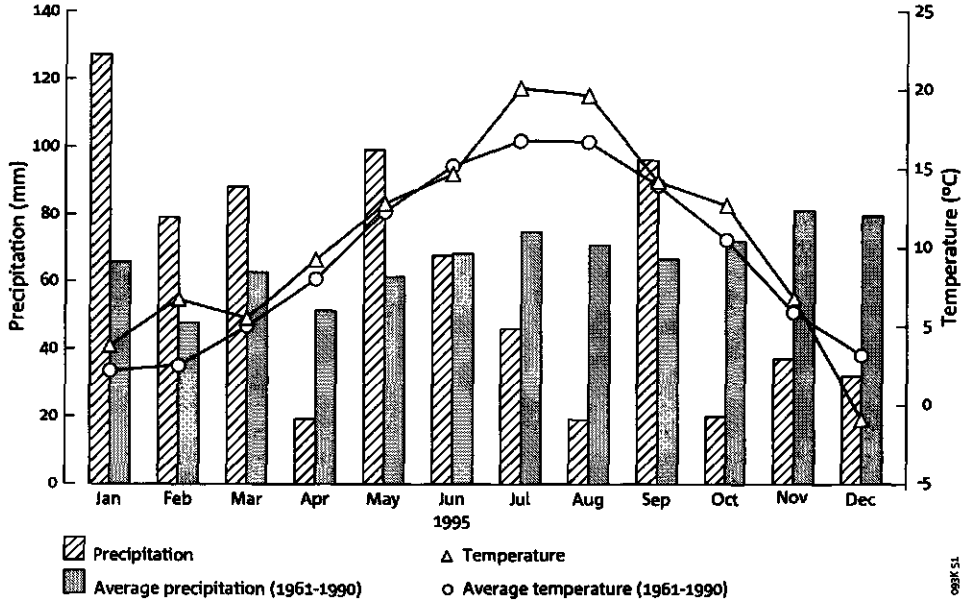

Figure 5.7: Annual trend of precipitation and temperature for the KNMI weather station De Bilt in 1995. Also the normal annual trend of precipitation and temperature based on the period 1961-1990 for De Bilt is shown.

The year 1995 was very warm, dry and had more sunshine than usual. The months of February, July, August and October were much warmer than normal. The summer was the 2nd warmest summer of the century. The average annual temperature was 10.4 °C against 9.4 ° C normally, making this the 5^{th} warmest year of the century until then. The annual precipitation of 739 mm was lower than usual: 792 mm. Most of the precipitation fell in the first three months of the year, which were wetter than usual. The months of April, August and October, November and December were much drier than in a normal year.

5.3.2 Field data

For the period of May to August meteorological data were obtained for four sites in the Netherlands. Two are maintained by the KNMI: Cabauw and Speulder forest. The other two are sites maintained by SC-DLO: Loo forest and Fledite forest. The location of the four sites is given in Figure 5.8.

Figure 5.8: Location of the meteorological measurement sites in the Netherlands. The box indicates the coverage of the Landsat TM scenes described in paragraph 5.3.2

- **Cabauw**

  The Cabauw measurement tower is situated in the western part of the Utrecht Province (51°58'16"N, 4°55'36" E), 2 kilometers northeast of the small village of Cabauw (Beljaars and Bosveld, 1997). The tower was designed and constructed by the KNMI for long-term meteorological research. The tower is 213 m high and has been operational since December 1972. Windspeed, temperature and wind direction are measured at different heights (10, 20, 40, 80, 140 and 200 m) of the tower. The tower is placed in a pasture where grass is the dominant vegetation cover. Open flat pastures and small villages surround the site. The river Lek flows 1 km south of the measurement tower. A large array of meteorological data is obtained on a half hourly basis. Most important for this research is the collection of radiation and energy balance data.

  In Figure 5.9 the daily course of solar radiation, air temperature, windspeed and sensible and latent heat flux at the Cabauw site is given for 11 July 1995. At this date also Landsat TM satellite data have been obtained, see Paragraph 5.3.3. The course of the solar radiation shows that in the morning no clouds were present. The amount of solar radiation steadily increases until noon. The air temperature follows the same course and reaches its peak of more than 30° C at 14:00h. In the afternoon clouds are present, decreasing the amount of solar radiation to almost 0 at 16:00h local time. Therefore the temperature drops also more rapidly than expected for a cloud-free day. Wind speed is more or less constant with some variation during the day, and decreases during the night. The daily course of the latent and sensible heat flux show that the vegetation present at the site uses approximately 80% of the available energy for evaporation. Because of the presence of clouds the latent heat flux drops rapidly in the afternoon.

- **Speulder Forest**

  The Speulder Forest site (52°15'07"N, 5°41'21"E) is part of an extensive forest area, which is bordered in the east by a heather area at approximately 1.5 km (Bosveld et al., 1993). In all other directions the forest extends over at least 4 km. Within this area the topography is slightly undulating with height variations of 5 to 10 m. The research site is a forest stand of 2.5 ha of Douglas Fir (*Pseudotsuga menziesii*) planted in 1962. Tree height ranges from 16 to 20 m. Leaf area index is approximately 10 but varies throughout the year. The stand is very dense at the forest interior and no understory vegetation is present. The groundwater level is at 40 m below the surface, therefore capillary rise to the root zone can be ignored. The instruments are mounted at different levels of the 36 m high measurement tower: 4, 18, 24, 30 and 36 m. Also here at this site radiation and energy balance measurements

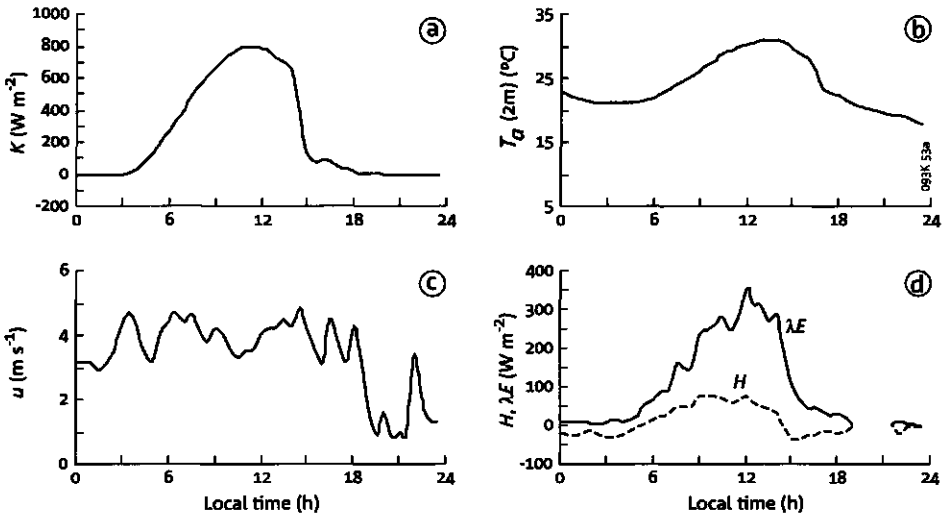

Figure 5.9: Daily course of a) incoming shortwave radiation $K^{\downarrow}$, b) air temperature T_a, c) windspeed u and d) sensible heat flux H (dotted line) and latent heat flux λE (solid line) at the Cabauw site, July, 11, 1995

are made on a half hourly basis during 1995.

- **Fledite Forest**

  The 24 m high measurement tower in the Fledite forest (52°19'06"N, 5°27'12"E) is situated in the southeast part of the Flevoland province (Elbers et al., 1996). Within a radius of 500 m 93% of the vegetation consists of forest, the main type being the populus (*Populus*). At the site the latent, sensible and momentum fluxes have been measured almost continuously during 1995. Also soil moisture content and atmospheric variables like precipitation and windspeed have been measured. The groundwater level is about 1.5 m below soil surface.

- **Loo Forest**

  The 22 m high measurement tower in the Loo forest (52°10'00"N, 5°44'38"E) is situated in the western part of the Gelderland province (Elbers et al., 1996). The Loo forest is part of the forestry of Kootwijk. Large parts of the forest are planted on sand dunes. The topography is therefore also slightly undulating with height differences of 10 m maximum. The main type of tree in this forest is the Scots pine (*Pinus Silvestrus*) planted around 1900. Other types present are birch (*Betula*), Douglas fir (*Pseudotsuga menziesii*) and oak (*Quercus*). Within the forest stand some open areas are present, with as main vegetation type heather. At this site the same array of variables measured at the

Table 5.4: Specifications of Landsat TM

Band	Wavelength interval (μm)
1	0.45 – 0.52
2	0.52 – 0.60
3	0.63 – 0.69
4	0.76 – 0.90
5	1.55 – 1.75
6	10.4 – 12.5
7	2.08 – 2.35
Geometrical Resolution	30 m, band 6: 120 m
Temporal Resolution	16 days

Fledite forest are measured here also.

5.3.3 Remote sensing data

Because of the unusual high amount of sunny days in the summer of 1995 four almost cloudless Landsat TM satellite scenes could be obtained in that time period. Useful Landsat TM scenes were captured at May 24, June 25, July 11 and August 12. In Figure 5.8 the coverage of the Landsat imagery is shown. Almost half of the Netherlands is covered. Only the northern part of the Netherlands as well as some parts of the eastern provinces were not covered. The main specifications of the Landsat TM satellite are given in Table 5.4

The Landsat data have been used to derive the following land surface characteristics: r_0, T_0 and $NDVI$. All land surface characteristics have been corrected for atmospheric influences using field measurements of r_0 and T_0 and conversion factors given by Markham and Barker (1985).

In Table 5.5 the statistics of the land surface characteristics derived from the four Landsat TM images of the Netherlands are shown. Table 5.5 shows that the surface albedo remains constant throughout the year, with the exception for the 25 June image. The standard deviation of the surface albedo is larger for the May and August images compared to the June and July images. The mean T_0 increases from May to August. The standard deviation for the T_0 is the largest for 24 May. This is mostly due to the effect that the difference between the T_0 of the open water bodies and land surface decreases during these four months. The $NDVI$ images show that the maximum mean $NDVI$ occurs at 25 June, and then gradually decreases. This could be the effect of plant senescence, limited water supply or early harvesting.

For the length scale and aggregation analysis of the Landsat TM data a subset has been chosen of 2560*2048 pixels encompassing the Central Part of

Table 5.5: Statistics of the land surface characteristics r_0, T_0 and $NDVI$, derived from Landsat TM satellite data for the Central Part of the Netherlands

Land surface characteristic	Date	Minimum	Maximum	Mean	Standard Deviation
r_0 (-)	24/5/1995	0.010	0.701	0.193	0.049
	25/6/1995	0.037	0.670	0.169	0.037
	11/7/1995	0.035	0.660	0.199	0.043
	12/8/1995	0.020	0.725	0.197	0.049
T_0 (K)	24/5/1995	281.51	315.62	297.79	2.635
	25/6/1995	283.36	317.44	299.37	2.540
	11/7/1995	292.93	321.42	302.74	2.202
	12/8/1995	291.49	319.80	304.62	2.198
$NDVI$ (-)	24/5/1995	-0.31	0.85	0.584	0.192
	25/6/1995	-0.50	0.88	0.607	0.213
	11/7/1995	-0.28	0.82	0.561	0.159
	12/8/1995	-0.35	0.89	0.529	0.167

the Netherlands. This subset has been subdivided into 20 equally sized grids of 512*512 pixels. The grids have been numbered 1 to 20 from the upper left to the bottom right. Plate E shows the r_0 derived from the original Landsat TM image for the subset together with the outlay of the 20 grids. Three grids are highlighted. In Plates F, G and H the r_0 images are shown for respectively the grids 3, 8 and 11. These grids will be discussed in more detail in Chapter 6

Chapter 6

Length scale analysis

This Chapter presents the results of the length scale analysis for the three test sites described in Chapter 5. The length scale analysis will be based on the wavelet analysis described in Paragraph 4.6. The wavelet variance will be used to describe the variance for each length scale ℓ^* (m). The dominant length scale, ℓ^*_{dom} (m) is defined as the scale for which the maximum wavelet variance is calculated. The Haar wavelet is chosen to calculate the wavelet variance. In Paragraph 4.7 it was shown that the Haar wavelet is the best wavelet for determining length scales.

6.1 Case study Barrax

6.1.1 Wavelet analysis

In Figure 6.1 the wavelet variance for all three land surface characteristics r_0, T_0 and $NDVI$ is shown. In order to compare it for all three land surface characteristics the wavelet variance has been scaled as a relative fraction to the total wavelet variance. The wavelet variance curve has a similar shape for all three land surface characteristics. The curves show that ℓ^*_{dom} is located at 296 m. This coincides with the mean size of the pivot irrigation systems. Therefore the pivots are the dominant factor in determining the variance for all land surface characteristics.

In Table 6.1 the ℓ^*_{dom} for the three land surface characteristics are shown. The percentage of variance explained by ℓ^*_{dom} is given, together with the percentage of variance explained by $\ell^* \geq \ell^*_{dom}$. The latter simulates the situation where the resolution of the sensor is equal to that of the dominant length scale.

From Table 6.1 it is clear that most of the variance is explained by the length scales larger and equal to $\ell^*_{dom} = 296$ m. The amount of variance explained by ℓ^*_{dom} is for all three land surface characteristics equal: $\pm 18\%$. If you would observe the area with a sensor with a geometrical resolution

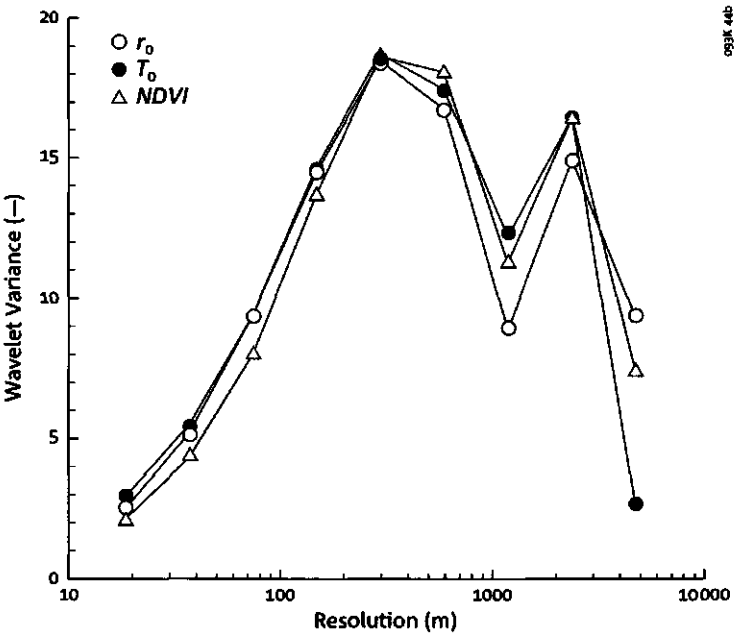

Figure 6.1: Wavelet variance of land surface characteristics derived from airborne TMS-NS001 data, Barrax, June 29, 1991: a) surface albedo r_0 b) surface temperature T_0 and c) Normalized Difference Vegetation Index $NDVI$

Table 6.1: Statistics of the wavelet analysis for the land surface characteristics r_0, T_0 and $NDVI$, derived from airborne TMS-NS001 data, Barrax, June 29, 1991

Land surface characteristic	ℓ^*_{dom}	Variance explained by dominant length scale	Variance explained by $\ell^* \geq \ell^*_{dom}$
	(m)	(%)	(%)
r_0	296	18.48	68.41
T_0	296	18.73	67.50
$NDVI$	296	18.62	71.86

equal to 296 m around 70% of the spatial variability would be captured. The remaining 30% would be lost.

6.2 Case study Jornada Experimental Range

6.2.1 Wavelet analysis

In Figure 6.2a the wavelet variance of r_0 for the three sites is shown. The three curves have a completely different shape. For the Mesquite site most of the variability is present at the smallest length scale of 4 and 8 m, which coincides with the average size of the dunes in this area. The wavelet variance for the grass site shows an almost flat shape, showing that there is considerable variability present at all scales. However the amount of variability is much smaller compared to the mesquite site. The transition site finally shows two peaks, ℓ^*_{dom} is located at 512 m and a second peak is located at 4 m. The peak at 4 m is due to the fact that there are mesquite shrubs present in the area, and the peak at 512 m can be explained because distinct regions of mesquite and grass are present.

In Figure 6.2b the wavelet variance of T_0 for the three sites is shown. In contrast to the wavelet variance curves for r_0, the wavelet variance curves for T_0 have a similar shape for all three sites. Most of the variability is explained by both the smallest length scales (4 - 8 m) and the largest length scales (512 - 1024 m). There is almost no spatial variability present at the remaining length scales (16 - 256 m). Also here the spatial variability present at the mesquite site is much larger than the spatial variability present at the grass site.

In Figure 6.2c the wavelet variance of the $NDVI$ for the three sites is shown. All three sites show that the wavelet variance curve has a similar shape, most of the spatial variability is explained by the smallest length scales, 4 and 8 m. Almost none of the spatial variability is present at larger length scales.

Comparing the three sites for all three land surface characteristics, the mesquite site contains much more spatial variability than the grass site . The reason is that the mesquite site is composed of bare soil and mesquite bush, two features that have larger differences in r_0, temperature and $NDVI$. The grass site is covered mostly by black grama, with some areas of bare soil. The differences in T_0, r_0 and $NDVI$ is not as large between black grama and bare soil, as between mesquite and bare soil. The transition site is a transition zone between the grass and mesquite site, showing that the transition site is composed of both black grama and mesquite bush together with bare soil. The overall variability of the transition zone is therefore larger than the grass site but smaller than the mesquite site. The decrease in wavelet variance for the mesquite site for all surface characteristics indicates that the dominant length scales for the land surface characteristics is at the smallest scale for

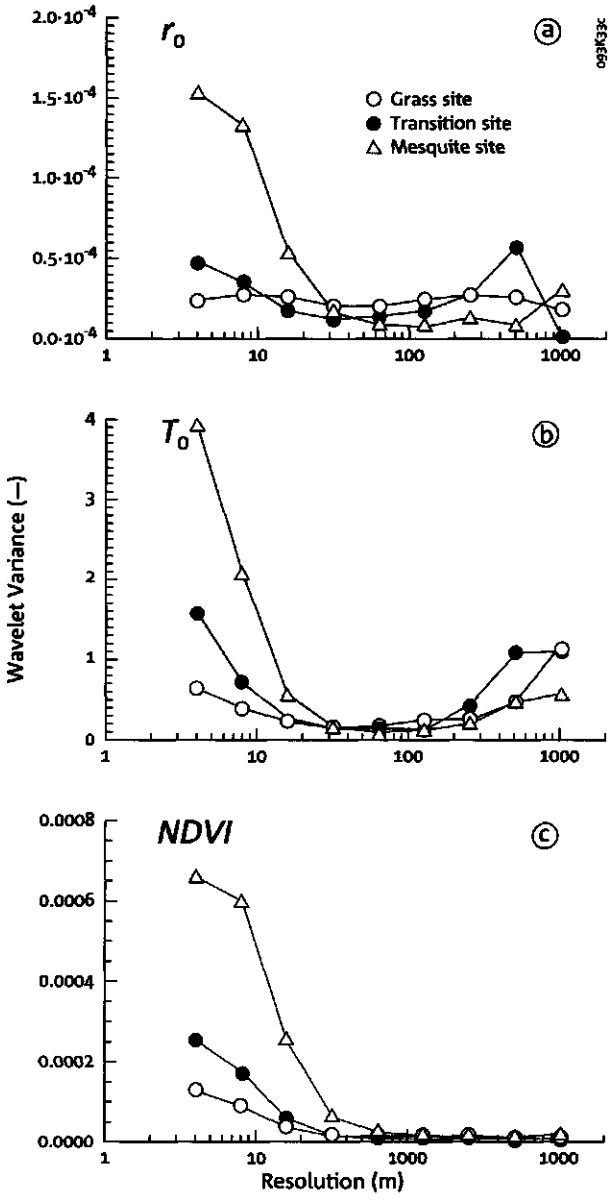

Figure 6.2: Wavelet variance of land surface characteristics derived from airborne Daedalus data, June 19, 1997, Jornada experimental range: a) surface albedo r_0 b) surface temperature T_0 and c) Normalized Difference Vegetation Index $NDVI$

Table 6.2: Statistics of the wavelet analysis for the land surface characteristics r_0, T_0 and $NDVI$, derived from Daedalus data, June 19, 1997, Jornada Experimental Range

Land surface characteristic	Site	Dominant length scale (m)	Variance explained by ℓ^*_{dom} (%)	Variance explained by $\ell^* \geq \ell^*_{dom}$ (%)
r_0	Grass	8	12.91	88.79
	Transition	512	25.00	25.49
	Mesquite	4	36.13	100.00
T_0	Grass	1024	31.21	31.21
	Transition	4	27.97	100.00
	Mesquite	4	47.52	100.00
$NDVI$	Grass	4	40.31	100.00
	Transition	4	45.87	100.00
	Mesquite	4	40.30	100.00

this site 4 m. It seems that the mosaic of dunes and bare soil areas is the most important characteristic, which governs the spatial pattern of r_0, T_0 and $NDVI$.

In Table 6.2 the statistics of the wavelet analysis for the land surface characteristics for the three sites are given. For the mesquite site ℓ^*_{dom} is 4 m, explaining between 36 and 47 % of the variability. Only for the $NDVI$ of the grass and transition sites ℓ^*_{dom} is also 4 m explaining about 40% of the spatial variability. For the surface albedo of the grass site ℓ^*_{dom} is 8 m explaining only 13% of the spatial variability. In all cases the spatial resolution to use to capture all spatial variability is 4 m. A spatial resolution larger than 4 m would miss a substantial part of the variability present in the landscape. The question remains if 4 m is sufficient to capture all spatial variability in this complex landscape. While it appears sufficient for the mesquite site a higher resolution is needed for the grass site. Within the grass site a resolution equal to the size of the bare soil areas and plant communities, which is less than 1 m would be needed.

6.3 Case study The Netherlands

The data set for the Netherlands consists of 4 Landsat TM images obtained in the summer of 1995: 24 May, 25 June, 11 July and 12 August. Due to computational limits part of the whole TM scene has been used in the length scale analysis. A subset of 2560 columns and 2048 rows has been chosen instead. The subset shows the Central Part of the Netherlands. Plate E

shows the subset.

6.3.1 Wavelet analysis

Because the wavelet analysis only works for square images, the images with a size of 2560 and 2048 columns have been subdivided into 20 grids of 512 rows by 512 columns. Plate E shows the subdivision of the Landsat TM image into 20 grids. First the mean results derived from all the wavelet analysis of all 20 grids are discussed. After that three grids are discussed in more detail focusing on the differences in response of the wavelet variance for different types of land surfaces. The temporal effect on the wavelet variance will be studied using the four Landsat TM images.

All grids

The wavelet analysis has been applied to the three land surface characteristics, r_0, T_0 and $NDVI$ derived from Landsat TM images at four different dates. Therefore 12 images have been analyzed. For the statistics of the land surface characteristics for each image see Table 5.5. Grids with clouds in it were excluded from the wavelet analysis.

In Figure 6.3a the wavelet variance for r_0 for the four different dates is shown. The wavelet variance plotted here is derived as the mean of the wavelet variance curves of all grids. The shape of the wavelet variance curve is for all four dates similar. At 1920 m ℓ^*_{dom} is located, there is also a second peak, although less dominant, inbetween 120 and 240 m. The length scale of 1920 m is probably due to the size of the large scale features in the dutch landscape: cities, forests and open water bodies. The second peak at the length scales of 120 and 240 m is probably due to the size of the agricultural fields in the Netherlands. The amount of variance differs for the four dates. The images of 24 May 1995 and 12 August 1995 show more variance than the images of 11 July 1995 and 25 June 1995. This is also illustrated in Table 5.5 where the minimum and maximum values for r_0 are respectively smaller and larger for the images of 24 May 1995 and 12 August 1995.

In Figure 6.3b the wavelet variance for T_0 for the four different dates is shown. While the resolution of the thermal infrared band of Landsat TM is 120 m, the wavelet variance for the pixels smaller than 120 m is small. The wavelet variance at those length scales is not equal to zero, because of the leakage of the Haar wavelet to smaller length scales and because the image is turned slightly due to the geometrical correction. All four dates show a similar shape for the wavelet variance curve. At 1920 m ℓ^*_{dom} is located, equal to the result for the r_0. The amount of variance varies from one date to another. The variance is largest for the image obtained at 24 May 1995. This is probably due to the effect that the largest difference between T_0 for an open water bodies and T_0 for the land surface occurs at this date.

In Figure 6.3c the wavelet variance for the $NDVI$ for the four different dates is shown. The shape of all the $NDVI$ wavelet variance curves for 24 May and 25 June is similar to the one derived in the analysis of the r_0 images. There is a peak located at 1920 m, and a second less dominant peak located between 120 and 240 m. The wavelet variance curves for 11 July and 12 August are slightly different. The ℓ^*_{dom} is still 1920 m, but the second peak has disappeared. This is probably caused by the fact that now for all "green" surfaces (pasture, agricultural fields, forest) in the Netherlands the $NDVI$ has about the same value, resulting in no particular length scale for those type of surfaces. The wavelet variance decreases for the $NDVI$ from 25 June 1995 to 12 August 1995. This could be the effect of plant senescence, limited water supply and/or early harvesting.

Selected grids

Because the Netherlands is a composite of different types of landscapes the wavelet analysis for three grids are discussed here separately. Plate E shows an overlay with the twenty grids. The grids are numbered from 1 in the upper left corner to 20 in the lower right corner, counting first from left to right and then from top to bottom. The grids 3, 8 and 11 are selected. Grid 3 shows a mixture of open water and agricultural fields with the larger fields located in the "Flevopolder", in the north of the grid and the smaller fields in the south of the grid. Grid 8 shows a very heterogeneous landscape with forests in the southwest, some cities in the middle of the grid and agricultural fields in the north and east. Grid 11 consists mostly of small sized parcels, mostly pasture, delineated by canals and some small cities.

In Figure 6.4a the wavelet variance for r_0 obtained at 24 May 1995 for the three grids is shown. The wavelet variance for the other dates are not shown, because they have a similar shape, like in the previous analysis for all grids. The wavelet variance for r_0 of grid 3 shows that ℓ^*_{dom} for this grid is located at the length scale of 1920 m. The amount of variance is also much larger than for the other two grids. This is mainly caused by the fact that a large body of water is present in the grid. The r_0 of water has a much lower value than for any other surface type, therefore causing a larger variance. The wavelet variance at the size of the water body is therefore much larger. The wavelet variance curve for r_0 of grid 8 shows that the amount of variance is almost equal for each scale. However the largest variance can be found at length scales larger than 3840 m. This is because half of grid 8 is occupied by forest and half by agricultural fields and cities. However in this complex landscape there seems to be no dominant length scale. The wavelet variance obtained for the r_0 of grid 11 shows that for an agricultural landscape of small parcels the majority of the variance is explained by the smaller length scales (30 - 240 m), with ℓ^*_{dom} located at 30 m.

In Figure 6.4b the wavelet variance for T_0 obtained at 24 May 1995 for

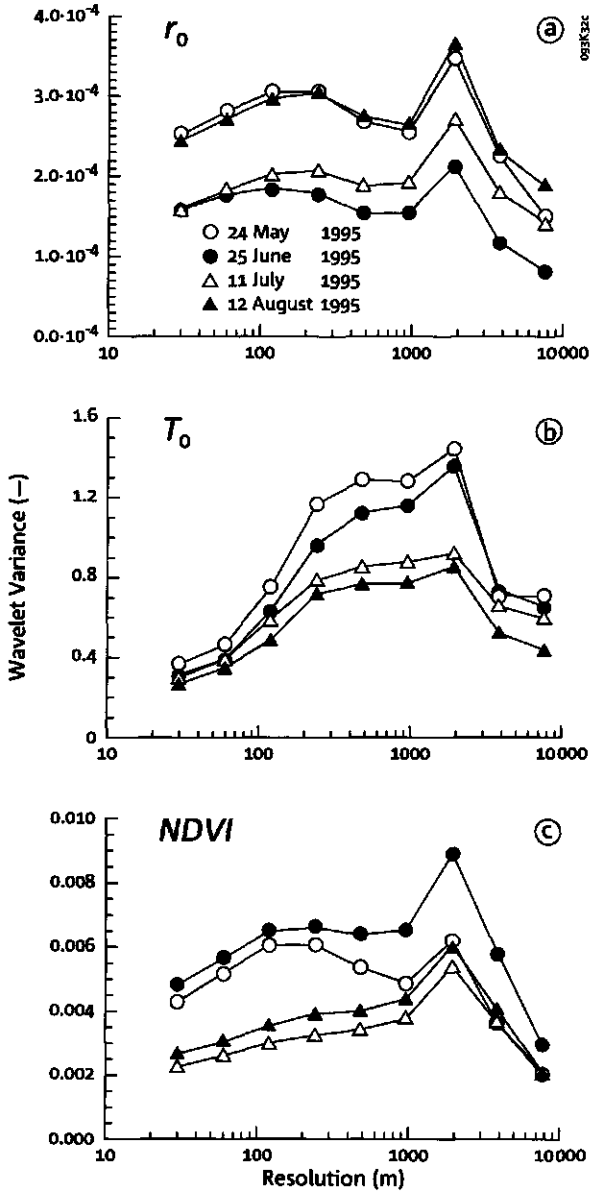

Figure 6.3: Wavelet variance of land surface characteristics derived from Landsat TM images for the Central Part of the Netherlands at four different dates: a) surface albedo r_0 b) surface temperature T_0 and c) Normalized Difference Vegetation Index $NDVI$

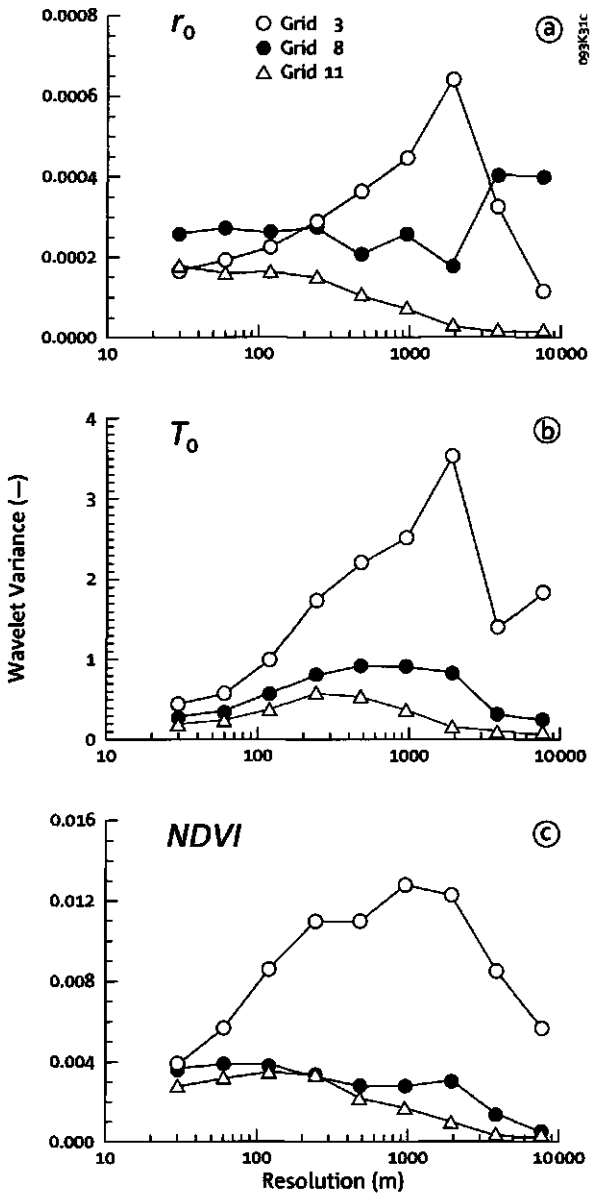

Figure 6.4: Wavelet variance of land surface characteristics derived from Landsat TM images at May 24, 1995 for three different grids: 3, 8 and 11. For the location of the grids see Plate E, a) surface albedo r_0 b) surface temperature T_0 and c) Normalized Difference Vegetation Index $NDVI$

the three grids is shown. The wavelet variance for T_0 of grid 3 shows that, similar to r_0, ℓ^*_{dom} of this grid is located at 1920 m. However the wavelet variance of the T_0 for grid 8 shows that ℓ^*_{dom} is no longer located at 3840 and 7680 m. The temperatures of the forest and agricultural fields are more or less similar. The size of the cities which are warmer than the surrounding area is here the dominant factor, leading to a ℓ^*_{dom} of 480 m, although at $\ell^* = 960$, 1920 m considerable variability is present. The wavelet variance for T_0 of grid 11 shows that ℓ^*_{dom} is 240 m. Regarding the fact that the resolution of the T_0 image is 120 m, one still can say that for grid 11 most of the variance is explained by the smaller length scales: 120, 240 and 480 m.

In Figure 6.4c the wavelet variance for the $NDVI$ obtained at 24 May 1995 for the three grids is shown. The wavelet variance for the $NDVI$ of grid 3 shows that ℓ^*_{dom} of this grid is located at 960 m. The wavelet variance of the $NDVI$ for grid 11 shows that the variance decreases from the smallest length scale to the largest length scale. The size of the parcels is here the dominant factor. The wavelet variance of the $NDVI$ for grid 8 shows an almost flat wavelet variance curve, meaning that the variance is evenly divided over all scales, representing the complexity of this heterogeneous landscape.

In Table 6.3 ℓ^*_{dom} for each land surface characteristic obtained from the wavelet analysis for grids 3, 8 and 11 and all grids is shown. The percentage of variance explained by ℓ^*_{dom} is given, together with the percentage of variance explained by $\ell^* \geq \ell^*_{dom}$. The latter simulates the situation where the resolution of the sensor is equal to that of the dominant length scale.

Table 6.3: Statistics of the wavelet analysis for the land surface characteristics r_0, T_0 and $NDVI$, derived from Landsat TM data for the Central Part of the Netherlands

Land surface characteristic	Grid	Date	ℓ^*_{dom} (m)	Variance explained by ℓ^*_{dom} (%)	Variance explained by $\ell^* \geq \ell^*_{dom}$ (%)
r_0	All	24/5	1920	14.51	30.21
		25/6	1920	15.05	29.06
		11/7	1920	15.69	34.40
		12/8	1920	15.04	32.20
	3	24/5	1920	23.27	39.10
		25/6	1920	22.44	36.69
		11/7	1920	22.06	38.12
		12/8	1920	21.09	44.52
	8	24/5	3840	16.02	31.94
		25/6	7680	14.86	14.86
		11/7	7680	18.81	18.81

continued on next page...

Table 6.3: Statistics of the wavelet analysis for the land surface characteristics r_0, T_0 and $NDVI$, derived from Landsat TM data for the Central Part of the Netherlands

Land surface characteristic	Grid	Date	ℓ^*_{dom} (m)	Variance explained by ℓ^*_{dom} (%)	Variance explained by $\ell^* \geq \ell^*_{dom}$ (%)
		12/8	7680	16.84	16.84
	11	24/5	30	20.23	100.00
		25/6	30	21.04	100.00
		11/7	30	18.24	100.00
		12/8	30	19.26	100.00
T_0	All	24/5	1920	17.66	34.96
		25/6	1920	18.47	37.43
		11/7	1920	15.41	36.30
		12/8	1920	16.49	34.96
	3	24/5	1920	23.12	44.26
		25/6	1920	24.17	39.58
		11/7	1920	20.53	55.15
		12/8	1920	24.26	44.27
	8	24/5	480	17.54	61.44
		25/6	1920	18.41	33.48
		11/7	1920	17.35	34.88
		12/8	480	17.53	63.17
	11	24/5	240	21.92	68.78
		25/6	1920	18.41	33.48
		11/7	1920	17.35	55.15
		12/8	1920	17.53	63.17
$NDVI$	All	24/5	1920	14.18	27.05
		25/6	1920	16.45	32.65
		11/7	1920	18.34	37.80
		12/8	1920	17.90	36.12
	3	24/5	960	16.08	49.45
		25/6	960	17.17	54.30
		11/7	1920	18.18	44.66
		12/8	960	18.55	56.36
	8	24/5	60	15.48	85.45
		25/6	60	15.75	84.90
		11/7	1920	18.75	29.87
		12/8	1920	17.63	27.96
	11	24/5	120	19.00	67.11

continued on next page...

Table 6.3: Statistics of the wavelet analysis for the land surface characteristics r_0, T_0 and $NDVI$, derived from Landsat TM data for the Central Part of the Netherlands

Land surface characteristic	Grid	Date	ℓ^*_{dom} (m)	Variance explained by ℓ^*_{dom} (%)	Variance explained by $\ell^* \geq \ell^*_{dom}$ (%)
		25/6	120	19.04	63.50
		11/7	240	17.74	53.55
		12/8	240	17.44	56.77

Table 6.3 shows that for the case study of the Netherlands the percentage of variance explained by ℓ^*_{dom} lies always within the range of 14 and 24%. A value of 1920 m for ℓ^*_{dom} is most frequently mentioned for all grids in Table 6.3. Suppose that a sensor with a resolution of 1920 m would observe this test area then less than 35% of the variance present in the landscape would be captured. Still a sensor with a higher resolution would be needed to capture all spatial variability. Therefore ℓ^*_{dom} cannot be used as a measure for the optimal sensor resolution.

6.4 Optimal sensor resolution

The Tables 6.3, 6.2, 6.3 show that ℓ^*_{dom} is not a good measure for the optimal sensor resolution. In some cases even less than 20% of the variance is explained by ℓ^*_{dom}. A better measure would be the length scale which would explain $\geq 90\%$ of the variance. In Table 6.4 for all test sites these length scales are given, ℓ^*_{dom} is also given in order to compare both length scales.

Table 6.4 shows that for all land surface characteristics and locations the ℓ^* which explains at least 90% of the variance is smaller or equal to ℓ^*_{dom}. This leads to the conclusion that ℓ^*_{dom} is not suited for the choice of the optimal sensor resolution.

The length scale analysis is of particular interest to the aggregation analysis by means of linearization explained in Paragraph 3.2. The cumulative wavelet (co)variance is equal to the (co)variance $\boldsymbol{p}$ in Equation 3.7. The wavelet (co)variance should be cumulated up to the scale level of the aggregated results. This is only valid when the Haar wavelet is used. Looking at the results of the length scale analysis, the ℓ^*_{dom} is the length scale at which the largest aggregation difference will occur.

Table 6.4: Choice of the optimal sensor resolution based on the wavelet analysis for the three test sites.

Scene	Description	$\ell^*_{90\%}$ (m)	ℓ^*_{dom} (m)	Variance ($\ell^* \geq \ell^*_{dom}$) (%)
Barrax	r_0	74	296	68.41
	T_0	74	296	67.50
	$NDVI$	148	296	71.86
Jornada	r_0, grass	4	8	88.79
	r_0, mesquite	4	512	25.49
	r_0, transition	4	4	100.00
	T_0, grass	4	1024	31.21
	T_0, mesquite	4	4	100.00
	T_0, transition	4	4	100.00
	$NDVI$, grass	4	4	100.00
	$NDVI$, mesquite	4	4	100.00
	$NDVI$, transition	4	4	100.00
The Netherlands	r_0, 24/5	120	1920	30.21
	r_0, 25/6	120	1920	29.06
	r_0, 11/7	60	1920	34.40
	r_0, 12/8	60	1920	34.20
	T_0, 24/5	60	1920	34.96
	T_0, 25/6	60	1920	37.43
	T_0, 11/7	60	1920	36.30
	T_0, 12/8	60	1920	34.96
	$NDVI$, 24/5	60	1920	27.05
	$NDVI$, 25/6	60	1920	32.65
	$NDVI$, 11/7	60	1920	37.80
	$NDVI$, 12/8	60	1920	36.12

Chapter 7

Aggregation of land surface characteristics

In this chapter the results of the aggregation analysis for the three test sites will be discussed. This will be done following the two different paths described in Figure 3.1. This will give insight in how the resolution of radiometric observations, which are used as input data, influences the results of a land surface model, in this particular case SEBI. The difference obtained by following either path A or B, which is said to be the error due to aggregation, will also be estimated by the two approaches described in Chapter 3 : the linearization approach and the convex hull approach.

In the remainder of the chapter the following nomenclature for the different resolutions of the data sets is used. A high resolution observation is equal to the resolution of the original data set. A low resolution observation applies to a data set with a pixel size larger than the original data set. A grid cell resolution observation applies to a data set where the entire area is covered by one single pixel.

This chapter focuses on the description of the error due to aggregation of a data set from a high resolution towards a lower resolution up to a grid cell resolution. For the Barrax case study three different options have been investigated.

The first option is the representation of the error due to aggregation for the *actual situation.* High resolution data have been used to derive the SEBI results and consequently the area average value for respectively H, λE and Λ has been derived. This result is compared to the area average value derived from low resolution data, up to the grid cell resolution.

The second option is an estimation of the error due to aggregation of the data set based on the *linearization approach.* The linearization approach uses information about the variance and covariance of the input variables together with an estimation of the distribution of the input variables. Here the mean, median and modus values of the input variables have been chosen

to represent the distribution of the input variables and can be thought of representative for the area. The results of the wavelet analysis have been used to infer the variance and covariance of the input variables for the different resolutions.

The third option is an estimation of the error due to aggregation for data set with a grid cell resolution based on the *convex hull approach*. The range of possible solutions for a data set obtained at a grid cell resolution has been derived. Information on the spatial variability of the input variables is needed. Three different options have been investigated. One where the spatial variability is derived from the high resolution data set, another where 1% of the information derived from the high resolution data set is used to infer spatial variability and finally where low resolution data has been used to infer spatial variability.

The linearization approach and convex hull approach will also be used in predicting the error due to aggregation for the remaining data sets: Jornada and the Netherlands.

7.1 Case study Barrax

7.1.1 Application of SEBI

The SEBI model has been applied using the TMS-NS001 data set recorded on 29 June 1991 to derive the three spatially distributed land surface characteristics r_0, T_0 and $NDVI$. The remaining input variables which are taken as constant for the complete Barrax site have been either obtained from field measurements or from radio soundings. In Table 7.1 the values for the areally constant input variables are given. The output of SEBI consists of spatially distributed values of H, λE and Λ.

Table 7.1: Areally constant input variables for SEBI, Barrax, 29 June 1991.

Input variable	Value	Source
h_i	750 m	Radio Sounding
θ_h	300.15 K	Radio Sounding
p_h	85986.1 Pa	Radio Sounding
q_h	0.0093 kg kg^{-1}	Radio Sounding
p_s	94045 Pa	Field Measurement
u^*	0.525 m s^{-1}	Field Measurement
f_{z_0}	0.025	-
$K^{\downarrow}$	860 W m^{-2}	Field Measurement
$L^{\downarrow}$	372 W m^{-2}	Field Measurement

The principle behind SEBI described in Chapter 2 can be illustrated with Figure 7.1 where for a small percentage ($\approx 0.5\%$) of the pixels the observed

temperature difference $(T_0 - T_a)$ and the theoretically derived temperature differences for zero evaporation $(T_0 - T_a)_0$ (upper boundary) and maximum evaporation $(T_0 - T_a)_{max}$ (lower boundary) are given. The values of $(T_0 - T_a)$ lie clearly between the theoretical boundaries for all pixels: $(T_0 - T_a)_{max}$ and $(T_0 - T_a)_0$, indicating that the value of Λ will lie between 0 and 1, see Equation 2.60. The slope of the upper boundary is predominantly determined by the decrease of net available energy $Q^* - G_0$ due to the increase of r_0, see Equation 2.58. The slope of the lower boundary is less steep because the decrease of $Q^* - G_0$ is being compensated by the increase of the vapor deficit $(e^* - e)$, see Equation 2.57.

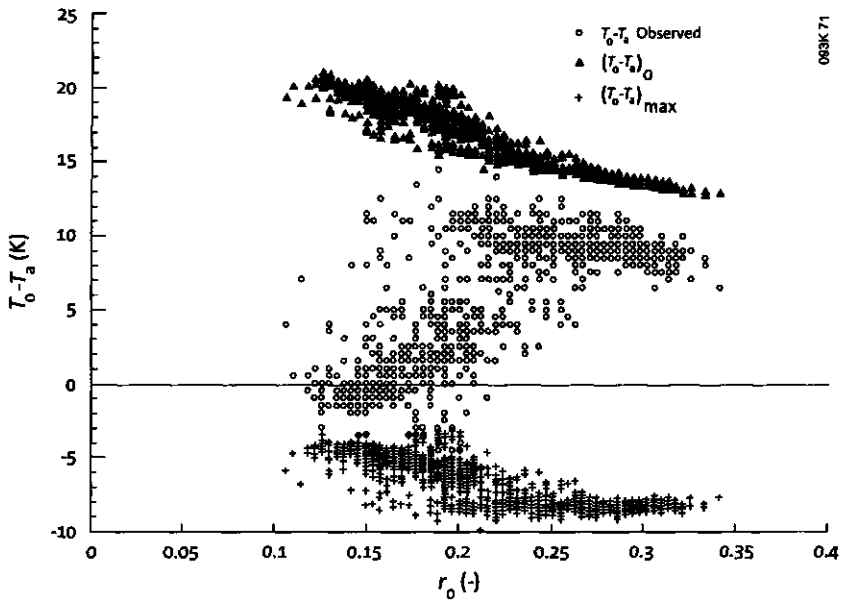

Figure 7.1: Observed Temperature difference, $(T_0 - T_a)$ plotted together with the theoretically derived temperature differences for zero evaporation $(T_0 - T_a)_0$ (upper boundary) and maximum evaporation $(T_0 - T_a)_{max}$ (lower boundary) for $\approx 0.5\%$ of the pixels from the TMS-NS001 image obtained at the Barrax site, 29 June 1991

The factor f_{z_0}, defined in Equation 2.64, has been used to set the ratio between $z_{0,m}$ and $z_{0,h}$. This ratio is still the bottleneck in determining heat flux densities when using remote sensing data. Its value is very difficult to determine by means of field measurements. Therefore in this study a constant value for f_{z_0}, valid for the whole area, is used as a fitting factor to minimize the error between SEBI results and field measurements. At three different surfaces in Barrax simultaneous field measurements of heat flux

densities have been obtained: irrigated maize, bare soil and fallow. Figure 7.2 shows the comparison between the values for Λ obtained from field measurements and from SEBI for the three different surface types. Figure 7.2 shows that the results for the SEBI model applied at the TMS-NS001 data set are satisfactory when f_{z_0} is equal to 0.025, which implies $kB^{-1} = 3.69$, where $kB^{-1} = \ln(\frac{z_{0,m}}{z_{0,h}})$. The RMSE for Λ is then equal to 0.04.

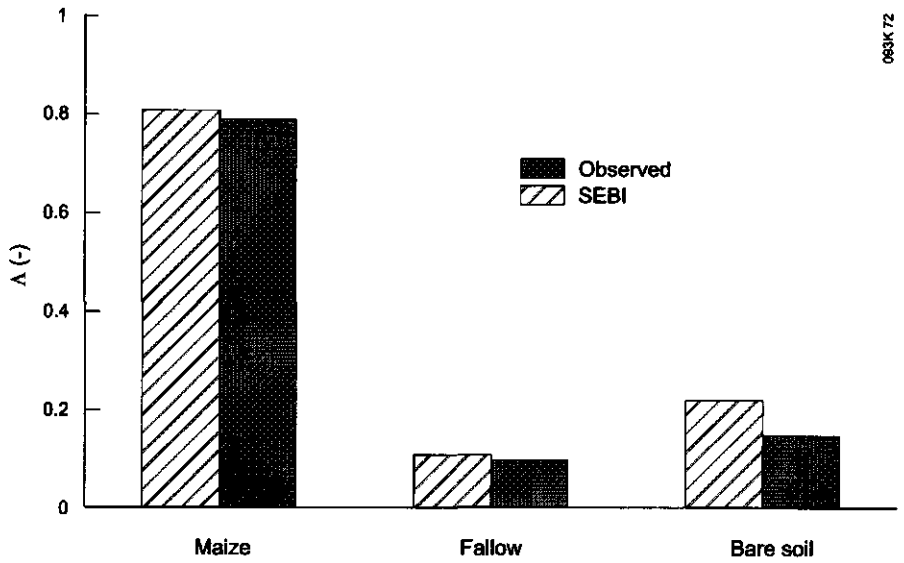

Figure 7.2: Comparison of field measurements of evaporative fraction Λ with SEBI model results for three sites in the Barrax area, June 29, 1991.

The spatially distributed input data used by the SEBI algorithm: r_0, T_0 and $NDVI$ will now be aggregated towards different spatial scales to determine the impact of using low resolution data as input on SEBI results.

7.1.2 Impact of spatial resolution of input data on SEBI results

The following procedure has been set up to study the spatial aggregation of land surface characteristics. First SEBI has been applied using the land surface characteristics r_0, T_0 and $NDVI$ derived from the original data set (geometrical resolution = 18.5 m) as input. The results are discussed in the previous paragraph 7.1.1, and it was shown that SEBI provided a good estimate of the heat flux densities. These results will be used in the remainder of this paragraph as a reference to determine the error due to aggregation. The spatially distributed H and λE have been averaged. From these mean heat flux densities the corresponding Λ is derived. These mean values are denoted in Figure 3.1 (path A) as $\overline{F}$ and will therefore be denoted in the

remainder of the chapter as $\overline{H}$, $\overline{\lambda E}$ and $\overline{\Lambda}$. *The values of* $\overline{H}$, $\overline{\lambda E}$ *and* $\overline{\Lambda}$ *are considered to be the correct aggregated values of* H, λE *and* Λ *for the whole scene.* If the whole Barrax site is considered as a single NWPM grid cell, ($\approx 10 * 10$ km^2) the values of $\overline{H}$, $\overline{\lambda E}$ and $\overline{\Lambda}$ will provide the right input for the NWPM.

Please note that the average of Λ derived directly from the SEBI results, $\langle\Lambda\rangle$, is not equal to $\overline{\Lambda}$. With $\overline{\Lambda}$ the condition of the conservation of energy is fulfilled by averaging the heat flux densities H and λE. While for $\langle\Lambda\rangle$ this is not necessarily true, because of the non-linearity of the function relating Λ to H and λE: $\Lambda = \lambda E/(\lambda E + H)$. If the landscape is heterogeneous then $\overline{\Lambda}$ and $\langle\Lambda\rangle$ will be different.

The spatially distributed input variables r_0, T_0 and $NDVI$ are resampled each time by a factor 2, resulting in input data at resolutions of 37, 74, 148, 296, 592, 1184, 2368, 4736 and 9472 m. This is equivalent to using multispectral radiometric observations at increasingly lower resolutions. The resampling has been done by means of linear averaging. The $NDVI$ is resampled by first resampling the reflectances for the red band and near infrared band, r_R and r_{NIR}, and from those the corresponding $NDVI$ has been calculated. This is equivalent to average multispectral observations band by band, i.e. as done when using low resolution observations. The $NDVI$ is a non-linear function of both r_R and r_{NIR}, therefore to fulfill the condition of the conservation of energy, r_R and r_{NIR} are resampled instead of $NDVI$.

The simple atmospheric correction scheme to derive r_0 described in Chapter 5 is a linear function of the input radiances, therefore r_0 can be resampled by linear averaging. The non-linearity of the function to derive T_0 from the radiance in the thermal infrared is negligible, therefore T_0 is said to be a linear function of the thermal infrared radiance, and linear averaging of T_0 is allowed. According to Becker and Li (1995) the error in temperature estimate due to aggregation is < 2K. The aggregation error which is observed is therefore only due to the non-linearity of the SEBI model and the heterogeneity of the land surface.

For all resolutions mentioned above the SEBI model has then been applied using the resampled input data r_0, T_0, r_R, r_{NIR} resulting in a spatially distributed H, λE, together with the corresponding Λ for each spatial resolution. The results obtained for a pixel with a resolution of 74 m have to be compared with the average results obtained with the square of 4*4 pixels of 18.5 m covering the same area. All these average results are denoted as $F(\overline{\boldsymbol{p}})$ in Figure 3.1 (Path B). Therefore these results will be denoted as $H(\overline{\boldsymbol{p}})$, $\lambda E(\overline{\boldsymbol{p}})$ and $\Lambda(\overline{\boldsymbol{p}})$ in the remainder of the chapter. The input $\boldsymbol{p}$ consists of the averages of r_0, T_0, r_R and r_{NIR} for the different resolutions.

For all resolutions the error due to aggregation for H, λE and Λ can now be calculated as $\Delta_{H,agg} = \overline{H} - H(\overline{\boldsymbol{p}})$, $\Delta_{\lambda E,agg} = \overline{\lambda E} - \lambda E(\overline{\boldsymbol{p}})$ and $\Delta_{\Lambda,agg} = \overline{\Lambda} - \Lambda(\overline{\boldsymbol{p}})$. This will lead to a distribution of errors for the entire area, where

$\overline{H}$, $\overline{\lambda E}$ and $\overline{\Lambda}$ are evaluated for the area covered by a low resolution pixel. The overall aggregation error, valid for the whole Barrax site, i.e. at the grid cell resolution, is given by $\overline{\Delta}_{H,agg} = \overline{H} - \overline{H(\overline{p})}$, $\overline{\Delta}_{\lambda E,agg} = \overline{\lambda E} - \overline{\lambda E(\overline{p})}$ and $\overline{\Delta}_{\Lambda,agg} = \overline{\Lambda} - \overline{\Lambda(\overline{p})}$. Here $\overline{H}$, $\overline{\lambda E}$ and $\overline{\Lambda}$ are evaluated for the whole area (all pixels). In Figure 7.3 the overall aggregation error for Barrax case is given for H, λE and Λ expressed as a relative error. The relative error due to aggregation for a variable x, $\delta_{x,agg}$ (%) is defined as:

$$\delta_{x,agg} = 100 * \frac{|\Delta_{x,agg}|}{\overline{x}} \tag{7.1}$$

In the same manner the overall relative error due to aggregation $\overline{\delta}_{x,agg}$ can be defined using $\overline{\Delta}_{x,agg}$ instead of $\Delta_{x,agg}$.

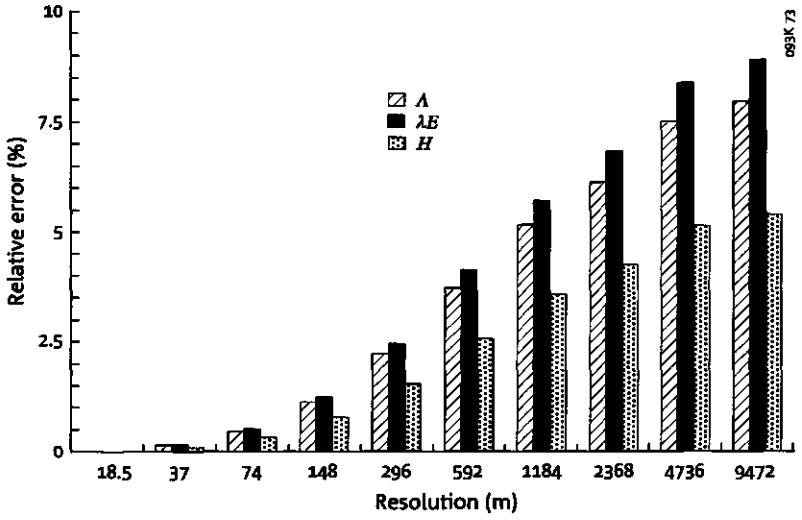

Figure 7.3: The overall relative error due to aggregation for the sensible heat flux density H, latent heat flux density λE and evaporative fraction Λ: $\overline{\delta}_{H,agg}$, $\overline{\delta}_{\lambda E,agg}$ and $\overline{\delta}_{\Lambda,agg}$ respectively for different spatial resolutions of the airborne TMS-NS001 data set obtained in Barrax, June 29, 1991

Figure 7.3 shows that $\overline{\delta}_{H,agg}$, $\overline{\delta}_{\lambda E,agg}$ and $\overline{\delta}_{\Lambda,agg}$ increase with decreasing resolution. At the highest resolutions ($\leq$ 100 m) $\overline{\delta}_{H,agg}$, $\overline{\delta}_{\lambda E,agg}$ and $\overline{\delta}_{\Lambda,agg}$ $\leq$ 1.9 %, while for low resolution data ($\geq$ 5000 m) $\overline{\delta}_{H,agg}$ = 5%, $\overline{\delta}_{\lambda E,agg}$ = 9% and $\overline{\delta}_{\Lambda,agg}$ = 8%. At the resolution of the NOAA-AVHRR satellite (1000 m) $\overline{\delta}_{H,agg}$ = 3.5%, $\overline{\delta}_{\lambda E,agg}$ = 6% and $\overline{\delta}_{\Lambda,agg}$ = 5%. Therefore using low resolution data as input for SEBI would introduce an error in the results, due to the non-linearity of SEBI with regard to the input variables and the heterogeneity of the Barrax site.

However when looking at the distribution of $\delta_{H,agg}$, $\delta_{\lambda E,agg}$ and $\delta_{\Lambda,agg}$ for different low resolution data sets, even low resolution data with a pixel

size twice as large as the high resolution data can introduce large errors. In Figure 7.4 the minimum and maximum $\delta_{\Lambda,agg}$ for different resolutions are given together with $\overline{\delta}_{\Lambda,agg}$. The minimum $\delta_{\Lambda,agg}$ increases with decreasing resolution. At a resolution larger than 2368 m the minimum $\delta_{\Lambda,agg}$ becomes larger than zero, indicating that at this resolution none of the aggregated pixels is completely homogeneous anymore. The maximum $\delta_{\Lambda,agg}$ decreases with decreasing resolution in contrast to $\overline{\delta}_{\Lambda,agg}$. The maximum $\delta_{\Lambda,agg}$ for the high resolution data of 37 m is 95%, indicating that this resolution is larger than the length scale of the process thereby causing (large) errors in the results. The $\delta_{\Lambda,agg}$ obtained for the input data resampled to a 37 m resolution is shown in Figure 7.5 for all pixels.

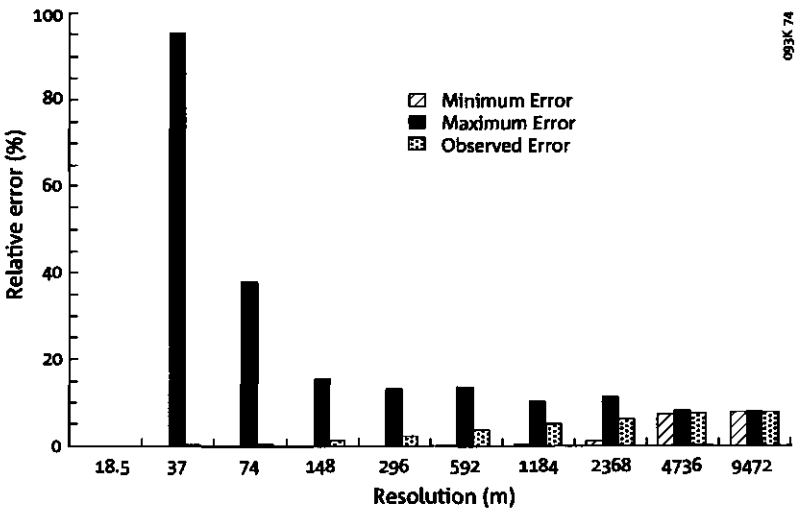

Figure 7.4: The minimum and maximum relative error due to aggregation for the sensible heat flux density H, latent heat flux density λE and evaporative fraction Λ: $\delta_{H,agg}$, $\delta_{\lambda E,agg}$ and $\delta_{\Lambda,agg}$ respectively together with the overall relative error due to aggregation for H, λE and Λ: $\overline{\delta}_{H,agg}$, $\overline{\delta}_{\lambda E,agg}$ and $\overline{\delta}_{\Lambda,agg}$ respectively for different spatial resolutions of the airborne TMS-NS001 data set obtained in Barrax, June 29, 1991

Figure 7.5 shows clearly that for the majority of the pixels $\delta_{\Lambda,agg}$ is zero, causing that $\overline{\delta}_{\Lambda,agg}$ is close to zero (see Figure 7.3). However there are also a number of pixels where $\delta_{\Lambda,agg}$ is not negligible. Figure 7.5 shows that for pixels located at transition zones of non-irrigated and irrigated land the error can be larger than 10% even up to a maximum of 95% (see Figure 7.4). The maximum $\delta_{\Lambda,agg}$ decreases with decreasing resolution while the sharp boundaries are blurred and $\delta_{\Lambda,agg}$ is averaged. This averaging leads however to a larger value for $\overline{\delta}_{\Lambda,agg}$, because a low resolution pixel is covering a larger area and therefore less likely to be completely homogeneous.

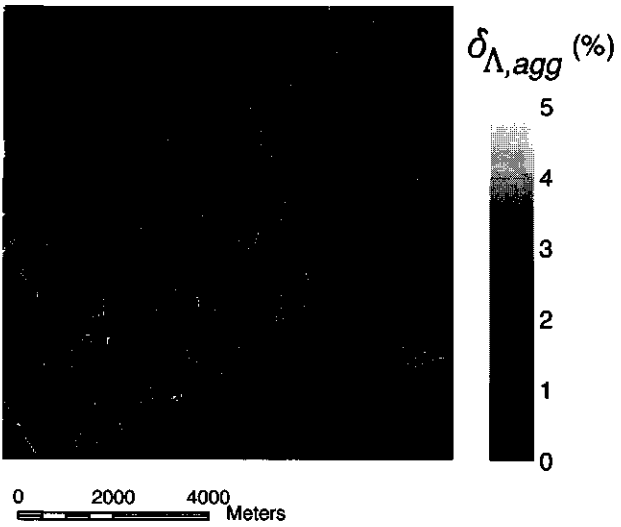

Figure 7.5: A map of the relative error due to aggregation for the evaporative fraction Λ: $\delta_{\Lambda,agg}$ at the resolution of 37 m, Barrax, 29 June 1991

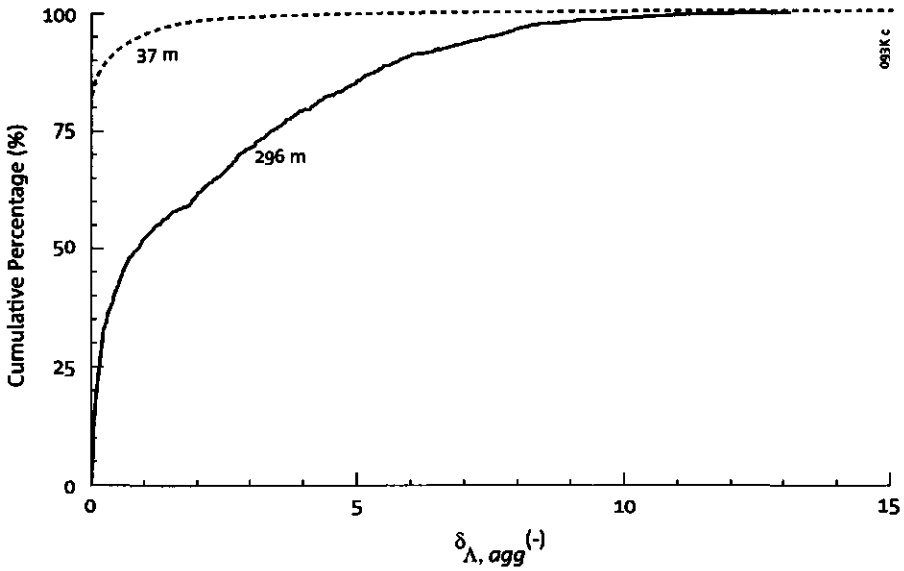

Figure 7.6: Cumulative distribution function of the relative error due to aggregation for the evaporative fraction Λ: $\delta_{\Lambda,agg}$ for 37 m and 296 m resolutions, Barrax, 29 June 1991

The aggregation analysis for the Barrax site shows that for low resolution data with a pixel size twice as large as for the high resolution data, $\delta_{\Lambda,agg}$ can be very high but $\overline{\delta}_{\Lambda,agg}$ is negligible for the whole scene. This is also illustrated by Figure 7.6 which shows the cumulative distribution function for $\delta_{\Lambda,agg}$ for two low resolution observations: 37 and 296 m. The maximum error may be larger for the data with a resolution of 37 m, but the distribution function also shows that for 80% of the data $\delta_{\Lambda,agg} = 0$. For the data with a resolution of 296 m the maximum $\delta_{\Lambda,agg}$ may be smaller, but only 10 % pixels have a $\delta_{\Lambda,agg} = 0$. Whereas the maximum $\delta_{\Lambda,agg}$ for individual pixels decreases with decreasing resolution, $\overline{\delta}_{\Lambda,agg}$ increases. The latter means that *for heterogeneous areas low resolution data cannot be used in a land surface model without compensating for* $\overline{\delta}_{\Lambda,agg}$. The same applies for $\overline{\delta}_{H,agg}$ and $\overline{\delta}_{\lambda E,agg}$.

The objective of this thesis is to look at the possibility of using low resolution remote sensing data for providing input data, e.g. Λ, for NWPMs. In that respect it is useful to look at the values of $\overline{\delta}_{\Lambda,agg}$. A large value of $\overline{\delta}_{\Lambda,agg}$ indicates that low resolution data is not suitable for providing input data for NWPMs. As has been shown in Chapter 4 the cumulative wavelet variance is directly coupled to $\overline{\delta}_{\Lambda,agg}$. On the other hand one should look at the distribution of $\delta_{\Lambda,agg}$ for the different resolutions (see Figure 7.4 - 7.6). These distributions provide a good indication of the reliability of the model results for the separate pixels.

In the case of using SEBI as a tool for predicting the evaporation for separate agricultural fields the priority lies at the correct estimation of the evaporation for each field and not the overall evaporation of the whole region. The results obtained for the Barrax site show that especially for fields bordered by fields with completely different hydrological conditions (wet vs dry) the results should be interpreted very carefully since $\delta_{\Lambda,agg}$ can be large. For these type of applications spatial resolution must be consistent with spatial variability. Also here the wavelet analysis can play a part to predict $\delta_{\Lambda,agg}$, while the pixels in a discrete wavelet transform of an image with the highest wavelet coefficients are subject to a large aggregation error depending on the non-linearity of the model. The above shows also that results obtained by applying SEBI to low resolution data of a heterogeneous area cannot be validated by using field measurements.

In the following paragraphs the two approaches introduced in Chapter 3: linearization approach and convex hull approach, will be used to predict $\overline{\Delta}_{H,agg}$, $\overline{\Delta}_{\lambda E,agg}$ and $\overline{\Delta}_{\Lambda,agg}$ while using low resolution data.

7.1.3 Linearization approach

The values of $\overline{\Delta}_{H,agg}$, $\overline{\Delta}_{\lambda E,agg}$ and $\overline{\Delta}_{\Lambda,agg}$ for different resolutions of the input data can be approximated by linearization of SEBI as explained in Paragraph 3.2. Since SEBI uses 4 spatially distributed input variables: r_0, T_0, r_R and

Table 7.2: Terms in the estimation of the error due to aggregation for the latent heat flux density, λE: $\overline{\Delta}_{\lambda E,agg}$ using Equation 3.7

Term in Equation 3.7	Non-Linearity Term k	Variance Term V
$\frac{1}{A}\int_A (p_1(x,y)-\overline{p}_1)^2 dA \frac{d^2 f}{\partial p_1^2}\Big\vert_p$	$\frac{\partial^2 \lambda E}{\partial r_0^2}$	$\hat{\sigma}^2_{r_0,j}$
$\frac{1}{A}\int_A (p_2(x,y)-\overline{p}_2)^2 dA \frac{d^2 f}{\partial p_1^2}\Big\vert_p$	$\frac{\partial^2 \lambda E}{\partial T_0^2}$	$\hat{\sigma}^2_{T_0,j}$
$\frac{1}{A}\int_A (p_3(x,y)-\overline{p}_3)^2 dA \frac{d^2 f}{\partial p_1^2}\Big\vert_p$	$\frac{\partial^2 \lambda E}{\partial r_R^2}$	$\hat{\sigma}^2_{r_R,j}$
$\frac{1}{A}\int_A (p_4(x,y)-\overline{p}_4)^2 dA \frac{d^2 f}{\partial p_1^2}\Big\vert_p$	$\frac{\partial^2 \lambda E}{\partial r_{NIR}^2}$	$\hat{\sigma}^2_{r_{NIR},j}$
$\frac{1}{A}\int_A (p_1(x,y)-\overline{p}_1)(p_2(x,y)-\overline{p}_2) dA \frac{d^2 f}{\partial p_1 \partial p_2}\Big\vert_p$	$\frac{\partial^2 \lambda E}{\partial r_0 T_0}$	$\hat{\sigma}^2_{r_0 T_0,j}$
$\frac{1}{A}\int_A (p_1(x,y)-\overline{p}_1)(p_3(x,y)-\overline{p}_3) dA \frac{d^2 f}{\partial p_1 \partial p_3}\Big\vert_p$	$\frac{\partial^2 \lambda E}{\partial r_0 r_R}$	$\hat{\sigma}^2_{r_0 r_R,j}$
$\frac{1}{A}\int_A (p_1(x,y)-\overline{p}_1)(p_4(x,y)-\overline{p}_4) dA \frac{d^2 f}{\partial p_1 \partial p_4}\Big\vert_p$	$\frac{\partial^2 \lambda E}{\partial r_0 r_{NIR}}$	$\hat{\sigma}^2_{r_0 r_{NIR},j}$
$\frac{1}{A}\int_A (p_2(x,y)-\overline{p}_2)(p_3(x,y)-\overline{p}_3) dA \frac{d^2 f}{\partial p_2 \partial p_3}\Big\vert_p$	$\frac{\partial^2 \lambda E}{\partial T_0 r_R}$	$\hat{\sigma}^2_{T_0 r_R,j}$
$\frac{1}{A}\int_A (p_2(x,y)-\overline{p}_2)(p_4(x,y)-\overline{p}_4) dA \frac{d^2 f}{\partial p_2 \partial p_4}\Big\vert_p$	$\frac{\partial^2 \lambda E}{\partial T_0 r_{NIR}}$	$\hat{\sigma}^2_{T_0 r_{NIR},j}$
$\frac{1}{A}\int_A (p_3(x,y)-\overline{p}_3)(p_4(x,y)-\overline{p}_4) dA \frac{d^2 f}{\partial p_3 \partial p_4}\Big\vert_p$	$\frac{\partial^2 \lambda E}{\partial r_0 r_{NIR}}$	$\hat{\sigma}^2_{r_R r_{NIR},j}$

r_{NIR}, Equation 3.7 has to be written for $n = 4$ variables. Two important characteristics have to be quantified: the non-linearity of the SEBI model and the heterogeneity of the land surface. The separate terms needed in Equation 3.7 are listed in Table 7.2 in the case of the estimation of $\overline{\Delta}_{\lambda E,agg}$. The terms are separated into two categories, the ones describing the non-linearity of SEBI with regard to r_0, T_0, r_R and r_{NIR}, and the ones describing the heterogeneity of the land surface by means of the wavelet variance, $\hat{\sigma}^2_{f,j}$ and covariance, $\hat{\sigma}^2_{fg,j}$.

The second order derivatives needed by the non-linearity term k have been evaluated numerically using symmetric difference quotients. The only unknown here is p, which gives the values for the input variables r_0, T_0, r_R and r_{NIR} to determine the exact derivatives. The mean values of these variables will not give necessarily the exact result because of neglecting of higher order derivatives with the Taylor expansion. For this data set the above set of derivatives will be calculated using the mean, median and modus values for r_0, T_0, r_R and r_{NIR} as estimates of p. In Table 5.1 the mean, median and modus values are given for r_0 , T_0 and the $NDVI$.

The variance term V is given by the results of the wavelet analysis.

In Chapter 4 it was shown that the cumulative wavelet variance $\hat{\sigma}^2_{f,j}$ and cumulative wavelet covariance $\hat{\sigma}^2_{fg,j}$ while using the Haar wavelet, represent the variance term V in Equation 3.7. The results of the length scale analysis discussed in Chapter 6 will be used, for $\hat{\sigma}^2_{f,j}$ see Figure 6.1. In Figure 7.7 $\hat{\sigma}^2_{fg,j}$ for the four input variables r_0, T_0, r_R and r_{NIR} is given.

Figure 7.7 shows that for all possible combinations of the input variables r_0, T_0, r_R and r_{NIR}, $\hat{\sigma}^2_{fg,j}$ shows the same trend present in the curves of $\hat{\sigma}^2_{f,j}$ presented in Chapter 6 (see Figure 6.1) except for $\hat{\sigma}^2_{T_0 r_{NIR},j}$. At small length scales there seems to be not much correlation between T_0 and r_{NIR}.

The information given by $\hat{\sigma}^2_{f,j}$ and $\hat{\sigma}^2_{fg,j}$ together with the numerical derivatives is used to estimate $\Delta_{\lambda E,agg}$ and $\Delta_{H,agg}$. Figure 7.8 shows the results for $\overline{\Delta}_{\Lambda,agg}$. Note that the results for $\overline{\Delta}_{\Lambda,agg}$ were derived indirectly from the results obtained for $\overline{\Delta}_{H,agg}$ and $\overline{\Delta}_{\lambda E,agg}$. The derivatives were derived with mean, median and modus values for r_0, T_0, r_R and r_{NIR}.

Figure 7.8 shows that the $\overline{\Delta}_{\Lambda,agg}$ obtained when using either the mean and median values for r_0, T_0, r_R and r_{NIR} slightly underestimate the actual $\overline{\Delta}_{\Lambda,agg}$. But the shape of the estimated curve using the mean and median input values is similar to the shape of the curve of the observed $\overline{\Delta}_{\Lambda,agg}$. Only the curve estimated with the modus of the input variables is clearly off in predicting a $\overline{\Delta}_{\Lambda,agg}$ close to 0. The modus of the input variables is only representative for the dry pixels. The shape is determined by the results of the wavelet analysis while the non-linearity term k, determined by the non-linearity of the SEBI model, is constant for all resolutions.

The results which have been obtained show clearly that the wavelet variance is a good tool to assess at which scales $\overline{\Delta}_{\Lambda,agg}$ would be large. The dominant length scale, ℓ^*_{dom} is the length scale at which the largest increase in $\Delta_{\Lambda,agg}$ takes place. This is only true when the Haar wavelet is used in the wavelet analysis. Only the exact estimation of $\overline{\Delta}_{\Lambda,agg}$ will remain troublesome due to the a priori unknown value p in Equation 3.7. In the Barrax test case both the mean and median values for where good estimates of p. *The mean and median values of p will also be used in the aggregation analysis for the data sets of Jornada and the Netherlands.*

The linearization approach can also be used to determine which of the input variables contributes most to $\overline{\Delta}_{\lambda E,agg}$. Therefore the value of each term listed in Table 7.2 is presented in Figure 7.9 for the resolution of 9472 m, i.e. the largest possible pixel size where $\overline{\Delta}_{\lambda E,agg}$ is the largest.

Figure 7.9 shows that the r_R term and the T_0 -r_R term are the dominant factors in estimating $\overline{\Delta}_{\lambda E,agg}$. The contribution of the r_R term to $\overline{\Delta}_{\lambda E,agg}$ differs when using the median value for the input variables, this would indicate that the non-linearity of λE with regard to r_R is the most important factor, together with a high spatial variability of r_R. Looking at the contribution of the T_0 ,r_R term to $\overline{\Delta}_{\lambda E,agg}$ the lower value estimated on the basis of the modus input stands out. Also this indicates that the non-linearity

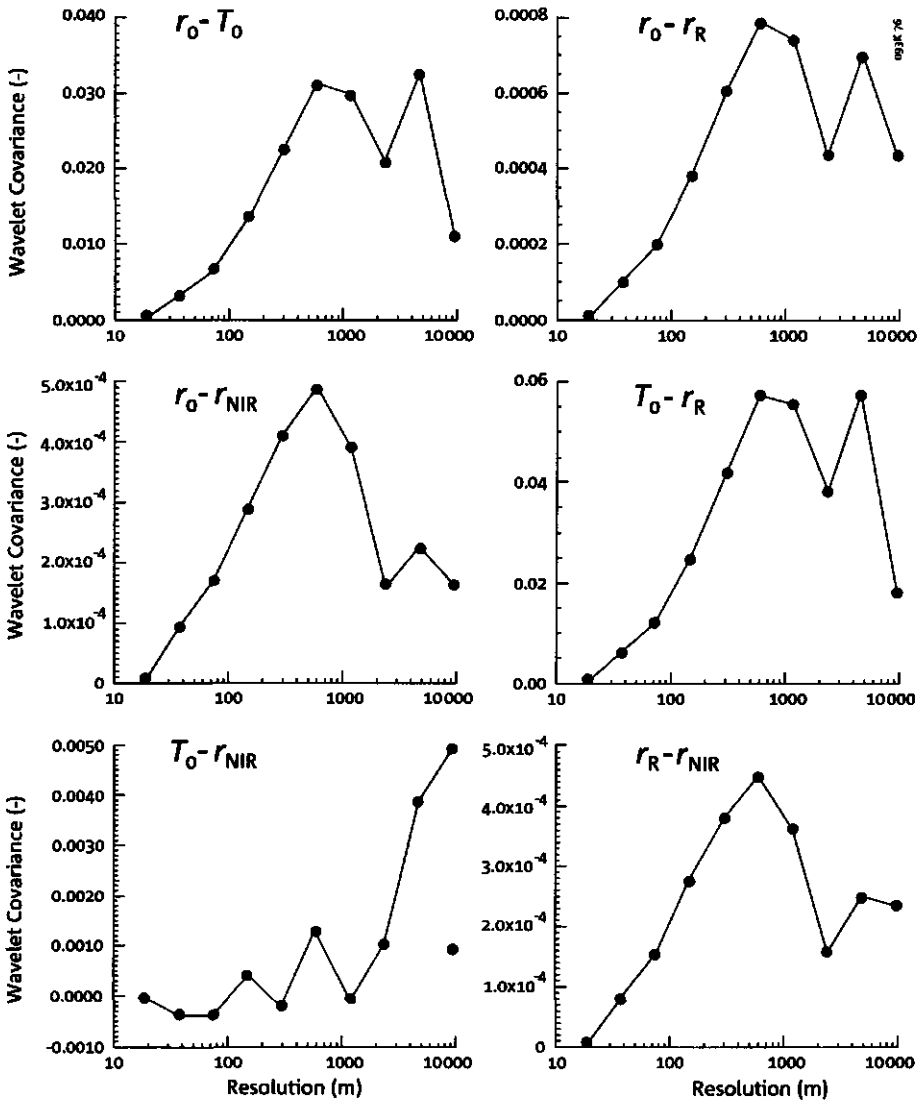

Figure 7.7: All possible combinations of the wavelet covariance $\hat{\sigma}^2_{fg,j}$ for surface albedo r_0, surface temperature T_0, red reflectance r_R and near infrared reflectance r_{NIR}. The graphs are based on airborne TMS-NS001 data obtained at Barrax, June 29, 1991. Please note the different scales at the y-axis representing $\hat{\sigma}_{fg,j}$.

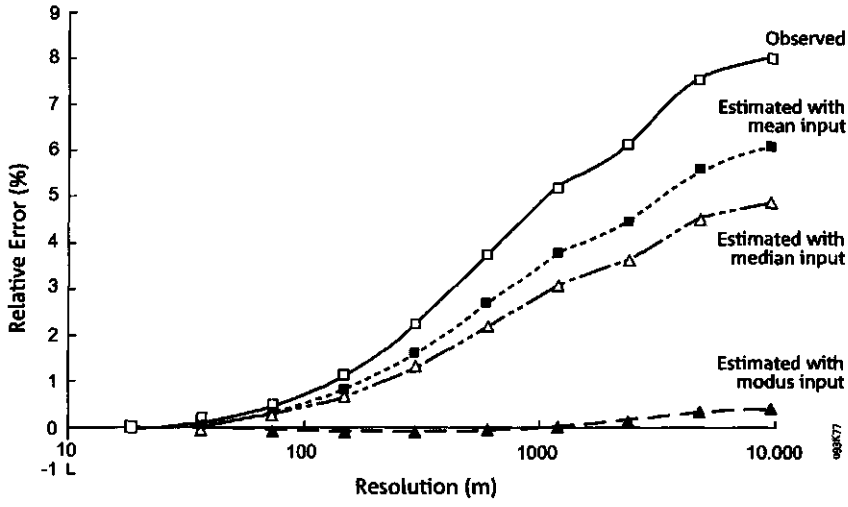

Figure 7.8: Results for the estimation of the error due to aggregation of evaporative fraction, Λ: $\overline{\Delta}_{\Lambda,agg}$, Barrax, June 29, 1991

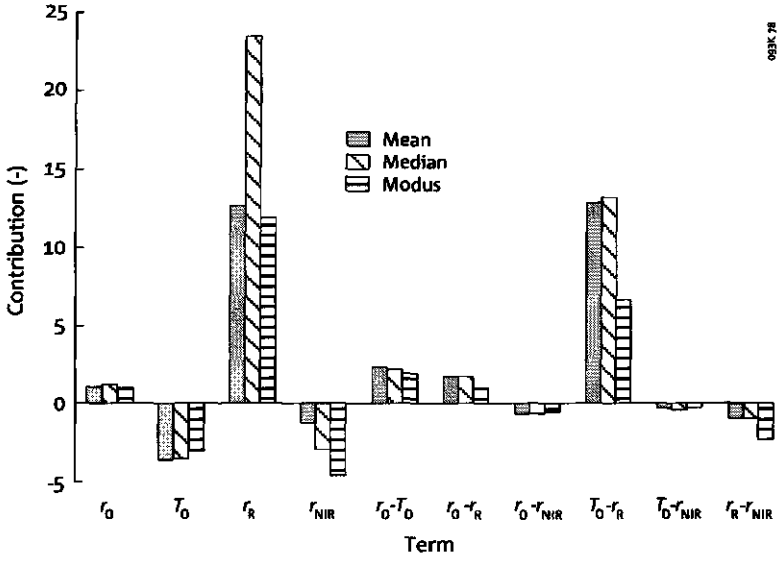

Figure 7.9: Contribution of the different terms defined in Table 7.2 to the overall error due to aggregation for latent heat flux density, λE: $\overline{\Delta}_{\lambda E,agg}$ at the resolution of 9472 m, Barrax, June 29, 1991

of λE with regard to r_R and T_0 is the dominant factor. The covariance terms have a substantial contribution to $\overline{\Delta}_{\lambda E,agg}$. Therefore the correlation between the input variables should always be taken into account when estimating $\overline{\Delta}_{\lambda E,agg}$. The contribution of r_{NIR} and r_0 to $\overline{\Delta}_{\lambda E,agg}$ is relatively small compared to the contribution of r_R and T_0.

Low resolution data, like METEOSAT and NOAA observe locations more than once per day and are therefore very well suited to map Λ on a daily basis for large areas. However the price to pay compared to high resolution data is $\overline{\Delta}_{\Lambda,agg}$. *The question remains how to correct the results obtained by low resolution data for* $\overline{\Delta}_{\lambda E,agg}$, $\overline{\Delta}_{H,agg}$ *and* $\overline{\Delta}_{\Lambda,agg}$*?*

The linearization approach can be used to correct the results obtained by low resolution data for $\overline{\Delta}_{\Lambda,agg}$ in the following way. First for a few selected moments throughout the year high resolution data of (a part of) the area under consideration should be available. A good criteria would be before and after dates when major changes in land use would occur, e.g. harvesting of grown crops. These high resolution data will be used for obtaining $\hat{\sigma}^2_{f,j}$ and $\hat{\sigma}^2_{fg,j}$ of the land surface characteristics used in SEBI: r_0, T_0 and $NDVI$ (r_R and r_{NIR}). The Haar wavelet will be used in the wavelet analysis. Then for selected moments in time the factor V in Equation 3.7 is known. The low resolution data itself can be used as an estimation of p in determining the derivatives of the input data with lead to H and λE, this will give a pixel-wise value for the factor k in equation 3.7. As is shown the mean and median value of the input variables, i.e. low resolution data, can provide only an estimate of k, but will still limit $\overline{\Delta}_{\Lambda,agg}$.

Using equation 3.7 the results of SEBI for H and λE can now be corrected for aggregation errors, as $\overline{\Delta}_{\lambda E,agg}$ and $\overline{\Delta}_{H,agg}$ is known for each pixel at different low resolution up to the grid cell resolution. The corrected values for $\overline{H}$ and $\overline{\lambda E}$ can be used to derive $\overline{\Lambda}$. This approach does not claim to provide the correct $\overline{\Lambda}$ but will produce a better result then without any correction.

7.1.4 Convex hull approach

With the convex hull approach described in Paragraph 3.3 it is possible to determine the boundary of $\overline{H}$, $\overline{\lambda E}$ and $\overline{\Lambda}$ for a given resolution, based on the spatial variability of the input variables. The boundaries are given by $F_\vee$ and $F^\wedge$, where F here is calculated using SEBI. Crucial in the success of the convex hull approach is the determination of the spatial variability of the input data. The spatial variability of the input data determines together with the non-linearity of the model the variability in model results, and therefore the range of $\overline{H}$, $\overline{\lambda E}$ and $\overline{\Lambda}$ for a given low resolution measurement of r_0, T_0, r_R and r_{NIR}.

To illustrate the convex hull concept the upper and lower boundaries of the $NDVI$ for the mean input of r_R and r_{NIR} derived from the TMS-

NS001 data obtained at the Barrax site, 29 june 1991 will be presented. The $NDVI$ is a non linear function of r_R and r_{NIR}. Therefore an error due to aggregation will occur when r_R and r_{NIR} are mapped over a heterogeneous area. In Figure 7.10 the $NDVI$ is plotted as a function of r_R and r_{NIR}. The limits of the $NDVI$ results are given by the spatial variability of r_R and r_{NIR} in the Barrax area. The spatial variability is given by the high resolution data. The total amount of possible spatial variability within a low resolution pixel is given by the convex hull which envelopes the pixel values of r_R and r_{NIR}. For the area determined by this convex hull the $NDVI$ has been calculated.

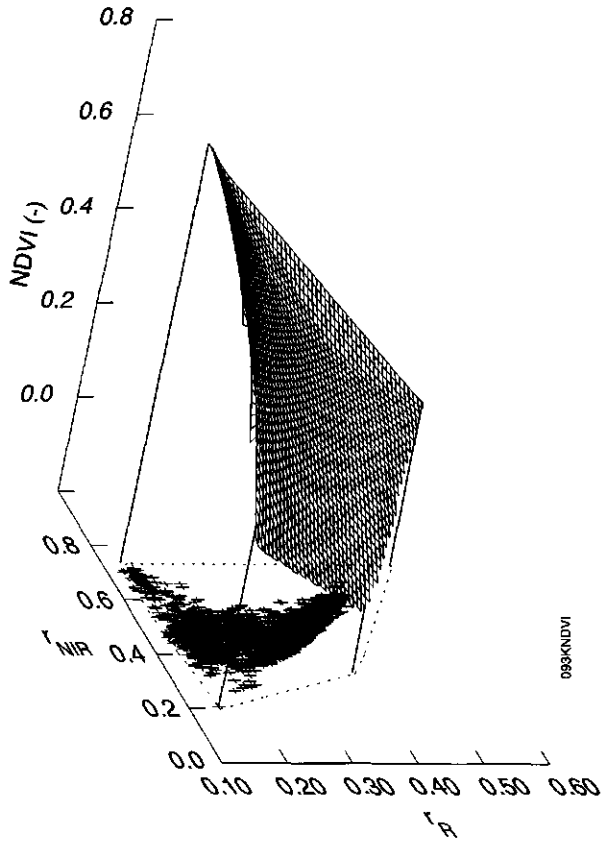

Figure 7.10: $NDVI$ as function of r_R and r_{NIR}. In the r_R-r_{NIR} plane the convex hull indicating the spatial variability is given together with 1 % of the data points.

The NDVI curve can now also be enveloped by a convex hull. This convex hull limits all possible results for the $NDVI$ given the spatial variability of r_R and r_{NIR} within the Barrax area. The upper hull represents the maximum

NDVI value given a low resolution measurement of any r_R and r_{NIR}, in the same manner the lower hull represents the minimum NDVI value given any low resolution measurement of r_R and r_{NIR}. If the upper and lower convex hull are subtracted the resulting plane gives the estimated $\Delta_{NDVI}(r_R, r_{NIR})$ for all combinations of r_R and r_{NIR}. Figure 7.11 shows the results for the Barrax test case. The convex hull approach can also be applied for the SEBI algorithm, only here SEBI depends on 4 input parameters, therefore the convex hull has to be solved for 5 dimensions: the 4 input parameters, together with the result of SEBI, either H, λE or Λ.

For the Barrax site three numerical simulation experiments will be evaluated to estimate the spatial variability of the input data:

1. The high resolution data set (resolution = 18.5 m) will be used to infer the spatial variability of the land surface characteristics used as input data in SEBI: r_0, T_0, r_R and r_{NIR}. The results based on this option will be compared with $\overline{H}$, $\overline{\lambda E}$ and $\overline{\Lambda}$ obtained for the Barrax data set. According to the convex hull theory the values for $\overline{H}$, $\overline{\lambda E}$ and $\overline{\Lambda}$ should lie between the boundaries derived by the convex hull approach. The results obtained by this option will be seen as the truth to which the other two options are compared.

2. Only 1% of the pixels of the original data set will be used to get information on the spatial variability of the land surface characteristics. This is similar to the situation where for a part of the region covered by a low resolution data set some high resolution data is available. Also nowadays there are sensors which are capable of measuring either in high-resolution or low-resolution mode (e.g. FOCUS, a sensor developed by DLR, Germany for the detection of biomass burning).

3. The input data will be resampled to the resolution of 1184 m, comparable to the resolution of the NOAA-AVHRR sensor. The spatial variability of the land surface characteristics used as input in SEBI will be determined for this low resolution data set. The minimum and maximum values obtained for $\overline{H}$, $\overline{\lambda E}$ and $\overline{\Lambda}$ will be compared with those obtained by the other two options.

The SEBI model was run for all possible combinations of r_0, T_0, r_R and r_{NIR} which are contained within boundaries given by the convex hull, resulting in a large number of values for H, λE and Λ. This has been done for all three options mentioned above. The 5-dimensional convex hull encompassing the input data together with the results, either H, λE or Λ, has been derived. The minimum and maximum values for $\overline{H}$, $\overline{\lambda E}$ and $\overline{\Lambda}$ has been calculated by finding the values for $F_\vee$ and $F^\wedge$ for the mean values of the input variables r_0, T_0, r_R and r_{NIR}. As an estimation of the actual value

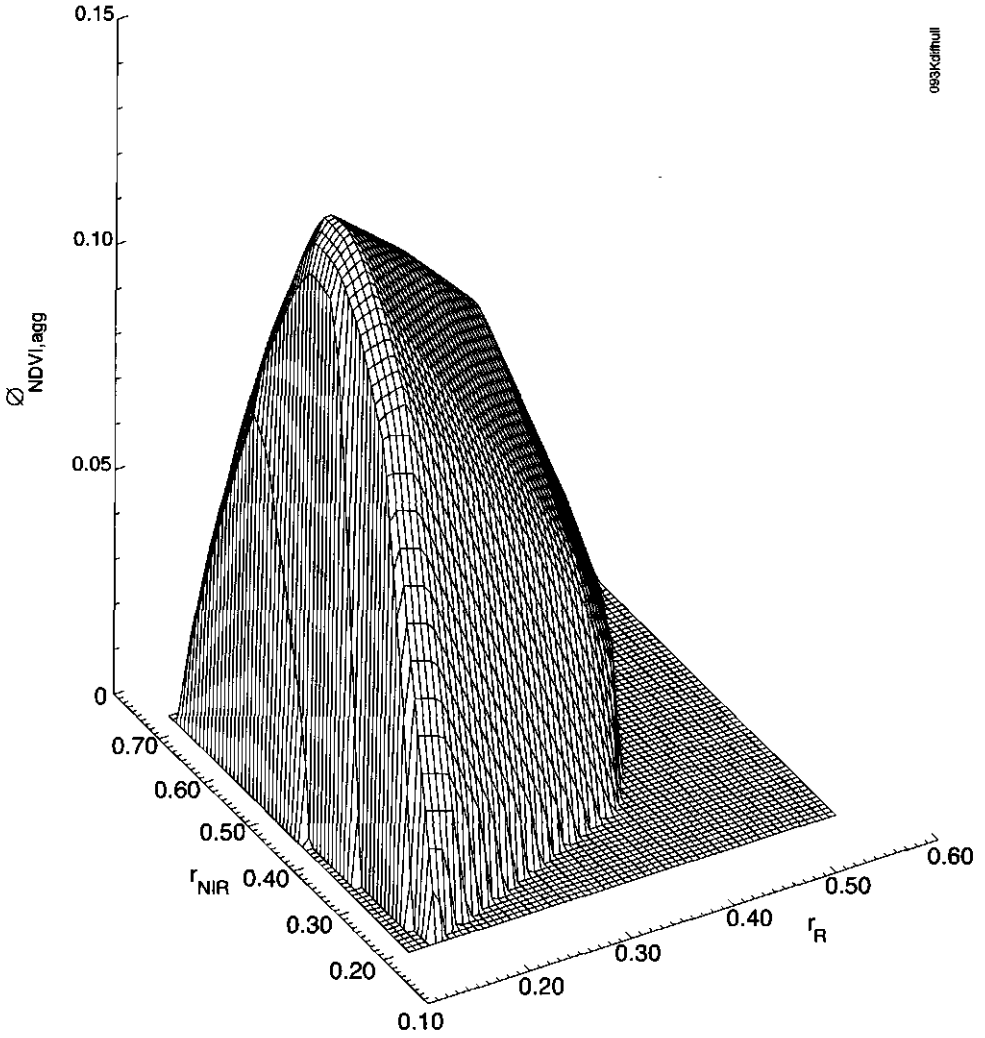

Figure 7.11: The maximum error due to aggregation for the $NDVI$, $\Delta_{NDVI}(r_R, r_{NIR}$, based on airborne TMS-NS001 derived reflectances in the red and near-infrared, r_R and r_{NIR} respectively, Barrax, 29 June 1991

of $\overline{H}$, the value of $\overline{H}_{est}$ obtained by the convex hull has been taken:

$$\overline{H}_{est} = \frac{\overline{H}_{max} - \overline{H}_{min}}{2} \tag{7.2}$$

The same assumption has been made by determining $\overline{\lambda E}_{est}$ whereas $\overline{\Lambda}_{est}$ is estimated using $\overline{\lambda E}_{est}$ and $\overline{H}_{est}$. Table 7.3 summarizes the results for the convex hull analysis for the Barrax data set.

Table 7.3 shows that the assumption given by Equation 7.2 does not produce the right values for $\overline{H}$, $\overline{\lambda E}$ and $\overline{\Lambda}$ for the full data set. $\overline{H}$ is underestimated (216.4 < 243.9) while $\overline{\lambda E}$ is overestimated (215.8 > 197.9), leading to an overestimation of $\overline{\Lambda}$ (0.499 > 0.410). The other options produce better results in estimating $\overline{\Lambda}$ but this is not more than a coincidence and no conclusions can be drawn from that. Looking at the minimum and maximum values of $\overline{H}$ (155.9-276.9), $\overline{\lambda E}$ (162.7-268.8) and $\overline{\Lambda}$ (0.322-0.542) obtained for the full data set it can be seen that the range for the possible values of $\overline{\Lambda}$ is 0.12, for $\overline{\lambda E}$ is 104.1 W m^{-2} and for $\overline{H}$ is 121.0 W m^{-2}. The results for $\overline{\lambda E}$ and $\overline{H}$ show that the maximum error due to aggregation can be large, up to a value of 44% for $\delta_{\lambda E,agg}$ and 36% for $\delta_{H,agg}$.

If only 1% of the pixels is taken to infer the spatial variability a good estimate of the minimum and maximum value for $\overline{\lambda E}$ can be given. However the minimum value of $\overline{H}$ is overestimated, leading also to an underestimation of the maximum value of $\overline{\Lambda}$. But still *a small portion of the dataset, if sampled at a high resolution, gives a reasonable estimate of the variability for the possible values of* $\overline{\lambda E}$, $\overline{H}$ *and* $\overline{\Lambda}$. Only by using low resolution imagery erroneous values for the minimum and maximum values for $\overline{H}$, $\overline{\lambda E}$ and $\overline{\Lambda}$ can be generated. *Therefore in combination with low resolution data always high resolution imagery should be used to infer the domains of the spatial variability of the input variables.*

In the following two paragraphs the above approaches to estimate $\overline{\Delta}_{\lambda E,agg}$, $\overline{\Delta}_{H,agg}$ and $\overline{\Delta}_{\Lambda,agg}$ will be applied to the remaining two data sets: Jornada Experimental Range and the Netherlands.

7.2 Case study Jornada Experimental Range

The input variables H, λE and Λ for the SEBI model have been derived using DAEDALUS data obtained at 19 June 1997 at the Jornada Experimental Range. The resolution of the data is 4 m. Field measurements and radio soundings have been used to derive the remaining input data, valid for the whole Jornada Experimental Range. In Table 7.4 these data are summarized.

In contrast to the Barrax test case the SEBI model will not be applied for all pixels within the entire Jornada Experimental range. Instead the $\overline{\Delta}_{\lambda E,agg}$, $\overline{\Delta}_{H,agg}$ and $\overline{\Delta}_{\Lambda,agg}$ will be calculated using the two approaches mentioned above: the linearization approach and the convex hull approach.

Table 7.3: Results for the convex hull analysis for the SEBI results for the evaporative fraction Λ, latent heat flux density λE and sensible heat flux density H based on TMS-NS001 data of the Barrax area., June 29, 1991. The spatial variability of the input variables, surface albedo r_0, surface albedo T_0, reflectance in the red r_R and reflectance in the near-infrared r_{NIR} was derived by either using the full high resolution data set, 1% of the high resolution data set, or the resampled high resolution data set to the size of a NOAA pixel.

SEBI results	High resolution data set	1 % of data set	Simulated NOAA
$\overline{\Lambda}$ (-)	0.410		
$\overline{\Lambda}_{est}$ (-)	0.499	0.476	0.395
$\overline{\Lambda}_{min}$ (-)	0.322	0.322	0.387
$\overline{\Lambda}_{max}$ (-)	0.542	0.461	0.415
$\overline{\delta}_{\Lambda,agg}$ min (%)	21.2	21.2	5.6
$\overline{\delta}_{\Lambda,agg}$ max (%)	32.2	12.4	1.1
$\overline{\lambda E}$ W m^{-2}	197.9		
$\overline{\lambda E}_{est}$ W m^{-2}	215.8	217.4	170.5
$\overline{\lambda E}_{min}$ W m^{-2}	162.7	166.9	168.1
$\overline{\lambda E}_{max}$ W m^{-2}	268.8	267.9	172.9
$\overline{\delta}_{\lambda E,agg}$ min (%)	17.8	15.7	15.1
$\overline{\delta}_{\lambda E,agg}$ max (%)	44.9	35.3	12.6
$\overline{H}$ W m^{-2}	243.9		
$\overline{H}_{est}$ W m^{-2}	216.4	239.7	260.8
$\overline{H}_{min}$ min W m^{-2}	155.9	208.9	253.8
$\overline{H}_{max}$ max W m^{-2}	276.9	270.4	267.8
$\overline{\Delta}_{H,agg}$ min (%)	36.1	14.4	4.0
$\overline{\Delta}_{H,agg}$ max (%)	13.5	10.8	9.8

Table 7.4: Areally constant input variables for the SEBI model, Jornada Experimental range, 19 June 1997.

Input variable	Value	Source
h_i	1700 m	Radio Sounding
θ_h	317.0 K	Radio Sounding
p_h	70000 Pa	Radio Sounding
q_h	0.0032 kg kg^{-1}	Radio Sounding
p_s	82646 Pa	Field Measurement
u^*	1.0 m s^{-1}	Field Measurement
f_{z_0}	0.1	-
$K^{\downarrow}$	850 W m^{-2}	Field Measurement
$L^{\downarrow}$	497 W m^{-2}	Field Measurement

7.2.1 Linearization approach

Also for the Jornada test case, as with the Barrax test case, equation 3.7 adapted for $n = 4$ variables will be used to estimate $\overline{\Delta}_{\lambda E,agg}$, $\overline{\Delta}_{H,agg}$ and $\overline{\Delta}_{\Lambda,agg}$. In Figure 7.12 the results for the estimation of $\overline{\Delta}_{\Lambda,agg}$ are shown. As input value for the non-linearity term the mean value of the input parameters r_0, T_0, r_R and r_{NIR} has been chosen . The median and modus value of the input parameters showed almost similar results.

Figure 7.12 shows that $\overline{\Delta}_{\Lambda,agg}$ is almost negligible. Even for a resolution $\geq$ 1000 m $\overline{\Delta}_{\Lambda,agg} \approx -0.01$. In the case of the Jornada Experimental Range low resolution data can be used to predict $\overline{\Lambda}$ with almost no error due to aggregation. The three different curves for grass, mesquite and transition are different however. For the mesquite site the largest differences occur at the smallest length scales which are equal to the size of the dunes and the bare soil areas. If the resolution becomes larger than the dunes and bare soil areas, the mesquite curve becomes almost flat, indicating that almost no variability is present at the largest length scales ($\geq$ 100 m). The grass site shows that whenever the resolution increases with a factor two, $\overline{\Delta}_{\Lambda,agg}$ becomes twice as large. This indicates that the variability is evenly spread between the different length scales. The transition site is a combination between the two other curves. When the resolution $\leq$ 32 m it follows the trend of the mesquite site due to the presence of mesquite dunes, at a resolution $\geq$ 128 m it follows the trend of the grass site. Although the sites at the Jornada experimental range at length scales $\leq$ 4 m exhibit a large spatial variability , the sites looks rather homogeneous at larger length scales. Also there is not a large variability in hydrological conditions within the Jornada experimental range in the summer. For these type of conditions, i.e. desert vegetation in the summer, low resolution data can be used without introducing an error due to aggregation.

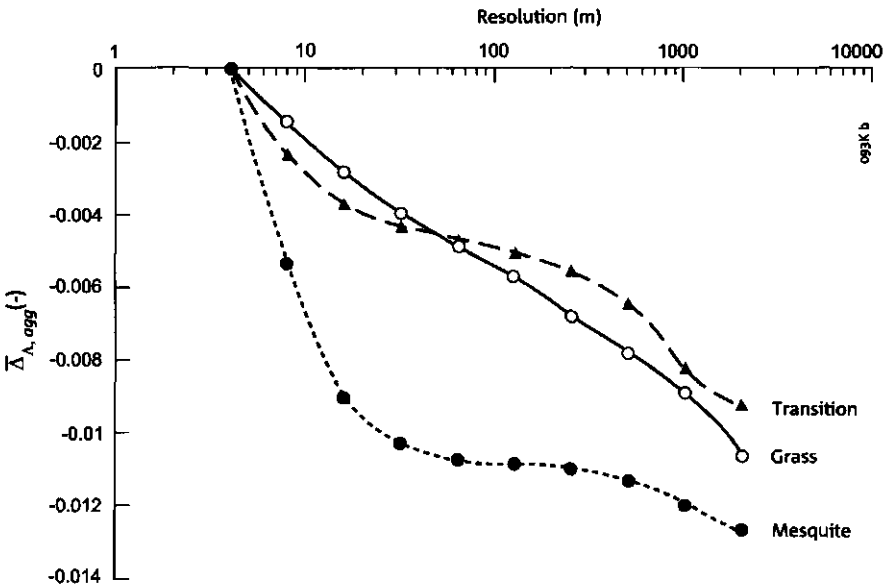

Figure 7.12: Estimation of the overall error due to aggregation for the evaporative fraction, Λ: $\overline{\Delta}_{\Lambda,agg}$ using the linearization approach for the Jornada Experimental Range for the three different experimental sites: grass, transition and mesquite, 19 June 1997. For p in Equation 3.7 the mean value of the input parameters r_0, T_0, r_R and r_{NIR} has been chosen

Table 7.5: Results for the convex hull analysis for the SEBI results for the evaporative fraction Λ, latent heat flux density λE and sensible heat flux density H based on the Daedalus data set of three sites at the Jornada Experimental Range, June 19, 1997. The spatial variability of the input variables, surface albedo r_0, surface albedo T_0, reflectance in the red r_R and reflectance in the near-infrared r_{NIR} was derived by either using the full high resolution data set or 1% of the high resolution data set

SEBI results	Grass		Mesquite		Transition	
	High resolution data set	1 % of data set	High resolution data set	1 % of data set	High resolution data set	1 % of data set
$\overline{\Lambda}_{est}$ (-)	0.185	0.186	0.315	0.330	0.214	0.277
$\overline{\Lambda}_{min}$ (-)	0.137	0.149	0.244	0.279	0.142	0.249
$\overline{\Lambda}_{max}$ (-)	0.233	0.222	0.386	0.380	0.286	0.304
range (-)	0.096	0.073	0.142	0.101	0.144	0.055
$\overline{\lambda E}_{est}$ W m^{-2}	99.1	99.5	174.1	169.0	138.8	138.1
$\overline{\lambda E}_{min}$ W m^{-2}	82.0	91.2	160.8	157.9	124.3	132.6
$\overline{\lambda E}_{max}$ W m^{-2}	116.1	107.8	187.4	180.0	153.2	143.7
range W m^{-2}	34.1	16.6	26.6	22.1	28.9	11.1
$\overline{H}_{est}$ W m^{-2}	368.2	369.6	289.4	292.2	329.4	328.9
$\overline{H}_{min}$ W m^{-2}	355.3	361.9	278.4	283.3	318.7	324.2
$\overline{H}_{max}$ W m^{-2}	381.1	377.2	300.4	301.1	340	333.5
range W m^{-2}	25.8	15.3	22.0	17.8	21.3	9.3

7.2.2 Convex hull approach

For the convex hull approach a similar procedure as with the Barrax data has been followed. Different options to capture the amount of spatial variability have been tested. The difference with Barrax is that here only the first two options have been taken: the degree of spatial variability derived on the basis of the full data set, and the degree of spatial variability derived on the basis of 1% of the data set. The third option in which the input data would have been resampled to the size of a NOAA pixel has been omitted, since the extent of the three sites is only 2048 * 2048 m^2 which is equal to the area covered by 4 NOAA pixels. In Table 7.5 the results of the convex hull analysis are summarized.

Table 7.5 shows the same lack of spatial variability obtained with the

linearization approach. Compared with the results obtained for the Barrax test case with the convex hull approach, the range to which the solution of $\overline{H}$, $\overline{\lambda E}$ and $\overline{\Lambda}$ is confined is much smaller. A remarkable feature is shown when comparing the grass and mesquite site. Whereas for the grass site using only 1% of the data set gives some differences in the estimation of the minimum and maximum values of $\overline{H}$, $\overline{\lambda E}$ and $\overline{\Lambda}$, for the mesquite site these differences are much smaller. This can be explained by the regular pattern exhibited at the mesquite site. A random uniform distributed sampling will still capture almost all spatial variability present at that site.

Based on the results of both the linearization and convex hull approach *it is allowed to use low resolution remote sensing data to obtain estimates of $\overline{H}$, $\overline{\lambda E}$ and $\overline{\Lambda}$. This applies to the summer conditions when the hydrological contrast between plants and bare soil is very small.* More research is needed for those situations where more hydrological contrast is expected, most notably at the end of the raining season.

7.3 Case study The Netherlands

As with the Jornada Experimental Range the same procedure is applied to the Netherlands case study to estimate $\overline{H}$, $\overline{\lambda E}$ and $\overline{\Lambda}$ based on the linearization and the convex hull approach (instead of applying SEBI for all resolutions like the Barrax test case). The input variables r_0, T_0, r_R, r_{NIR} have been estimated using Landsat TM data, 24 May 1995. It has been chosen to examine this date instead only of all dates. As was shown in Chapter 6 the wavelet variance curves are equally shaped for all dates, where the main difference lies in the amount of variability present in the image. For the 24 May 1995 the amount of variability is the largest, together with the 12 August 1995 image. Therefore an analysis of the 24 May 1995 will also provide insight for the other three dates. In Table 7.6 the remaining input variables for the SEBI model are given.

7.3.1 Linearization approach

The length scale analysis discussed in Chapter 6 was applied for 20 equally sized grids in which the Landsat TM image had been subdivided. The same grids will be used for the linearization approach as well as the convex hull approach.

In Figure 7.13 the results for the estimation of $\overline{\Delta}_{\Lambda,agg}$ are given, where $\overline{\Delta}_{\Lambda,agg}$ has been derived using the results for $\overline{\Delta}_{\lambda E,agg}$ and $\overline{\Delta}_{H,agg}$. Grid number 5 has been excluded from the analysis because of the presence of clouds within the grid. Cloud contaminated low resolution pixels are a possible source of error in land surface models using r_0 and T_0 as input variables. The value of r_0 will be overestimated, whereas T_0 will be overestimated.

Table 7.6: Areally constant input variables for SEBI, the Netherlands, 24 May 1995.

Input variable	Value	Source
h_i	1500 m	Radio Sounding
θ_h	295.0 K	Radio Sounding
p_h	85000 Pa	Radio Sounding
q_h	0.007 kg kg^{-1}	Radio Sounding
p_s	100800 Pa	Field Measurement
u^*	0.4 m s^{-1}	Field Measurement
f_{z_0}	0.1	-
$K^{\downarrow}$	785 W m^{-2}	Field Measurement
$L^{\downarrow}$	338 W m^{-2}	Field Measurement

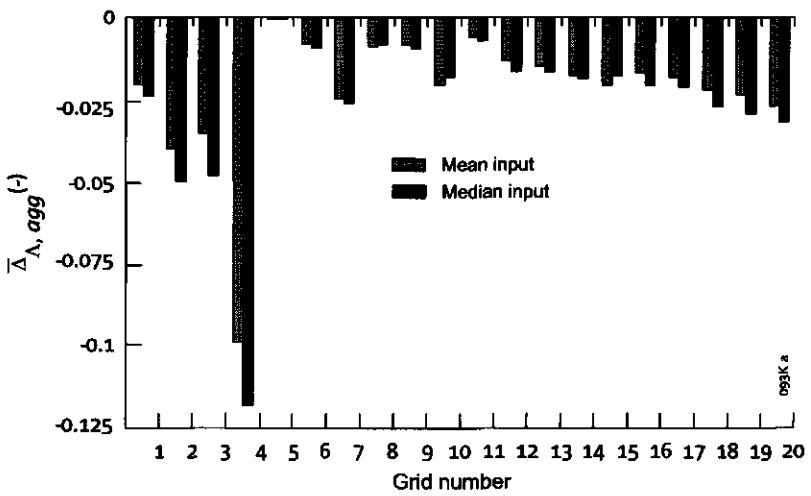

Figure 7.13: Estimation of the overall error due to aggregation for the evaporative fraction, Λ: $\overline{\Delta}_{\Lambda,agg}$ for the 20 grids shown in Plate E using the linearization approach, the Central Part of the Netherlands, May 24, 1995 . For p the mean value or the median value of the input variables r_0, T_0, r_R and r_{NIR} has been chosen

The results shown in Figure 7.13 indicate that for the input variables r_0, T_0, r_R and r_{NIR} the estimations on the basis of the median and mean values do not differ much. They show the same trend for all 20 grids. The grid numbers 2, 3 and 4 show the largest values for $\overline{\Delta}_{\Lambda,agg}$. This can be explained by the presence of large bodies of water in all three grids, which increases the spatial variability for the four input variables, leading to a larger value of $\overline{\Delta}_{\Lambda,agg}$. The mean value of $\overline{\Delta}_{\Lambda,agg}$ for all 20 grids is -0.02 (mean input) and -0.03 (median input) which implies an almost negligible value of $\overline{\Delta}_{\Lambda,agg}$. The maximum value of $\overline{\Delta}_{\Lambda,agg}$ is -0.10 (mean input) and -0.12 (median input). Looking at the grids 3, 8 and 11 which were also highlighted in the length scale analysis described in Chapter 6, one can see large differences between the three grids. For grid 11 the value of $\overline{\Delta}_{\Lambda,agg}$ is close to zero. Grid 3 is then almost covered by the same type of land use, pastures, and exhibits almost no spatial variability. Grid 8 shows only a slightly larger value for $\overline{\Delta}_{\Lambda,agg}$ which is surprising because of the much larger amount of spatial variability. Grid 3 shows the largest value for $\overline{\Delta}_{\Lambda,agg}$ which is caused by the presence of a large water body.

The results obtained by the linearization approach for the Netherlands shows that *only for the grids where large water bodies are present* $\overline{\Delta}_{\Lambda,agg}$ *is not negligibly small. For the remainder of the grids low resolution data seems to be sufficient to estimate* $\overline{\lambda E}$, $\overline{H}$ *and* $\overline{\Lambda}$. As was shown in the analysis of the Barrax data set a small value of $\overline{\Delta}_{\Lambda,agg}$ is not a guarantee that $\Delta_{\Lambda,agg}$ for all pixels will be equally small.

7.3.2 Convex hull approach

The convex hull approach has also been applied for all twenty grids, with the exception of grid number 5. The minimum and maximum values for $\overline{\lambda E}$ and $\overline{H}$ have been estimated. The whole data set has been used to infer the spatial variability. The exact range of solutions for $\overline{\lambda E}$ and $\overline{H}$ can only be derived when using the whole data set. In Figure 7.14a the results for the convex hull approach for the estimation of the minimum and maximum values of $\overline{\lambda E}$ are shown for the 20 grids. Also the results for $\overline{H}$ are shown in Figure 7.14b.

Figure 7.14a and b show that the range for the possible solutions of $\overline{\lambda E}$ and $\overline{H}$ are very large. The maximum values of $\overline{\lambda E}$ for all grids with the exception of grid 1 and 10 are around 400 W m^{-2}. The minimum values for $\overline{\lambda E}$ show a more diverse pattern. The values range from -200 until -1000 W m^{-2}. The values for $\overline{H}$ show the opposite, with the minimum values being more or less stable around 0 W m^{-2} and the maximum values range from 400 until 1400 W m^{-2}. These unreasonably low values for $\overline{\lambda E}$ and high values for $\overline{H}$ possibly are the effect of the low NDVI values present in the grid (see Table 5.5. The NDVI values are ≤ 0 for water, causing a overestimation of H and an underestimatoin of λE. Also scan errors in the Landsat image

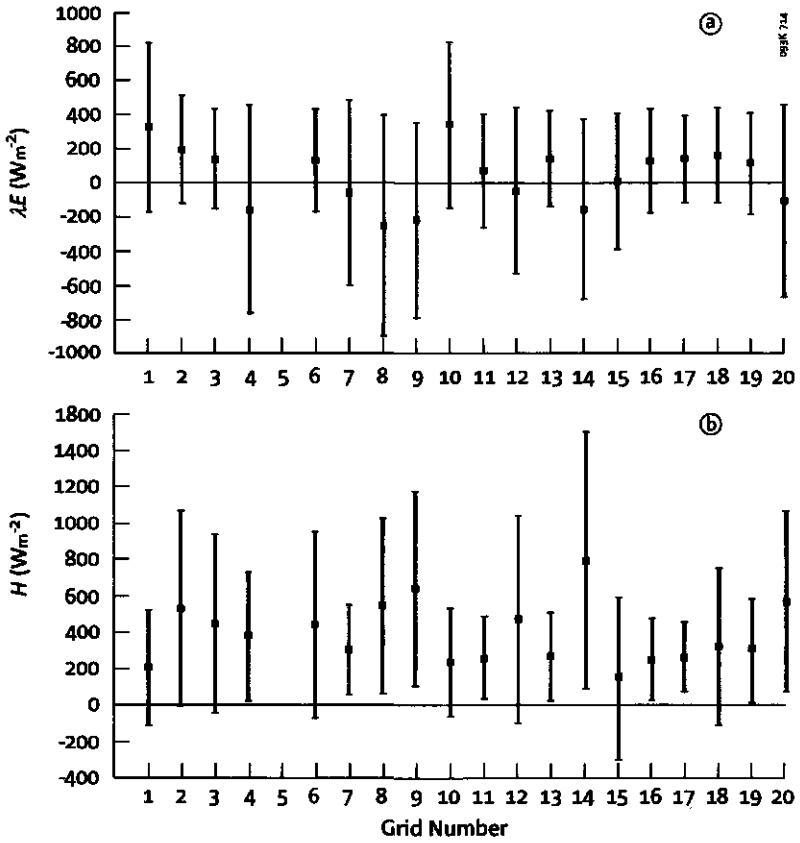

Figure 7.14: Estimation of a) the aggregated latent heat flux density, $\overline{\lambda E}$ and b) the aggregated sensible heat flux density, $\overline{H}$ using the convex hull approach for the Netherlands, 24 May 1995 for the 20 grids shown in Plate E. The square indicates the average value, whereas the extent of the bars show the range of possible values for a) $\overline{\lambda E}$ and b) $\overline{H}$

can be a possible source of error. This pixels, although small in number, can alter the shape of the convex hull considerably, leading to strange values for $\overline{\lambda E}$ and $\overline{H}$. Especially when greenhouses are present in the image, the signal tends to get saturated, leading to much higher reflectances than normal.

The results of the convex hull analysis show however that *for a landscape like the Netherlands, low resolution remote sensing data cannot be used a priori to estimate* $\overline{\lambda E}$, $\overline{H}$ *and* $\overline{\Lambda}$.

7.4 Conclusions

In this section the conclusions based on the results for the aggregation analysis for all three test cases will be given. The overall relative error due to aggregation for H, λE and Λ: $\overline{\delta}_{H,agg}$, $\overline{\delta}_{\lambda E,agg}$ and $\overline{\delta}_{\Lambda,agg}$ obtained by the linearization approach has a maximum value of 10% for the three different data sets. Compared to the precision of field measurements which is roughly in the same order this indicates that low resolution remote sensing data may be used to map Λ for input in a NWPM model.

However the convex hull analysis showed that low resolution remote sensing data cannot be used a priori. Knowledge about the spatial variability at the process scale is still needed to determine the error due to aggregation. The wavelet variance is a good tool to determine the spatial variability at different length scales.

If one is interested not in a areal average of Λ, but in the actual values for each separate pixel, the resolution of the remote sensing data should be smaller than the actual process scale. If the resolution is larger than the process scale, the analysis of the Barrax site showed, that the error due to aggregation for Λ: $\delta_{\Lambda,agg}$ can be as large as 95 %.

Low resolution remote sensing data may be used to infer the aggregated value of Λ, if the spatial variability is known at the scale less or equal to the process scale. However interpretation of results based on individual pixels of low resolution remote sensing data should be done carefully, while individual pixels may not be representative of the area they cover.

Summary and conclusions

Land Surface Models (LSMs) describe the exchange of heat, moisture and momentum between the land surface and the atmosphere, i.e. the surface energy balance. These models can also be solved regionally using remote sensing data as input. Important input variables which can be derived from remote sensing data are surface albedo r_0, surface temperature T_0 and the vegetation index $NDVI$.

LSMs combined with remote sensing data describe the surface energy balance for a large area. That makes this type of models suitable for inclusion in Numerical Weather Prediction Models (NWPMs). The LSM can be used to provide the lower boundary condition for a NWPM.

The partitioning of net available energy into latent and sensible heat flux density, λE and H respectively, has an impact on the formation of clouds and therefore on the amount of precipitation, the radiation balance and the distribution of water vapor in the atmosphere. The partitioning can be described by the evaporative fraction Λ, being a soil wetness indicator. Low resolution remote sensing data, having a high temporal resolution are suitable for updating Λ on a daily basis, thus steering the NWPM.

The coupling of a LSM with a NWPM is however not trivial. The grid cell size of a NWPM is much larger than the pixel size of any remote sensing data. *The results obtained by the LSM on the basis of remote sensing data should therefore be aggregated towards the grid cell size of a NWPM.* Two important aspects have then to be taken into account:

- The resolution of the observation versus the scale of the process involved
- The type of model used to infer the soil wetness indicator from remote sensing data i.e. linear or non-linear

When the resolution of the observation is larger than the scale of the process involved *and* the type of model is non-linear, then linear averaging of the results to the scale of a NWPM grid cell is not allowed. Therefore the central research question stated in this thesis is defined as: *How to areally aggregate soil wetness indicators, accounting for their length scales and resolutions at which they can be sampled by advanced satellite sensors, from*

pixel to meso scale.

In Chapter 2 the most important land surface processes involved in the description of the exchange of momentum, heat and moisture have been described. These processes are of a turbulent nature and formulations of the profiles of specific humidity, windspeed and temperature in the lower part of the atmospheric boundary layer are given. The atmospheric boundary layer is the layer which is directly influenced by land surface processes. The flux profile relationships derived for the lower part of the boundary layer are rewritten to be valid for the entire atmospheric boundary layer.

Land surface evaporation has been described by the Penman-Monteith equation where flux densities are analogous to electrical currents. The influence of stomata, wind speed and other factors affecting the land surface evaporation are described by resistances. On the basis of the Penman-Monteith equation and the flux profile relationship valid for the entire boundary layer a Land Surface Model that incorporates remote sensing data is introduced, i.e. Surface Energy Balance Index (SEBI). The SEBI model uses three input variables derived from remote sensing data: r_0, T_0 and $NDVI$. The latter being used to describe the surface roughness. The main principle of SEBI is the choice for the temperature difference between land surface and air, $T_0 - T_a$, as an indicator for Λ. The Penman-Monteith equation is used to derive theoretical values of $T_0 - T_a$ for zero respectively maximum evaporation. The observed $T_0 - T_a$ is used then to estimate actual evaporation. The air temperature, T_a is chosen at the height of the boundary layer, where T_a can assumed to be constant for a large area.

In Chapter 3 a methodology is presented how to aggregate distributed land surface model results towards a NWPM grid scale. In this thesis the land surface model is SEBI, whereas the distributed input variables are r_0, T_0 and $NDVI$, derived from remote sensing data. First a theoretical framework for the aggregation of model results from the local to the large scale has been presented. The aggregation of distributed model results can be performed in different ways. One option is to aggregate the results derived from a distributed model f using distributed input variables. Another option is by using the average of the input variables as input for the distributed model f thereby producing an aggregated result. Both options will produce the same result if the distributed model is linear and/or the input data is completely homogeneous. The first option is the correct way of producing an aggregated result, if the resolution of the observation from which the input variables are derived is at least *smaller* than the length scale of the processes described by the distributed model f. The second option describes the effect of the resolution of the observation being *larger* than the length scale of the pro-

cesses described by the distributed model f. The difference between the two options is the error due to aggregation. Two aspects have to be quantified when describing the error due to aggregation: the non-linearity of the model and the land surface heterogeneity.

Two different approaches to predict the error due to aggregation have been introduced. The first approach is the linearization approach where the LSM can be approximated by a Taylor expansion. The effects of non-linearity and land surface heterogeneity on the error due to aggregation are described by the terms in the Taylor expansion, when neglecting third and higher order terms. In the case of only one input variable, the variance of that input variable across the area of interest describes the land surface heterogeneity, while the second order derivative of the LSM with respect to the input variable describes the degree of non-linearity of the LSM. This approach can also be extended to more than one variable. As a consequence covariance between different input variables has to be taken into account. *The linearization approach only works with weakly non-linear continuous models.*

The second approach is based on the convex hull. The convex hull of a set is the smallest convex domain which contains all points in the set. The convex hull can be used to define the range of valid results of a LSM given a certain low resolution measurement for the input variables. The boundaries can be calculated on the basis of the natural spatial variability of the input variables for the area covered by the low resolution measurement. *The convex hull approach works for continuous as well for discontinuous models.*

In Chapter 4 the wavelet transform is introduced to determine the length scales of land surface characteristics from remote sensing data. It is a relatively new technique, which enables one to study features of a data set with a detail matched to their scale i.e. broad features on a large scale and fine features on a small scale.

The main advantage of the wavelet transform when compared to the Fourier transform is its capability to capture the variability in non-stationary signals. In this thesis the discrete wavelet transform has been chosen as a tool for the length scale analysis.

One appearance of a discrete wavelet transform, the fast wavelet transform represents a data set in a non-redundant fashion. The fast wavelet transform can be used to decompose a data set into *details, smooths and roughs*. The resolution of the original data set is called high resolution. Any other resolution derived from the original resolution is called low resolution. The decomposition of a data set into details, smooths and roughs is called a multi-scale analysis. The *smooths* are representations of a data set of a low resolution, the *details* are representing the amount of variability lost while transferring from one resolution to a lower one. The *roughs* are the amount

of variability while transferring from the original high resolution to a lower resolution. For any resolution the summation of the smooths and the roughs provide the original image.

The variance of the wavelet coefficients describing the details is also known as the wavelet variance, which gives for each resolution the amount of variance that can be explained by that specific resolution. Therefore, it is a natural tool to investigate the spatial scales of variability of remote sensing data. A test with images with predescribed length scales for different type of wavelets has been carried out. *In determining the dominant length scales of an image, the Haar wavelet produced the best results .*

In Chapter 5 three different data sets consisting of field and remote sensing measurements have been introduced.

The first data set has been collected in the framework of the EFEDA campaign, which was held in Spain, June 1991. The data set consists of an airborne TMS-NS001 image of the Barrax region. Within the Barrax region the most remarkable feature is the presence of pivot irrigation systems. These irrigated surfaces show large contrasts with the surrounding agricultural fields which are not irrigated.

The second data set consists of airborne DAEDALUS imagery, obtained at the Jornada Experimental Range, Las Cruces, New Mexico during the summer of 1997. The Jornada Experimental range is located in the northern region of the Chihuahuan desert, the most arid of the North American grasslands. Three test sites were identified: a grass site where grass is the dominant vegetation, a mesquite site where the mesquite bush is the dominant vegetation and the transition site where the grass is gradually taken over by the mesquite bush.

The third data set consists of four Landsat TM satellite images obtained in the summer of 1995 for the Central Part of the Netherlands. The data are representative of a temperate oceanic climate, and for a highly developed urban and agricultural region. The Landsat TM images have been divided into 20 equally sized grids.

For all three data sets the retrieval procedures to obtain r_0, T_0 and $NDVI$ from the remote sensing data have been discussed.

In Chapter 6 the results of the length scale analysis for the three data sets are discussed.

The length scale analysis for the Barrax data set showed that the dominant length scale ℓ^*_{dom} for all three land surface characteristics is equal to the average size of the pivot irrigation systems. These systems are clearly the dominant feature in the Barrax area. This confirmed the validity of the approach developed to measure the length scales. The amount of variability

explained by the length scales larger or equal to ℓ^*_{dom} which is about 70 %.

The length scale analysis for the Jornada Experimental range showed that for this type of landscape most of the variability can be explained by the smallest length scales. It seems that even a resolution of 4 m is not sufficient to describe all variability being present. However compared to the data sets of Barrax and the Central Part of the Netherlands the amount of variability for r_0, T_0 and $NDVI$ is low.

The length scale analysis for the Central Part of the Netherlands has been applied to 20 square grids in which the Landsat TM image was subdivided. The average for all grids showed that ℓ^*_{dom} is equal to 1920 m for all three land surface characteristics r_0, T_0 and $NDVI$. However looking at the individual grids there seemed to be a large degree of variability of ℓ^*_{dom} for r_0, T_0 and $NDVI$. A remarkable feature for all grids and land surface characteristics in the Central Part of the Netherlands is that only between 15 and 25 % of the variability is explained by ℓ^*_{dom}. This leads to the conclusion that the variability for the land surface characteristics in the Netherlands is not bound to one single length scale.

The curves describing the wavelet variance of r_0, T_0 and $NDVI$ showed a comparable shape for the three land surface characteristics. There were differences between the different data sets. Only for the grass site at the Jornada Experimental range the wavelet variance curve is different for all three land surface characteristics.

The optimal sensor resolution which was defined as the length scale at which more than 90 % of the variability was explained. Only for the Jornada experimental range ℓ^*_{dom} was equal to the optimal sensor resolution: 4 m. The optimal sensor resolution was for the Netherlands either 60 or 120 m, depending on the land surface characteristic. For the Barrax site the optimal sensor resolution was equal to 296 m.

In Chapter 7 the linearization and convex hull approach, which were discussed in Chapter 3, have been tested using data from the three test sites.

First the surface energy balance has been calculated for the Barrax area using SEBI based on a comparison between field measurements and SEBI results. The performance of SEBI was satisfactory, with a Root Mean Square Error for Λ of 0.04. The different terms of the surface energy balance, H, λE and Λ were then aggregated using the two different options described in the theoretical framework of Chapter 3. One where the distributed results were averaged and another where the input variables were averaged. The difference between both results is the error due to aggregation. The overall relative error due to aggregation for the results of SEBI are for H 5 %, for λE 9 % and for Λ 8 %. These errors occur when on the basis of one low resolution measurement of the Barrax area an area average value for H, λE

and Λ will be calculated. However looking at individual pixels the relative errors are the largest for high resolution data and decrease with increasing pixel size. The maximum relative error due to aggregation for Λ was 95 % and occurred at a resolution of 37 m, whereas the original resolution was 18.5 m. To estimate the error due to aggregation the linearization approach and the convex hull approach have been applied to the Barrax data set.

The linearization approach uses the wavelet variance and covariance as a measure for the spatial variability of the land surface characteristics. The non-linearity term, given by the derivatives of SEBI with regard to the input variables has been derived numerically. The linearization approach showed that the wavelet variance and covariance are good measures for the error due to aggregation at different resolutions. The estimation of the degree of non linearity of the LSM is more troublesome. Using the linearization approach a procedure has been outlined how to correct results based on low resolution remote sensing data for errors due to aggregation.

The range of results for area-averaged values of H, λE and Λ was calculated using the convex hull approach. Compared to the results obtained for the Barrax area the maximum error due to aggregation for H is 36 %, for λE 45 % and for Λ 32 %. The spatial variability of the input variables was derived using the full data set. A test case where the spatial variability was derived using only 1% of the pixels, showed a decrease in the maximum error as expected. Compared to the full data set however a reasonable estimation of the maximum errors could be given. When however the spatial variability was based on remote sensing data resampled to the resolution of the NOAA sensor, 1000 m, the results became very poor. To infer the domains of the spatial variability of the land surface characteristics, high resolution imagery should be used.

The linearization and convex hull approach have also been applied to both the Jornada data set and the Netherlands data set. For the Jornada data set both approaches showed that the error due to aggregation of H, λE and Λ is negligible. The real spatial variability within the Jornada Experimental range is confined to length scales smaller than 4 m.

The linearization approach applied to the Central Part of the Netherlands data set showed some mixed results for the 20 grids. The range in the overall error due to aggregation for Λ varies between 0 - 10 %. The grids with the largest aggregation errors contained large water bodies within their limits. The grids showing the smallest errors applied to rather homogeneous agricultural regions, with most of the landscape being pasture. The convex hull approach showed however that the range of results of SEBI based on low resolution measurements was rather large for all grids. The spatial variability has been derived using the full data set. Extreme values were probably caused by scan errors and low NDVI values.

To infer the aggregated value of evaporative fraction Λ low resolution re-

mote sensing data cannot be used without having any information on the spatial variability at higher resolutions. The results obtained by the linearization approach show that using high resolution data the overall aggregation error can indeed be estimated. The linearization approach showed that for even very heterogeneous areas the overall error due to aggregation is not larger than 10%. However the results based on the convex hull analysis show that the overall error due to aggregation can be much larger than observed for the three test cases. Therefore knowledge of the spatial variability at the process scale is needed.

Perspectives for future resarch

The results presented in this thesis showed for the three test sites that if low resolution remote sensing data are used to infer areally aggregated values of Λ with an error would occur. This result is also dependent on the chosen LSM, i.e. SEBI. Su et al. (1999) found an error due to aggregation for the Barrax area, based on the SEBAL model (Bastiaanssen95), being larger than found for the SEBI model in this thesis. However the SEBAL model is not scale invariant. The driving force behind SEBAL is the ability to detect completely dry and wet regions in the image. As the resolution of the remote sensing decreases it gets harder to detect completely dry and wet regions. The error due to aggregation depends on the LSM used. An important characteristic of the LSM should be scale invariance. A more sophisticated SVAT (Soil Vegetation Atmosphere Transfer) model should be used to infer the error due to aggregation and should be compared to the results obtained by SEBI.

In this thesis only three case studies have been treated. For a more general picture the aggregation analysis should also be taken to a *global* level. To get an idea about the aggregation on that level one should apply a global land use map, such as the global land cover classification system developed by the International Geosphere-Biosphere Programme Data and Information Systems Land Cover Working Group (IGBP-DIS LCWG), which uses 17 different biomes. For each biome the spatial variability of the different land surface characteristics, r_0, T_0 and $NDVI$ has to be quantified. This can be done by using several high resolution data sets which are acquired for the different biomes. For each biome the convex hull approach would indicate the range of possible results of H, λE and Λ. Extrapolating the results for each biome to the global scale using the land cover map would give an idea for which areas low resolution remote sensing data could be used without producing large aggregation errors.

Several adjustments to the approaches to estimate the error due to aggregation can be made. The linearization approach uses the wavelet variance as an estimation of the land surface heterogeneity at different resolutions. The wavelet variance has been estimated using the Fast Wavelet Transform. This leads to results presented at a dyadic scale. A possible improvement could be using a continuous wavelet transform, thereby producing a continuous wavelet variance curve. This would give information on the aggregation error for all possible resolutions.

Finally all the test cases have been carried out for regions with a rather flat topography. In regions with considerable topography the error due to aggregation could be much larger due to increase of variability of the land surface characteristics, most notably in the difference in surface reflectance, r_0 and surface temperature T_0 between north and south oriented slopes. Low resolution remote sensing data will not be able to detect the individual slopes and are therefore a possible source of errors due to aggregation.

Samenvatting en conclusies

LandOppervlak Modellen (LOM) beschrijven de uitwisseling van warmte en vocht tussen het landoppervlak en de atmosfeer, resulterend in de landoppervlak energiebalans. Normaliter worden deze modellen opgelost voor een enkel punt op het landoppervlak. Echter deze modellen kunnen ook voor een groter gebied worden toegepast door remote sensing gegevens te gebruiken als invoer. Belangrijke invoer variabelen die kunnen worden afgeleid van remote sensing gegevens zijn de oppervlakte albedo r_0, de oppervlakte temperatuur T_0 en de vegetatie index $NDVI$.

Een LOM gecombineerd met remote sensing gegevens beschrijft de landoppervlak energiebalans voor een groot gebied. Zo kan de hoeveelheid warmte en vocht die worden uitgewisseld tussen atmosfeer en landoppervlak worden bepaald voor een groot gebied. Een Numeriek Weervoorspelling Model (NWM) gebruikt deze informatie als invoer. In een NWM is het landoppervlak verdeeld in grote gridcellen (> 625 km^2), die een oppervlakte hebben die vele malen groter is als het oppervlak wat een pixel van een remote sensing beeld bedekt (1000 m^2 - 25 km^2).

De verdeling van de netto beschikbare energie aan het landoppervlak tussen latente en voelbare warmte stroomdichtheid, λE en H respectievelijk, heeft invloed op de vorming van wolken en daardoor op de hoeveelheid neerslag, de stralingsbalans en de verdeling van waterdamp in de atmosfeer. De verdeling tussen H en λE kan worden beschreven door de verdampingsfractie, Λ, een bodemvocht indicator. Lage resolutie remote sensing gegevens (oppervlakte pixel > 1 km^2), met een hoge temporele resolutie (minstens 1 keer per dag) zijn geschikt voor het dagelijks bijsturen van Λ, daarbij de resultaten van de NWM corrigerend.

De koppeling van een LOM met een NWM is echter niet triviaal. Zoals eerder vermeld, het oppervlak bedekt door een NWM gridcel is veel groter dan het oppervlak bedekt door een pixel. *De resultaten berekend door een LOM met remote sensing gegevens als invoer moeten daarom worden geaggregeerd tot de grootte van een NWM gridcel.* Daarbij moet rekening worden gehouden met twee belangrijke aspecten:

- De resolutie van de waarneming ten opzichte van de schaal van het proces dat wordt beschreven.

- Het soort model waarmee het proces wordt beschreven: lineair of niet lineair.

Wanneer de resolutie van de waarneming lager is dan de schaal van het te beschrijven proces *en* het gebruikte model is niet lineair, dan is het lineair middelen van de resultaten tot de schaal van de NWM grid cel niet geoorloofd. De centrale onderzoeksvraag in dit proefschrift is dan de volgende: *Hoe moet men bodemvochtindicatoren ruimtelijk aggregreren van pixel tot NWM gridcel grootte, rekening houdend met de lengte schaal van het beschreven proces en de ruimtelijke resolutie waarmee invoergegevens voor een landoppervlak model kunnen worden gekarteerd door middel van geavanceerde satelliet sensoren?*

In Hoofdstuk 2 worden de belangrijkste processen beschreven die verantwoordelijk zijn voor de uitwisseling van momentum, warmte en vocht tussen landoppervlak en atmosfeer. Deze processen zijn turbulent van aard. De vergelijkingen die de profielen geven van specifieke vochtigheid, wind snelheid en temperatuur in het onderste deel van de atmosferische grenslaag worden ook wel flux-profiel vergelijkingen genoemd. De atmosferische grenslaag is de laag die direct wordt beinvloed door processen aan het landoppervlak. De flux-profiel vergelijkingen die zijn afgeleid voor de onderste laag van de atmosferische grenslaag zijn herschreven om ze geldig te laten zijn voor de gehele atmosferische grenslaag.

Verdamping aan het landoppervlak wordt beschreven door de Penman-Monteith vergelijking die analoog aan de beschrijving van een elektrische stroom, de stroomdichtheid van de verdamping beschrijft. De invloed van huidmondjes, windsnelheid en andere factoren op de verdamping wordt beschreven door middel van weerstanden. Met als basis de Penman-Monteith vergelijking en de flux-profiel vergelijkingen die geldig zijn voor de gehele grenslaag is een LOM ontwikkeld dat geschikt is om remote sensing gegevens als invoer te gebruiken: SEBI (Surface Energy Balance Index). Het SEBI model gebruikt drie invoer variabelen die kunnen worden afgeleid met behulp van remote sensing gegevens: r_0, T_0 en $NDVI$. De $NDVI$ wordt gebruikt om de ruwheid van het landoppervlak te beschrijven. Het principe van SEBI wordt gegeven door de keuze voor het temperatuur verschil tussen landoppervlak en lucht, $T_0 - T_a$, als een indicator voor de verdampingsfractie Λ. De Penman-Monteith vergelijking wordt gebruikt om theoretische waarden voor $T_0 - T_a$ af te leiden voor het geval dat er geen verdamping is en voor het geval van maximale verdamping. De bijbehorende weerstanden volgen uit de flux-profiel vergelijkingen. De waargenomen $T_0 - T_a$ wordt dan gebruikt om de actuele verdamping te schatten. De lucht temperatuur T_a is gekozen op de hoogte van de atmosferische grenslaag, waar T_a geacht wordt constant te zijn voor een groot gebied. Deze waarde wordt bepaald aan de hand van

metingen van het temperatuur profiel.

In Hoofdstuk 3 wordt beschreven hoe ruimtelijk verdeelde resultaten van een LOM, in dit proefschrift SEBI, kunnen worden geaggregeerd tot de schaal van een NWM gridcel. SEBI gebruikt als ruimtelijk verdeelde invoer variabelen r_0, T_0 en $NDVI$, welke afgeleid zijn van remote sensing gegevens. Een theoretisch kader is gepresenteerd waarin wordt beschreven hoe ruimtelijk verdeelde model resultaten kunnen worden geaggregeerd. De aggregatie van ruimtelijk verdeelde model resultaten kan op twee verschillende manieren worden uitgevoerd. De eerste manier is om de ruimtelijk verdeelde *resultaten* van een model f te aggregeren. Het model f heeft daarbij als invoer ruimtelijk verdeelde variabelen. De tweede manier is om de ruimtelijk verdeelde *invoer* variabelen voor het model f te aggregeren wat een geaggregeerde uitvoer oplevert.

Beide manieren zullen hetzelfde resultaat geven als het model f lineair is en/of de invoer variabelen volkomen homogeen zijn. De eerstgenoemde manier van aggregeren is de correcte manier van aggregeren, wanneer de resolutie van de waarnemingen waarmee de invoer variabelen zijn afgeleid op zijn minst gelijk is aan de lengte schaal van het proces beschreven door het gedistribueerde model f. De tweede manier aggregeren beschrijft het effect wanneer de resolutie van de waarneming niet gelijk is aan de lengte schaal van het process beschreven door het gedistribueerde model f. Het verschil tussen de resultaten van beide manieren van aggregeren is de aggregatie fout. Twee aspecten moeten worden gekwantificeerd bij het beschrijven van de aggregatie fout: de mate van niet-lineariteit van het model f, in dit geval SEBI, en de mate van heterogeniteit van het landoppervlak.

Twee verschillende manieren van aanpak worden gegeven om de aggregatie fout te voorspellen. De eerste manier van aanpak is de linearizatie aanpak waarbij een LOM wordt benaderd door middel van een Taylor-reeks. De effecten van de niet-lineariteit van een LOM en de heterogeniteit van het landoppervlak op de aggregatie fout worden hier beschreven aan de hand van de verschillende termen van een Taylor reeks. Wanneer er slechts sprake is van één ruimtelijk verdeelde invoer variabele voor een LOM, beschrijft de variantie van die ruimtelijk verdeelde invoer variabele de heterogeniteit van het landoppervlak. De tweede orde afgeleide van het LOM met betrekking tot die invoer variabele beschrijft dan de niet-lineariteit van het LOM. Deze aanpak kan ook worden uitgebreid tot meer dan één variabele. In dat geval moet ook de covariantie tussen de verschillende ruimtelijk verdeelde invoer variabelen worden meegenomen. De linearizatie aanpak werkt alleen bij zwak niet-lineaire modellen die tevens continu zijn.

De tweede aanpak is gebaseerd op een geometrisch concept: de convex hull. De convex hull van een groep gegevens is het kleinste convex domein dat

alle punten in die groep gegevens omvat. De convex hull kan worden gebruikt om het theoretisch bereik aan te geven van geldige resultaten van een LOM gegeven één enkele lage resolutie waarneming voor de ruimtelijk verdeelde invoer variabelen van de LOM. Het bereik van de resultaten kan worden bepaald door een voorstelling te maken van de ruimtelijke variabiliteit van de invoer gegevens voor het gebied dat bedekt wordt door die enkele lage resolutie waarneming. De convex hull aanpak heeft als voordeel dat het werkt voor zowel modellen die continu alswel modellen die discontinu zijn.

In Hoofdstuk 4 is de wavelet transformatie beschreven die in dit proefschrift gebruikt wordt om lengte schalen van landoppervlak eigenschappen te bepalen aan de hand van remote sensing gegevens. De wavelet transformatie, een relatief nieuwe techniek, is uitermate geschikt om gegevens uit te splitsen in kleine (details) en grote elementen. Het grote voordeel van de wavelet transformatie in vergelijking tot de Fourier transformatie is de mogelijkheid om de variabiliteit in niet-stationaire signalen weer te geven. In dit proefschrift is de discrete wavelet transformatie gekozen als gereedschap voor de lengte schaal analyse. De Fast Wavelet Transform, een specifieke vorm van de discrete wavelet transformatie geeft een set gegevens weer in een niet overcomplete weergave van wavelet coefficienten. De Fast Wavelet Transform kan worden gebruikt om een set gegevens onder te verdelen in "details", "smooths" en "roughs". De resolutie van de originele set gegevens wordt hier hoge resolutie genoemd. Elke andere resolutie die van de hoge resolutie is afgeleid wordt aangeduid met lage resolutie. De onderverdeling van een set gegevens in details, smooths en roughs wordt een multi-schaal analyse genoemd. De "smooths" zijn een representatie van de set gegevens bij een lage resolutie. De "details" geven het verlies in informatie van een set gegevens weer, wanneer de resolutie van deze set gegevens is verlaagd. De "roughs" geven het verlies in informatie van een set gegevens tussen de (originele) hoge resolutie van een set gegevens en een lage resolutie versie daarvan. Bij alle lage resoluties geeft de som van de "smooths" en de "roughs" samen de hoge resolutie versie van de set gegevens. De variantie van de wavelet coefficienten die gebruikt worden om de "details" te vormen staat ook bekend als wavelet variantie. De wavelet variantie geeft voor elke resolutie de grootte van de variantie weer die kan worden toegeschreven aan elementen met een grootte gelijk aan die resolutie. Daarom is de wavelet variantie een geschikt stuk gereedschap om te gebruiken voor het karteren van lengte schalen van landoppervlak eigenschappen in remote sensing beelden. Een test is uitgevoerd waarin beelden met een van te voren vastgestelde dominante lengte schaal zijn gebruikt om verschillende type wavelets te testen voor hun geschiktheid om lengte schalen te karteren. *Uit de test resultaten kwam naar voren dat de Haar wavelet de meest geschikte wavelet was om de dominante lengte schaal van een beeld te karteren.*

In Hoofdstuk 5 zijn drie verschillende sets van gegevens bestaande uit veldmetingen en remote sensing beelden beschreven. De eerste set gegevens is verzameld in het kader van de EFEDA campagne, gehouden in juni 1991 in de omgeving van Barrax, Spanje. De gegevens bestaan uit veldmetingen en een vliegtuigopname gemaakt met de TMS-NS001 sensor van het gebied rond Barrax. In de Barrax regio is het meest in het oog springende kenmerk de aanwezigheid van pivot irrigatie systemen. Deze geirrigeerde gebieden contrasteren sterk met de omliggende landbouwgebieden die niet worden geirrigeerd.

De tweede set gegevens bestaat uit vliegtuigopnamen gemaakt met de DAEDALUS sensor, opgenomen in de zomer van 1997 op het terrein van de Jornada Experimental Range, Las Cruces, New Mexico, Verenigde Staten. De Jornada Experimental Range is gesitueerd in de noordelijke contreien van de Chihuahua woestijn, de droogste aller Noord-Amerikaanse graslanden. Drie test gebieden zijn onderscheiden: een gras gebied waar gras de dominante vegetatie is, een mesquite gebied waar de mesquite struik de dominante vegetatie is en een overgangs gebied waar het gras geleidelijk aan wordt verdrongen door de mesquite struiken.

De derde set gegevens bestaat uit vier Landsat TM satelliet beelden van midden-Nederland, opgenomen in de zomer van 1995. De gegevens zijn representatief voor een sterk verstedelijkt gebied in een gematigd klimaat. De Landsat TM beelden zijn verdeeld in 20 even grote vierkanten. Voor elke set van gegevens zijn de procedures om de landoppervlak eigenschappen r_0, T_0 en de $NDVI$ te bepalen besproken.

In Hoofdstuk 6 worden de resultaten voor de lengte schaal analyse besproken. De lengte schaal analyse voor de Barrax gegevens laat zien dat de dominante lengte schaal ℓ^*_{dom} voor alle drie landoppervlak eigenschappen, r_0, T_0 en $NDVI$ gelijk is aan de gemiddelde grootte van de pivot irrigatie systemen. Deze systemen zijn duidelijk het meest belangrijke kenmerk in de Barrax regio. Dit bevestigt ook de validiteit van de aanpak om de lengte schalen te meten met de wavelet variantie. De hoeveelheid variantie die wordt verklaard door elementen met een lengte schaal groter of gelijk aan ℓ^*_{dom} is ongeveer gelijk aan 70 %.

De lengte schaal analyse voor de Jornada Experimental Range laat zien dat voor dit type landschap de meeste informatie aanwezig is in de kleinste lengte schalen. Het lijkt erop dat een resolutie van 4 m zelfs niet voldoende is om alle heterogeniteit van het landoppervlak te verklaren. Echter vergeleken met de gegevens van Barrax en midden-Nederland is de totale hoeveelheid variantie voor de landoppervlak eigenschappen laag.

De lengte schaal analyse voor midden-Nederland is uitgevoerd voor alle

twintig vierkanten waarin het beeld is onderverdeeld. Het gemiddelde voor alle vierkanten laat zien dat ℓ^*_{dom} gelijk is aan 1920 m voor de drie land oppervlak eigenschappen r_0, T_0 en $NDVI$. Echter als men kijkt naar de afzonderlijke vierkanten dan is er behoorlijk wat variatie in ℓ^*_{dom} voor r_0, T_0 en $NDVI$. Een opmerkelijk kenmerk voor alle vierkanten en landoppervlak eigenschappen is dat slecht tussen de 15 en de 25 % van de heterogeniteit van het landschap wordt verklaard door ℓ^*_{dom}. Hieruit blijkt dat de heterogeniteit van de landoppervlak eigenschappen in midden-Nederland niet is gebonden aan één enkele lengte schaal.

Voor elke set van gegevens kent de wavelet variantie curve een zelfde karakteristieke verloop voor r_0, T_0 en de $NDVI$. De curves verschillen wel onderling tussen de verschillende sets aan gegevens. Slechts bij het gras gebied in de Jornada Experimental Range zijn de wavelet variantie curves voor r_0, T_0 en $NDVI$ verschillend.

De optimale sensor resolutie is gedefineerd als de lengte schaal waarop meer dan 90 % van de variabiliteit kan worden verklaard. Slechts voor de Jornada Experimental Range is ℓ^*_{dom} gelijk aan de optimale sensor resolutie: 4 m. De optimale sensor resolutie is voor midden-Nederland 60 of 120 m, afhankelijk van de landoppervlak eigenschap. Voor de Barrax gegevens set is de optimale sensor resolutie gelijk aan 296 m. De dominante lengte schaal ℓ^*_{dom} is dus niet per definitie gelijk aan de optimale sensor resolutie.

In Hoofdstuk 7 zijn de linearizatie en convex hull aanpak, besproken in Hoofdstuk 3 toegepast op de gegevens verzameld voor de drie sets van gegevens. Allereerst is voor het Barrax proefgebied de energiebalans berekend met SEBI gebruikmakend van de TMS-NS001 data. De resultaten zijn vergeleken met veldmetingen van de energiebalans, waaruit bleek dat de verdampingsfractie Λ was berekend met een absolute fout van 0.04. Om de aggregatie fout te bepalen zijn vervolgens de resultaten van SEBI, te weten H, λE en Λ, geaggregeerd volgens de twee verschillende manieren besproken in het theoretisch kader van Hoofdstuk 3. Eén manier waarbij de ruimtelijk verdeelde resultaten (H, λE en Λ) zijn gemiddeld en de andere manier waarbij de ruimtelijk verdeelde invoergegevens (r_0, T_0 en $NDVI$) zijn gemiddeld. Het verschil tussen beide uitkomsten is de aggregatie fout. De totale relatieve aggregatie fout voor de resultaten van SEBI is 5 % voor H, 9 % voor λE en 8 % voor Λ. De totale relatieve aggregatie fout is de fout die wordt gemaakt als op basis van één lage resolutie opname voor het hele Barrax gebied een gebiedsgemiddelde waarde voor H, λE en Λ wordt berekend. Echter als men kijkt naar tussenliggende resultaten waarbij het Barrax gebied niet wordt bedekt door één enkele lage resolutie pixel, maar door meerdere pixels met weliswaar een lagere resolutie dan de originele resolutie, dan blijkt dat de maximum relatieve aggregatie fout voor individuele

pixels toeneemt met afnemende pixel grootte (hogere resolutie). Echter de totale relatieve aggregatie fout neemt toe met toenemende pixel grootte. De maximum relatieve aggregatie fout voor Λ is 95 % bij een resolutie van 37 m, waarbij de originele resolutie van de gegevens 18.5 m is.

Om de aggregatie fout voor het Barrax beeld te schatten zijn de linearizatie en convex hull aanpak gebruikt en vergeleken met de voorgaande resultaten. De linearizatie aanpak gebruikt de cumulatieve wavelet variantie en covariantie als een maat voor de ruimtelijke variabiliteit van de landoppervlak eigenschappen. De niet-lineariteit term wordt gegeven door de afgeleide van SEBI met betrekking tot de invoer variabelen (r_0, T_0 en $NDVI$) en is bepaald met een numerieke methode. De linearizatie aanpak toont aan dat de cumulatieve wavelet variantie en covariantie een goede maat zijn voor het *verloop* van de aggregatie fout voor verschillende resoluties. De schatting van de mate van niet-lineariteit van SEBI is moeilijker. Op basis van de linearizatie aanpak is een procedure beschreven die resultaten van een LOM gebaseerd op invoer variabelen die berekend zijn aan de hand van lage resolutie remote sensing gegevens kan corrigeren voor aggregatie fouten

Het bereik van de resultaten voor gebiedsgemiddelde waarden voor H, λE en Λ zijn berekend met behulp van de convex hull aanpak. Vergeleken met de SEBI resultaten behaald voor het Barrax proefgebied is de maximum aggregatie fout 36 % voor H, 45 % voor λE en 32 % voor Λ. De ruimtelijke variabiliteit van de invoer variabelen is bepaald aan de hand van de gehele set van gegevens. Een proef waarbij de ruimtelijke variabiliteit is bepaald aan de hand van slechts 1 % van de gegevens, liet een daling van de maximum fout zien, vanwege de afgenomen variabiliteit. Echter het is nog steeds mogelijk een redelijke schatting van de maximale aggregatie fout te geven. Als men echter de resolutie van de set van gegevens terugbrengt tot een resolutie vergelijkbaar met de NOAA sensor, 1000 m, worden de resultaten van de convex hull analyse onbetrouwbaar. Dit komt omdat de resolutie van 1000 m lager is dan die van de optimale sensor resolutie, zoals bepaald in Hoofdstuk 6. Daarom moet om de ruimtelijke variabiliteit te schatten beelden van een resolutie vergelijkbaar met die van de optimale sensor resolutie worden gebruikt, waarbij echter niet de gehele set aan gegevens hoeft te worden gebruikt.

De linearizatie en convex hull aanpak zijn ook toegepast voor de proefgebieden van de Jornada Experimental Range en midden-Nederland. Voor het Jornada proefgebied lieten beide methodes zien dat de aggregatie fout verwaarloosbaar klein is. De echte ruimtelijke variabiliteit is in het Jornada proefgebied voorbehouden aan lengte schalen kleiner dan 4 m.

De resultaten behaald door de linearizatie aanpak voor midden-Nederland laten wisselende resultaten zien voor de twintig vierkanten. De totale aggregatie fout voor Λ varieerde van 0 to 10 %, waarbij de vierkanten die bestaan

deels uit land en deels uit open water de grootste aggregatie fouten kennen. De vierkanten met de kleinste aggregatie fouten bestaan over het algemeen uit relatief homogene landbouwgebieden, voornamelijk grasland. De convex hull aanpak laat echter zien dat voor alle vierkanten het bereik van de resultaten voor SEBI behoorlijk groot is. De ruimtelijke variabiliteit is bepaald aan de hand van de gehele set van gegevens. Extreme waarden worden waarschijnlijk veroorzaakt door scanfouten en lage waarden van de NDVI.

Het is niet mogelijk om de geaggregeerde waarde van de verdampingsfractie Λ*, berekend aan de hand van SEBI met behulp van lage resolutie remote sensing gegevens, betrouwbaar te bepalen zonder informatie over de ruimtelijke variabiliteit van de invoer gegevens bij een hogere resolutie. De resultaten behaald door de linearizatie aanpak tonen aan dat gebruikmakend van hoge resolutie beelden de aggregatie fout kan worden bepaald. De linearizatie aanpak toont tevens aan dat zelfs in het geval van Barrax, een sterk heterogeen gebied de aggregatie fout niet groter is dan 10 % voor* Λ*. Echter de resultaten behaald door de convex hull analyse tonen aan dat de totale aggregatie fout veel groter kan zijn dan hier aangetoond voor de drie proefgebieden. Om de aggregatie fout exact te bepalen is kennis van de ruimtelijke variabiliteit van de invoer gegevens nodig op een schaal gelijk aan de schaal van het proces beschreven in het land oppervlak model.*

Tot slot worden er nog een aantal suggesties voor toekomstig onderzoek gedaan.

Bibliography

Bastiaanssen, W. G. M. (1995). *Regionalization of surface fluxes and moisture indicators at composite terrain*. Ph.D. thesis, Wageningen Agricultural University, Department of Water Resources. 273 pp.

Becker, F. and Li, Z. L. (1995). Surface temperature and emissivity at various scales: Definition, measurement and related problems. *Remote Sensing Reviews*, 12:225–253.

Beljaars, A. C. M. and Bosveld, F. C. (1997). Cabauw data for the validation of land surface parameterisation schemes. *J Climate*, 10:1172–1193.

Blackadar, A. K. and Tennekes, H. (1968). Asymptotic similarity in neutral barotropic planetary boundary layers. *J. Atmos. Sci.*, 25:1015–1020.

Blöschl, G. and Sivalapan, M. (1995). Scale issues in hydrological modelling: A review. *Hydr. Processes*, 9:251–290.

Bolle, H.-J., André, J. C., Arrue, J. L., Barth, H. K., Bessemoulin, P., Brasa, A., de Bruin, H. A. R., Cruces, J., Dugdale, G., Engman, E. T., Evans, D. L., Fantechi, R., Fiedler, F., van de Griend, A. A., Imeson, A. C., Jochum, A., Kabat, P., Kratzsch, T., Lagouarde, J.-P., Langer, I., Llamas, R., Lopez-Baeza, E., Melia-Miralles, J., Muniosguren, L. S., Nerry, F., Noilhan, J., Oliver, H. R., Roth, R., Saatchi, S. S., Diaz, J. S., de Santa Olalla, M., Shuttleworth, W. J., Sogaard, H., Stricker, H., Thornes, J., Vauclin, M., and Wickland, D. (1993). Efeda: European field experiments in a desertification-threatened area. *Ann. Geophys.*, 11:173–189.

Bosveld, F. C., Bouten, W., Noppers, F., Steingröver, E., and Tiktak, A. (1993). The aciforn hydrological programme, the water cycle of a douglas fir forest. KNMI technical reports TR-152, KNMI. 23 pp.

Brutsaert, W. (1982). *Evaporation into the atmosphere: theory, history, and applications*. Reidel Publishing Company, Dordrecht, 299 pp.

Brutsaert, W. and Mawdsley, J. A. (1976). The applicability of planetary boundary layer theory to calculate regional evapotranspiration. *Water Resour. Res.*, 12:852–858.

Burke-Hubbard, B. (1996). *The world according to wavelets*. A.K. Peters, Wellesly, MA, 268 pp.

Chui, C. K. (1992). *Wavelet Analysis and its Applications, vol. 2, Wavelets – A Tutorial in Theory and Applications*. Academic Press, San Diego, CA, 723 pp.

Claussen, M., Lohmann, U., Roeckner, E., and Schulzweida, U. (1994). A global dataset of land-surface parameters. Technical report, Max-Planck-Institut für Meteorologie.

Cooley, J. W. and Tukey, J. W. (1965). An algorithm for the machine calculation of complex fourier series. *Math. Comp.*, 19:297–301.

Crawford, T. V. (1965). Moisture transfer in free and forced convection. *Quart. J. Roy. Meteorol. Soc.*, 91:18–27.

Csanady, G. T. (1967). The applicability of planetary boundary layer theory to calculate regional evapotranspiration. *J. Atmos. Sci.*, 24:467–471.

Daubechies, I. (1988). Orthonormal bases of compactly supported wavelets. *Commun. On Pure and App. Math.*, 41:909–996.

Daubechies, I. (1992). *Ten lectures on wavelets*. Soc. For Ind. And Appl. Math., Philadelphia, PA, 357 pp.

Deardorff, J. W. (1972). Numerical investigation of neutral and unstable planetary boundary layers. *J. Atmos. Sci.*, 29:91–115.

Dyck, S. and Baumert, D. (1991). A concept for hydrological process studies from local to global scale. In Kienitz, G., Milly, P., Genuchten, M. V., D.Rosbjerg, and Shuttleworth, W. (editors), *Proc. of the Vienna Symposium*, number 204 in IAHS Publications, pp. 31–42.

Dyer, A. J. (1967). The turbulent transport of heat and water vapour in an unstable atmosphere. *Quart. J. Roy. Meteorol. Soc.*, 93:501–508.

Dyer, A. J. and Hicks, B. B. (1970). Flux-gradient relationships in the constant flux layer. *Quart. J. Roy. Meteorol. Soc.*, 96:715–721.

Elbers, J. A., Dolman, A. J., Moors, E. J., and Snijders, W. (1996). Hydrologie en waterhuishouding van bosgebieden in nederland, fase 2: Meetopzet en eerste resultaten. Staring Centrum Rapport 333.2, Winand Staring Centre. (in Dutch). 65 pp.

Engman, E. T. (1990). Process in microwave remote sensing of soil moisture. *Can. J. Remote Sensing*, 16:6–14.

Foufoula-Georgiou, E. and Kumar, P. (1994). *Wavelets in Geophysics, Wavelet analysis and its applications, volume 4*. Academic Press, San Diego, CA, 373 pp.

Fourier, J. (1822). *La Theorie Analytique de la Chaleur*. University Press, London, 466 pp.

Fuchs, M. and Hadas, A. (1972). The heat flux density in a non-homogeneous bare loessial soil. *Boundary Layer Meteor.*, 3:191–200.

Gabor, D. (1946). Theory of communication. *J. IEE*, 93:429–445.

Garrat, J. R. (1992). *The atmospheric boundary layer*. Cambridge University Press, 670 pp.

Garrat, J. R. (1993). Sensivitiy of climate simulations to land-surface and atmospheric boundary layer treatments, a review. *J. Climate*, 6:419–449.

Gibbens, R. F., Havstad, K. M., Billheimer, D. D., and Herbel, C. H. (1993). Creosote bush vegetation after 50 years of logamorph exclusion. *Oecologia*, 94:210–217.

Haar, A. (1910). Zur theorie der orthogonalen funktionensysteme. *Math. Ann.*, 69:331–371.

Herrmann, F. (1997). *A scaling medium representation, a discussion on well-logs, fractals and waves*. Ph.D. thesis, Technical University Delft. 298 pp.

Hu, Z. and Islam, S. (1997). A framework for analyzing and designing scale invariant remote sensing algorithms. *IEEE trans. on geosc. and remote sensing*, 35(3):747–755.

Inoue, E. (1963). On the turbulent structure of airflow within crop canopies. *J. Meteorol. Soc. Japan*, 41:317–326.

Jackson, T. J. (1997). Soil moisture estimation using special satellite microwave/imager satellite data over a grassland region. *Water Resour. Res.*, 33(6):1475–1484.

Klemeš, V. (1983). Conceptualisation and scale in hydrology. *J. Hydrol.*, 653:1–23.

KNMI (1996). Jaaroverzicht van het weer in nederland, jaar 1995. JOW-bulletin 13, KNMI. (in Dutch).

Kumar, P. and Foufoula-Georgiou, E. (1997). Wavelet analysis for geophysical applications. *Rev. of Geophysics*, 35(4):385–412.

Mallat, S. (1989). A theory for multiresolution signal decomposition: the wavelet representation. *IEEE Trans. Pattern. Anal. Machine Intell.*, 11:674–693.

Mallat, S. (1998). *A wavelet tour on signal processing*. Academic Press, San Diego, CA, 637 pp.

Markham, B. L. and Barker, J. L. (1985). Thematic mapper bandpass solar exoatmospherical irradiances. *Int. J. of Rem. Sens.*, 8(3):517–523.

McNaughton, K. G. and Raupach, M. R. (1996). Responses of the convective boundary layer and the surface energy balance to large-scale heterogeneity. In Stewart, J. B., Engman, E. T., Feddes, R. A., and Kerr, Y. (editors), *Scaling up in hydrology using remote sensing*, pp. 171–182. John Wiley & Sons, Chichester, England.

Menenti, M. and Choudhury, B. J. (1993). Parameterization of land surface evaporation by means of location dependent potential evaporation and surface temperature range. In Bolle, H.-J., Feddes, R. A., and Kalma, J. (editors), *Exchange processes at the land surface for a range of space and time scales*, number 212 in IAHS Publications, pp. 561–568.

Milly, P. and Dunne, K. (1994). Sensitivity of the global water cycle to the water-holding capacity of land. *J. Climate*, 7:506–526.

Moene, A. F., de Bruin, H. A. R., and Holtslag, A. A. M. (1995). Validation of the surface parameterization of hirlam using surface-based measurements and remote sensing data. KNMI scientific reports WR 95-07, KNMI. 45 pp.

Monin, A. S. and Obukhov, A. M. (1954). Basic laws of turbulent mixing in the ground layer of the atmosphere. *Tr. Geofiz. Instit. Akad. Nauk*, 24(151):163–187. (in Russian).

Monteith, J. L. (1965). Evaporation and environment. *Symp. Soc. Exp. Biol.*, 19:205–234.

Monteith, J. L. (1973). *Principles of Environmental Physics*. Edward Arnold Press, London, 241 pp.

Pelgrum, H. and Bastiaanssen, W. G. M. (1997). The non-linearity between surface fluxes and remotely observable land surface characteristics and its consequences for pixel size selection. In *13^{th} conference on hydrology*, pp. 342–344. AMS, Long Beach, CA.

Penman, H. L. (1948). Natural evaporation from open water, bare soil, and grass. *Proc. Roy. Soc. London*, A193:120–146.

Percival, D. B. (1995). On estimation of the wavelet variance. *Biometrika*, 82:619–631.

Preparata, F. and Shamos, M. I. (1985). *Computational geometry: an introduction*. Springer Verlag, New York, NY, 390 pp.

Raffy, M. (1994). Heterogeneity and change of scale in models of remote sensing. spatialization of multi-spectral models. *Int. J. Remote Sensing*, 15(12):2359–2380.

Ranchin, T. and Wald, L. (1993). The wavelet transform for the analysis of remotely sensed images. *Int. J. Remote Sensing*, 14(3):615–619.

Reynolds, O. (1894). On the dynamical theory of incompressible viscous fluids and the determination of the criterion. *Phil. Trans. Roy. Soc. London*, A186:123–161.

Ritchie, J. C., Rango, A., Kustas, W. P., Schmugge, T. J., Brubaker, K., Havstad, K. M., Nolan, B., Prueger, J. H., Everitt, J. H., Davis, M. R., Schiebe, F. R., Ross, J. D., Humes, K. S., Hipps, L. E., Menenti, M., Bastiaanssen, W. G. M., and Pelgrum, H. (1996). Jornex: An airborne campaign to quantify rangeland vegetation change and plant community-atmospheric interaction. In *2nd international airborne remote sensing conference and exposition*, volume II, pp. 55–66. San Francisco, CA.

Rudloff, W. (1981). *World-Climates with tables of climatic data and practical suggestions*. Wissenschaftliche Verlagsgesellschaft, Stuttgart, 632 pp.

Schlesinger, W. H., Reynolds, J. F., Cunningham, G. L., Huenneke, L. F., Jarrel, W. M., Virginia, R. A., and Whitford, W. G. (1990). Biological feedbacks in global desertification. *Science*, 247:1043–1048.

Shukla, J. and Mintz, Y. (1982). Influence of land surface evapotranspiration on the earth's climate. *Science*, 215:1498–1501.

Stollnitz, E. J., DeRose, T. D., and Salesin, D. H. (1995). Wavelets for computer graphics: A primer, part 1. *IEEE Computer Graphics and Applications*, 15(3):76–84.

Su, Z., Pelgrum, H., and Menenti, M. (1999). Aggregation effects of surface heterogeneity in land surface processes. *Hydr. and Earth System Sciences*, 3(4):549–563.

Taconet, O., Bernard, R., and Vidal-Madjar, D. (1986). Evapotranspiration over an agricultural region using a surface flux/temperature model based on noaa-avhrr data. *J. Clim. Appl. Meteorol.*, 25:284–307.

van de Griend, A. A. and Owe, M. (1993). On the relationship between thermal emissivity and the normalized difference vegetation index for natural surfaces. *Int. J. of Rem. Sens.*, 14(6):1119–1131.

van den Hurk, B. J. J. M., Bastiaanssen, W. G. M., Pelgrum, H., and van Meijgaard, E. (1997). A new methodology for assimilation of initial soil moisture fields in weather prediction models using meteosat and noaa data. *J. Appl. Meteorol.*, 36:1271–1283.

Wilson, M. F. and Henderson-Sellers, A. (1985). A global archive of land cover and soils data for use in general circulation climate models. *J. Climatology*, 5:119–143.

Yaglom, A. M. (1977). Comments on wind and temperature flux-profile relationships. *Boundary-Layer Meteorol.*, 11:89–102.

Yamada, T. (1976). On the similarity functions a, b, c of the planetary boundary layer. *J. Atmos. Sci.*, 33(5):781–793.

Curriculum Vitae

Hendrik Pelgrum, 18 september 1969, Zutphen

1987: VWO diploma, Baudartius College, Zutphen
Aanvang studie Landbouw Universiteit Wageningen, Cultuurtechniek.
april-september 1992: stage CEMAGREF, Montpellier, Frankrijk.

1993: Ingenieursdiploma Cultuurtechniek, specialisatie Hydrologie en Waterbeheer, Landbouw Universiteit Wageningen
Afstudeervakken: Agrohydrologie, Bodemnatuurkunde.

1994: Vervangende dienstplicht, afdeling Waterhuishouding Aride Gebieden, SC-DLO, Wageningen.

1995: Aanvang promotieonderzoek, vakgroep Waterhuishouding Landbouwuniversiteit Wageningen,
gedetacheerd bij SC-DLO, Wageningen.
september 1997 - maart 1998: gastverblijf USDA-ARS Hydrology Laboratory, Beltsville, Maryland, VS.

2000: Internal Research Fellow, Earth Sciences Division, ESTEC, Noordwijk.

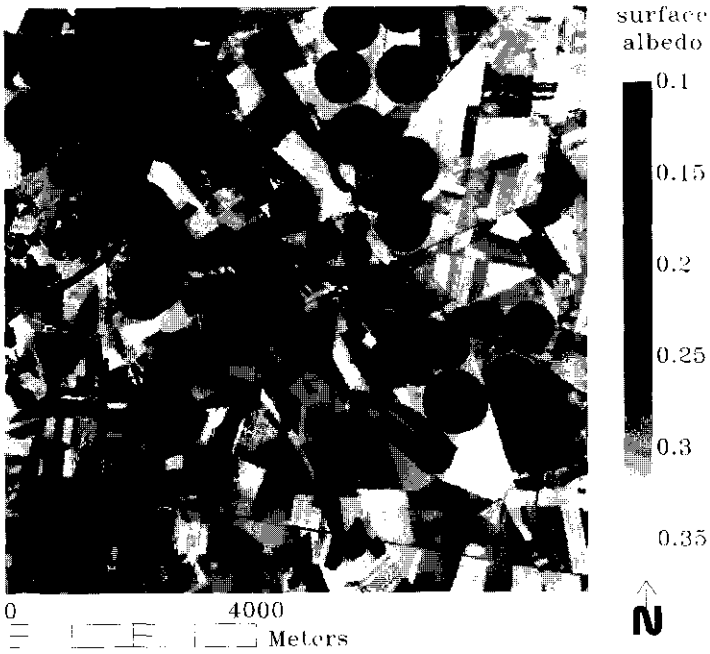

Plate A: Barrax, June 29 1991, surface albedo r_0.

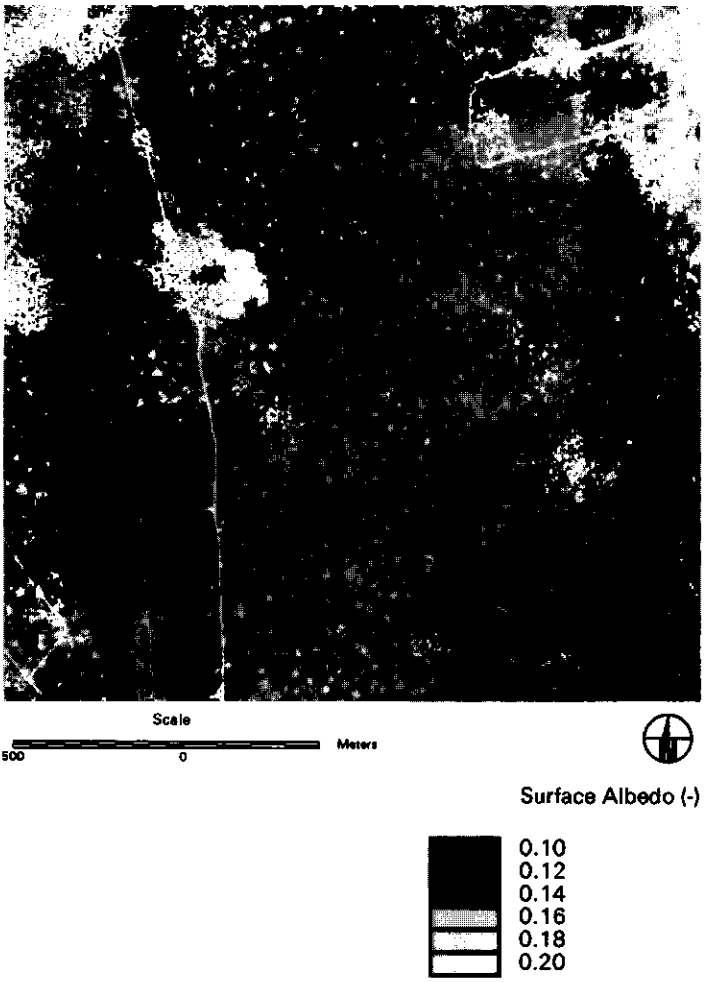

Plate B: Grass site, Jornada Experimental Range, June 19 1997, surface albedo r_0.

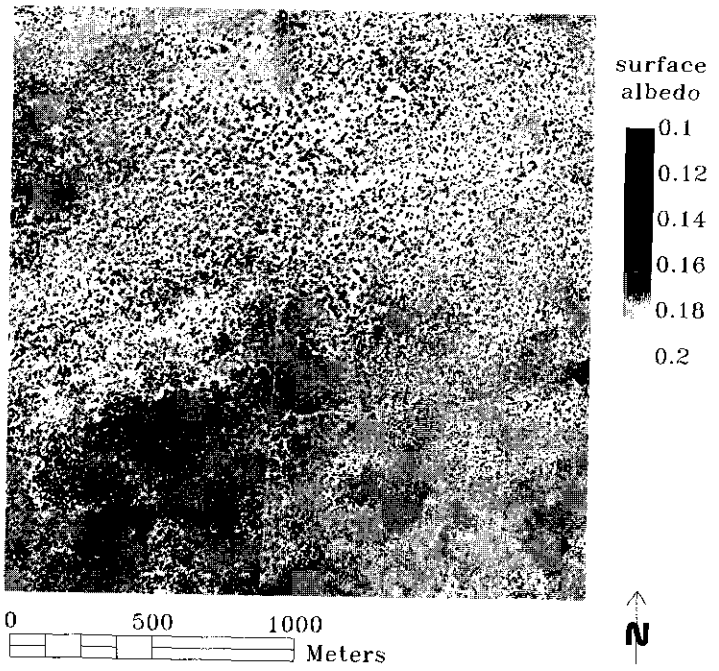

Plate C: Mesquite site, surface albedo r_0.

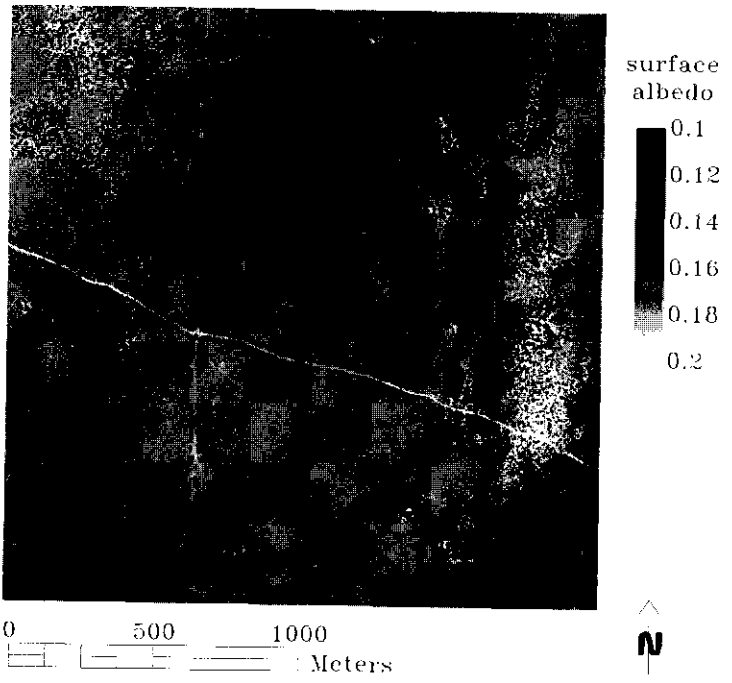

Plate D: Transition site, Jornada Experimental Range, June 19 1997, surface albedo r_0.

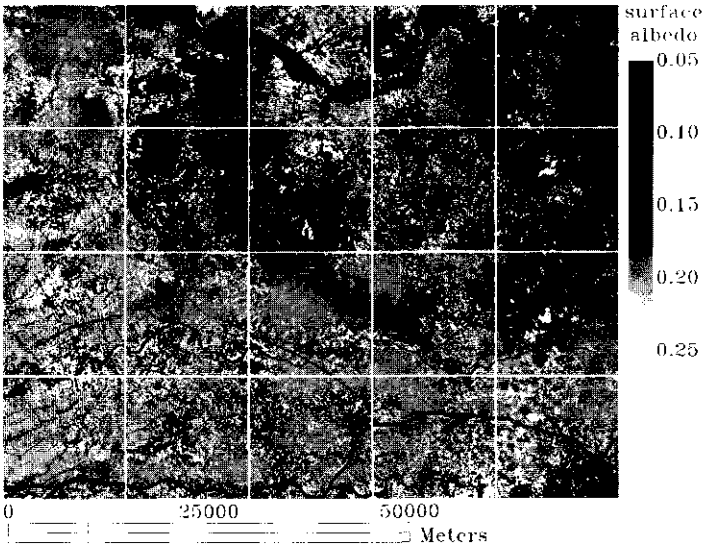

Plate E: The Central Part of the Netherlands, July 11 1995, surface albedo, r_0. The 20 grids used in the aggregation and length scale analysis are also shown.

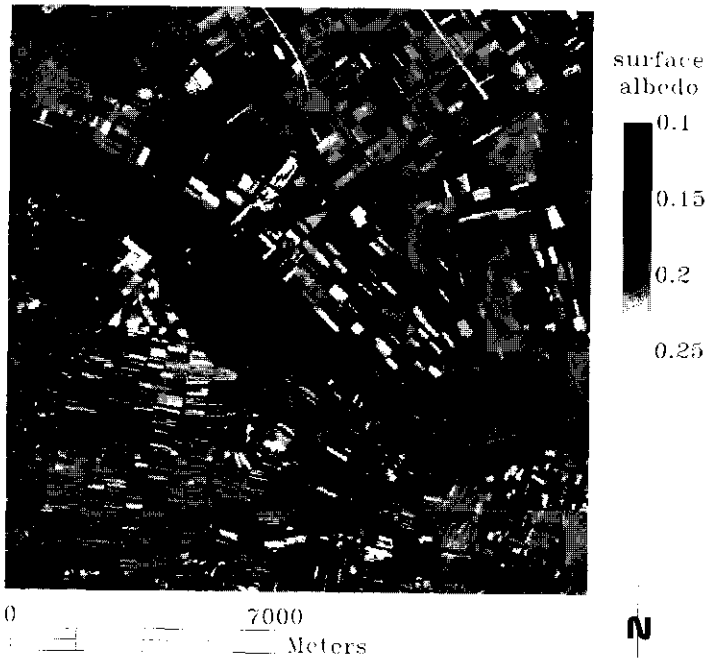

Plate F: Grid 3, The Central Part of the Netherlands, July 11 1995, surface albedo, r_0.

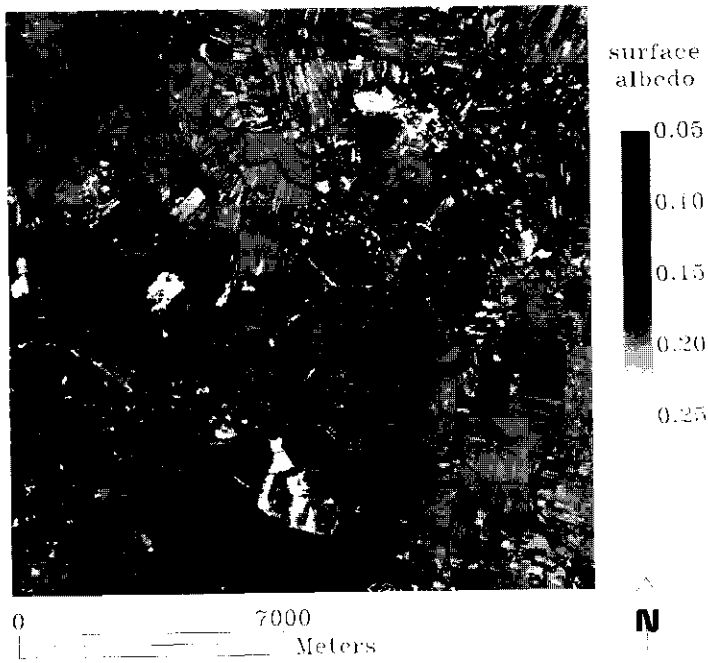

Plate G: Grid 8, The Central Part of the Netherlands, July 11 1995, surface albedo, r_0.

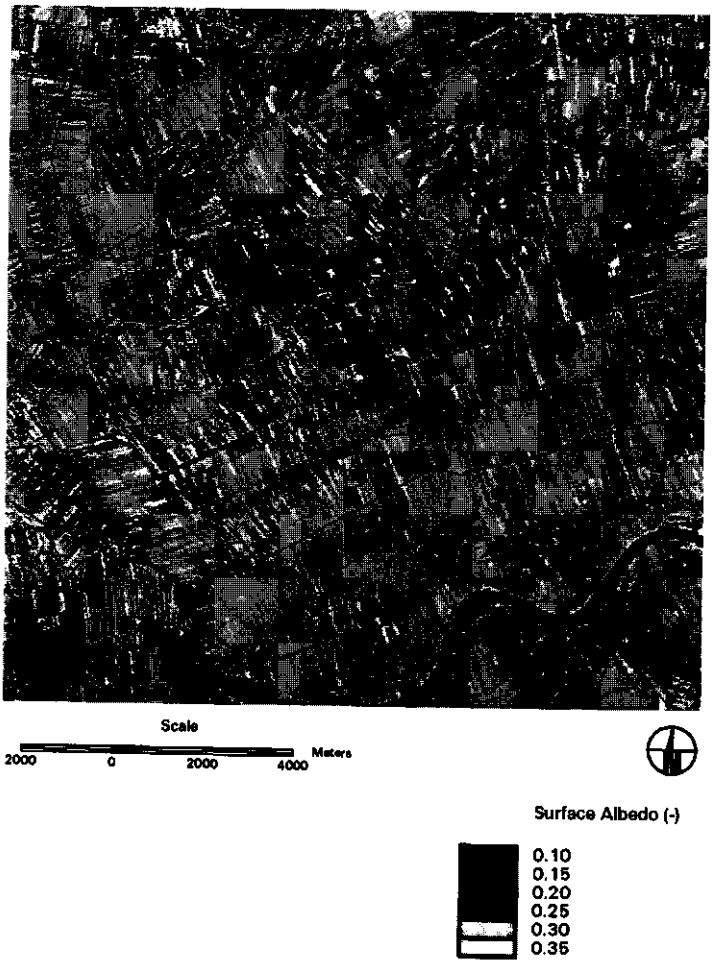

Plate H: Grid 11, The Central Part of the Netherlands, July 11 1995, surface albedo, r_0.